2015

Development of New Tools for Study of Tumor Microenvironment

Michael D. Anderson
University of Rhode Island, anders81@my.uri.edu

DEVELOPMENT OF NEW TOOLS FOR STUDY OF TUMOR MICROENVIRONMENT

BY

MICHAEL ANDERSON

A DISSERTATION SUBMITTED IN PARTIAL FULFILLMENT OF THE REQUIREMENTS FOR THE DEGREE OF

DOCTOR OF PHILOSOPHY

IN

PHYSICS

UNIVERSITY OF RHODE ISLAND

2015

DOCTOR OF PHILOSOPHY DISSERTATION

OF

MICHAEL ANDERSON

APPROVED:

Dissertation Committee:

Major Professor: Oleg Andreev
Yana Reshetnyak
Ying Sun
Nasser H. Zawia

DEAN OF THE GRADUATE SCHOOL

UNIVERSITY OF RHODE ISLAND
2015

ABSTRACT

Solid tumors have a microenvironment that is inherently acidic and hypoxic. Hypoxia is caused by leaky blood vessels and large diffusion distances from cells to them. It is heterogeneous throughout the tumor and while all solid tumors are hypoxic to a degree, it is difficult to predict invasiveness based on it. However, acidity is a near ubiquitous characteristic of tumors with more aggressive tumors producing greater acidity. It is important to measure pH in diseased tissue with accuracy and precision, since acidity is associated with the development of various pathological states including tumors. In this work we focus on the acidosis aspect of the tumor microenvironment by describing the development of pHLIP® (pH (Low) Insertion Peptides) targeting based tools that are capable of imaging the pH of a tumor microenvironment. pHLIP was chosen as a targeting vehicle because of its pH dependent insertion mechanism that allows it to effectively target acidic tissues, including tumors.

We used pHLIP® to study the roles of carboxyl groups in transmembrane (TM) peptide insertion. pHLIP binds to the surface of a lipid bilayer as a disordered peptide at neutral pH; when the pH is lowered, it inserts across the membrane to form a TM helix. Peptide insertion is reversed when the pH is raised above the characteristic pK_a (6.0). A key event that facilitates membrane insertion is the protonation of aspartic acid (Asp) and/or glutamic acid (Glu) residues, since their negatively charged side chains hinder membrane insertion at neutral pH. In order to gain mechanistic understanding, we studied the membrane insertion and exit of a series of pHLIP variants where the four Asp residues were sequentially mutated to nonacidic residues,

including histidine (His). Our results show that the presence of His residues does not prevent the pH-dependent peptide membrane insertion at $\sim$ pH 4 driven by the protonation of carboxyl groups at the inserting end of the peptide. We expect that our understanding will be used to improve the targeting of acidic diseased tissue by pHLIP.

Looking from the lipid bilayer's perspective, small angle x-ray scattering studies showed membrane thinning by 18% induced by insertion of short-pHLIP (truncated version of pH Low Insertion Peptide) into bilayer. Thinning allows to reduce stress on membrane associated with negative hydrophobic mismatch. Also we observed 12% of membrane thinning when long-pHLIP partitions into outer leaflet of bilayer at high pH adopting coil conformations. The long-pHLIP at high pH creates an asymmetric inclusion in the bilayer, which results in increase of tension leading to the bilayer thinning. The tension and thinning is released when long-pHLIP inserts into bilayer as a transmembrane helix at low pH.

The first tool developed is a new ^{64}Cu-pHLIP peptide for targeting, imaging and quantifying acidic tumors by positron emission tomography, and our findings reveal utility in assessing prostate tumors. The new pHLIP version limits indiscriminate healthy tissue binding, and we demonstrate its targeting of extracellular acidification in three different prostate cancer models, each with different vascularization and acid-extruding protein carbonic anhydrase IX (CAIX) expression. We then describe the tumor distribution of this radiotracer *ex vivo*, in association with blood perfusion and known biomarkers of acidity such as hypoxia, lactate dehydrogenase A and CAIX. We

find that the new probe reveals metabolic variations between and within tumors, and discriminates between necrotic and living tumor areas.

The second tool introduced is a novel approach of extracellular pH measurements at the surface of cells, which is based on the use of a pH-sensitive fluorescent dye SNARF conjugated to a pH Low Insertion Peptide (WT-pHLIP), which targets plasma membranes of cells in acidic diseased tissue. Our experimental set up includes two different approaches, one is based on acquisition of fluorescent spectra, and other one is based on recording of images via two emission filters. By using appropriate calibration curves obtained on liposomes and tumor spheroids in the presence of 2-deoxyglucose, both approaches give the same values of surface pH. The developed tool was validated on cancer cells grown in tumor spheroids, in mice and excised tumors *ex vivo*. We establish that highly metastatic cancer cells have lower pH at their surface compared to non-metastatic cells. Our approach was sensitive enough to detect pH changes *in vitro* and *in vivo* induced by glucose, which leads to the enhancement of cancer cells metabolism and acidification of the extracellular space. The introduced tool could be developed for clinical application of surface pH measurements in biopsy samples. It might provide important clinical information about tumor stage and invasiveness, and can guide in the choice of treatment approach.

ACKNOWLEDGMENTS

First I would like to thank my advisor Dr Oleg Andreev and Yana Reshetnyak for their support throughout this process. Honestly I do not know where I would be without them. They had faith in me even before they knew me. They gave me oppurtunities that I never deserved. They were patient with me throughout all my mistakes (and there was a lot of them) and made sure that I would never fail. Ultimately I feel privledged to have had researchers of their caliber mentor me.

I thank my parents for their relentless support of me. They always made sure that I had the best medical care and that I was taken care of. It didn't matter if I called them up falling apart, they would listen to me and help me get through it. I will never forget the constant encouragement that they give me.

I am forever grateful to my wife Leann Anderson for always supporting me and moving far from home with me just so that I could go to graduate school. She always made coming home pleasurable and is truly the only person who understands me. Also, for not only condoning, but contributing to my cat loving ways.

To my fur baby, Bella, for making bad days better with your cuddles.

A big thank you to my Uncle Dick for always challenging me to think, supporting me and exposing me to different experiences.

Thank you Grandma Reedy, while she has passed on, my grandma always encouraged me in my studies and never doubted me.

I would like to thank Mr. Jonathon Zinnel. While I am sure that he will never know how much he helped me, it was his faith in me at the start of 8^{th} grade that completely changed the course of my academic career.

Also thank you Mr. Maurice Green for giving me so much of your time, energy and defending me at the end of high school. He was the reason that I learned to love and appreciate physics.

I am grateful to Dr. Bartley Cardon for his support throughout undergraduate school. He helped me understand that just because I am not great, does not mean that I am worthless. He made me feel special and ultimately guidied me on where to go for my next step.

I would like to thank my graduate program committee members Dr Ying Sun, Dr Gerhard Müller and Dr Bongsup Cho for giving their precious time even when it is not convenient for them. I feel lucky to have such a collection of wonderful professors as my graduate committee.

I thank my colleagues and friends from our lab for their valuable discussions and help with experiments. I appreciate their many contributions to the work presented in this thesis. A special thanks to Jennifer Daniels and Anuradha Weerakkody for making my days better through telling stories, playing games and discussions.

I would like to thank staff members of URI graduate school for kindly fielding my many questions.

I am grateful to all who have helped me throughout my entire academic career from Saint John's, East Noble High School, Purdue University to The University of Rhode Island. While I wish that I could name all of them, everything that I have done is because of of their help.

PREFACE

This dissertation is written in the 'Manuscript Format' using the Thesis/ Dissertation template of University of Rhode Island. There are four manuscripts, each organized into a chapter. Tables and figures of each manuscript are listed under the corresponding chapter in the list of tables and figures.

The results of our studies presented here were published in four papers:

1. Barrera, F. N., Weerakkody, D., **Anderson, M**., Andreev, O. A., Reshetnyak, Y. K. and Engelman, D. M. Roles of Carboxyl Groups in the Transmembrane Insertion of Peptides, *J. Mol. Biol*. 413, 359-371 (2001).
2. Nerissa Therese Viola-Villegas, Sean D. Carlin, Ellen Ackerstaff, Kuntal K. Sevak, Vadim Divilov, Inna Serganova, Natalia Kruchevsky, **Michael Anderson**, Ronald G. Blasberg, Oleg A. Andreev, Donald M. Engelman, Jason A. Koutcher, Yana K. Reshetnyak, Jason S. Lewis. Understanding the pharmacological properties of a metabolic PET tracer in prostate cancer. *Proceedings of the National Academy of Sciences*, *111*(20), 7254-7259 (2014).
3. Dhammika Weerakkody, Alexander Karabadzhak, **Michael Anderson**, Fallon Laliberte, Oleg A. Andreev, Theyencheri Narayanan, Yana K. Reshetnyak, Insertion of short peptide into lipid bilayer: negative hydrophobic mismatch. In preparation for publication.
4. **Michael Anderson**, Linden Wyatt, Gregory Andreev, James Segala, Anna Moshnikova, Donald M. Engelman, Yana K. Reshetnyak, Oleg A. Andreev.

pH at the surface of cancer cells measured *in vitro*, *in vivo* and *ex vivo*. In preparation for publication

TABLE OF CONTENTS

LIST OF TABLES

LIST OF FIGURES

CHAPTER 1 PAGE

CHAPTER 2

CHAPTER 1

Published in Journal of Molecular Biology on

21th of October, 2011

Roles of Carboxyl Groups in the Transmembrane Insertion of Peptides

Francisco N. Barrera[1], Dhammika Weerakkody[2], Michael Anderson[2], Oleg A. Andreev[2], Yana K. Reshetnyak[2], Donald M. Engelman[1]

[1] Department of Molecular Biophysics and Biochemistry, Yale University, PO Box 208114, New Haven, CT 06520, USA

[2] Physics Department, University of Rhode Island, Kingston, RI 02881, USA

Research Highlights

pHLIP forms a TM helix at acidic pH. We mutate all aspartic acid residues. His residues do not prevent pH-dependent peptide membrane insertion. The number of residues that protonate correlates with insertion cooperativity.

Abbreviations

TM, transmembrane; wt, wild type; POPC, 1-palmitoyl-2-oleoyl-*sn*-glycero-3-phosphocholine; OCD, oriented circular dichroism; PEG, polyethylene glycol; pH, extracellular pH

Keywords

membrane protein folding; pHLIP; pH trigger; carboxyl titration; transmembrane helix

Abstract

We have used pHLIP® [*pH* (*l*ow) *i*nsertion *p*eptide] to study the roles of carboxyl groups in transmembrane (TM) peptide insertion. pHLIP binds to the surface of a lipid bilayer as a disordered peptide at neutral pH; when the pH is lowered, it inserts across the membrane to form a TM helix. Peptide insertion is reversed when the pH is raised above the characteristic pK_a (6.0). A key event that facilitates membrane insertion is the protonation of aspartic acid (Asp) and/or glutamic acid (Glu) residues, since their negatively charged side chains hinder membrane insertion at neutral pH. In order to gain mechanistic understanding, we studied the membrane insertion and exit of a series of pHLIP variants where the four Asp residues were sequentially mutated to nonacidic residues, including histidine (His). Our results show that the presence of His residues does not prevent the pH-dependent peptide membrane insertion at ~ pH 4 driven by the protonation of carboxyl groups at the inserting end of the peptide. A further pH drop leads to the protonation of His residues in the TM part of the peptide, which induces peptide exit from the bilayer. We also find that the number of ionizable residues that undergo a change in protonation during membrane insertion correlates with the pH-dependent insertion into the lipid bilayer and exit from the lipid bilayer, and that cooperativity increases with their number. We expect that our understanding will be used to improve the targeting of acidic diseased tissue by pHLIP.

Introduction

Extracellular acidification is a hallmark of different pathologies, including cancer, inflammation, ischemic stroke, and atherosclerotic plaques. Acidosis might be a useful biomarker for diagnosis or treatment if means can be found to target tissue acidity. We have found that a peptide derived from helix C of bacteriorhodopsin,[1] named pHLIP® [**pH** (**l**ow) **i**nsertion **p**eptide], is capable of targeting acidic tissues and inserting into the cell plasma membrane.[2] pHLIP is able to target mouse tumors **in vivo** with high specificity,[2] opening the possibility of its use for cancer imaging. Additionally, pHLIP has a promising therapeutic potential, as it is able to translocate cell-impermeable cargo molecules, such as organic dyes, peptides, peptide nucleic acids, and toxins, across the plasma membrane into the cytoplasm of tumor cells. [2 and 3] pHLIP itself does not have obvious acute toxicity in cells[3] or in mice.[2]

pHLIP is monomeric at low concentrations, with a mostly unstructured conformation in neutral and basic solutions (state I). If lipid vesicles or membranes are present at neutral pH, pHLIP binds to their external surface with an energy of 6–7 kcal/mol (state II).[4] In the membrane-attached state, pHLIP remains largely unstructured.[1] However, if the solution pH is lowered, pHLIP inserts to form a transmembrane (TM) α-helix (state III). The insertion is fully reversible and unidirectional, with the C-terminus being translocated across the membrane.[3] The p$\mathbf{K}_a$ of peptide insertion into lipid bilayers is 6.0, and the energy difference between the attached state and the inserted state is 1.8 kcal/mol at 37 °C.[4]

The pHLIP sequence is relatively rich in acidic residues (Table 1). At neutral pH, the combined negative charges of these residues, together with the carboxy terminus, constitute a large energetic barrier to pHLIP insertion across the membrane. The estimated energetic cost of the transfer of a single aspartic acid residue from water to the hydrophobic core of the membrane is unfavorable by 3.6 kcal/mol for the unprotonated (negatively charged) state, but only by 0.4 kcal/mol for the protonated (noncharged) state.[5] Simultaneously moving four charged Asp residues, one Glu residue, and the carboxy terminus into the membrane would cost 21.6 kcal/mol, assuming 3.6 kcal/mol for each carboxyl group, and peptide partitioning into the membrane at equilibrium would be about $1{:}10^{16}$. Thus, for pHLIP to be able to insert into membranes, protonation of a large fraction of the acidic residues can be expected, and knowledge of the protonation pattern of the acidic residues of pHLIP is an essential part of understanding the molecular mechanism of the membrane insertion process for any peptide containing carboxyl groups. Two classes of carboxyl groups are of interest: those that remain buried in the membrane after pHLIP is inserted into the membrane and those that traverse the hydrophobic core of the membrane during insertion.[6] Accordingly, we have studied both the pH-driven membrane insertion and the exit process for a series of peptides where the key aspartic acid residues are sequentially mutated.

Results

Previous studies in our laboratories revealed that sequence variations in the TM region of pHLIP can disrupt the delicate balance that preserves its water solubility. For example, a simultaneous change in the two aspartic acid residues at positions 14 and 25 to the homologous glutamic acid (Asp14/25Glu) resulted in a loss of pH-dependent membrane insertion due to aggregation of the peptide in aqueous solution[7] (we have recently developed new pHLIP variants with several Glu residues, which preserve pH-dependent properties; unpublished data). In order to reduce the likelihood that the introduced variations in the peptides used in this work could cause aggregation, we decided to follow a dual strategy to increase their water solubility: (i) we added an Asp tag to the N-terminus (noninserting end) to increase the number of charges in the molecule, which typically improves the solubility of hydrophobic peptides[8 and 9]; this resulted in the replacement of the N-terminal sequence AAEQ with DDDED (Table 1); and (ii) we used the TANGO algorithm[10] to define the region of the pHLIP sequence with the highest aggregation tendency and found this to be the stretch from residue 21 to residue 30 (coinciding with the most hydrophobic region of the peptide). We then mutated Leu26 to Gly, which greatly reduced the predicted aggregation tendency.

We incorporated these modifications into a series of pHLIP variants, where four aspartic acid residues were sequentially mutated to nonacidic polar residues. The aspartic acid residues at the C-terminus of the peptide that transitorily traverse the core of the membrane upon insertion (Asp31 and Asp33) were replaced with polar but

uncharged asparagine residues. On the other hand, for the Asp residues that are located in the core of the membrane after insertion (in positions 14 and 25), histidine was chosen as the replacement residue, as it is expected to be partially charged at neutral pH (thus improving water solubility) while being only slightly polar in its uncharged state (the transfer energies from water to the bilayer interior are 0.43 and 0.11 kcal/mol for the neutral forms of Asp and His,[5] respectively) so that the insertion properties of pHLIP may not be altered. The peptides were named D0–D3 according to the number of aspartic acid residues present in the regions of interest (TM and C-terminus; the positively charged N-terminus is not expected to interact with the membrane). For the variants with three aspartic acids, two alternatives were studied: one that kept Asp14 (D3a peptide) and the other that kept Asp25 (D3b peptide).

We conducted experiments to test the state of the variants in solution, where pHLIP is largely found as an unstructured monomer.[11] Sedimentation velocity experiments were conducted to determine the oligomerization state of the different peptide variants in aqueous buffer. Previous analysis of wild-type (wt) pHLIP (at 7 μM in 10 mM phosphate buffer and 100 mM NaCl, pH 8)[11] showed that pHLIP is mostly monomeric, but a small oligomer population is observed (~ 6%). We performed our sedimentation velocity experiments under the same conditions, but without NaCl in the solution. For each peptide, we observed a peak with a sedimentation coefficient of 0.72 ± 0.12 S (Table 2 and Fig. 1), which corresponds to a molecular mass of 3.4 ± 0.8 kDa. This is in agreement with the expected monomer masses of the different peptides (4126 Da for wt and ~ 4300 Da for the different variants), with the differences being ascribed to shape effects from the extended peptide. In the case of

D1 and D0, a minor peak with a sedimentation coefficient of 3.3 ± 0.3 S was also observed. This component represents $5 \pm 2\%$ of the total population, and its sedimentation coefficient corresponds to a molecular mass of 43 kDa (roughly consistent with the presence of an octameric or decameric particle). Comparison of our results with the previous report for wt suggests that the presence of oligomers is reduced at lower ionic strength. For the particular case of the D1 and D0 peptides, they seem to have a slightly higher oligomerization tendency in solution, but they are still 95% monomeric. Thus, our results suggest that all the peptide variants remain soluble and are essentially monomeric. For the rest of the experiments, we employed peptide concentrations (1.5–5 μM) lower than that used for sedimentation analysis (7 μM); thus, the level of oligomers present for D1 and D0 is expected to be lower.

Fluorescence spectra of the peptides in aqueous solution at neutral pH showed that, in all cases, the emission maximum is centered around 347–349 nm (Fig. 2, black lines, and Table 2), indicating that the two tryptophan residues of the peptides are largely exposed to aqueous solution, as in fully unfolded proteins, and consistent with the slightly low sedimentation coefficient. This finding represents an improvement over the previously studied Asp14/25Glu mutant peptide, where peptide aggregation shifts the emission maximum to 342 nm in buffer at pH 8.[7] A similar fluorescence maximum was also observed for the Asp14/25Asn mutant under the same conditions.[2] The presence of mostly unstructured species in aqueous solution for each of the studied peptides was confirmed by circular dichroism (CD) experiments, since the observed CD spectra were characterized by a minimum at 203 nm (Fig. 3, black lines), as observed for pHLIP in state I.

The two lipid-interacting states of the pHLIP variants were then examined: state II, where wt pHLIP is mostly unstructured and attached at the bilayer surface, and state III, where wt pHLIP forms a TM helix at low pH.[1 and 6] Fluorescence experiments in the presence of 1-palmitoyl-2-oleoyl-**sn**-glycero-3-phosphocholine (POPC) liposomes revealed that for the two D3 variants, the characteristic fluorescence signatures for states II and III were evident: (i) in the presence of liposomes at neutral pH (Fig. 2, blue lines), the fluorescence emission maxima of the peptides were slightly shifted from 348.7 ± 1.0 to 346.2 ± 1.2 nm, accompanied by a small fluorescence increase (Table 2); and (ii) when the pH was lowered to pH 4, we observed a large fluorescence increase and a spectral blueshift to 336.2 ± 1.1 nm (red lines), which are typically observed when the Trp side chain is buried in the membrane hydrophobic core. To complement the fluorescence data, we performed CD experiments under the same conditions (Fig. 3). The CD signature of the pHLIP membrane insertion process consists of the appearance of the characteristic signals associated with the formation of α-helix: minima at 208 and 222 nm and positive ellipticity at 190 nm. Both D3 variants showed spectral changes very similar to those observed for wt upon acidification. Thus, we concluded that replacement of one of the Asp residues in the TM region of the peptide does not lead to changes in the peptide's ability to interact with the membrane in a pH-dependent manner.

The D2 variant, where both Asp residues are replaced by His residues, also demonstrates a pH-dependent membrane interaction. However, the spectral pattern is slightly different from those for wt and D3 variants: the fluorescence intensity of D2 in the presence of POPC decreases in the pH range 8–6, with no significant changes in

the spectral maximum at pH 8–7 and with a small shift to lower wavelengths at pH 6 (Fig. S1). The amount of the helical structure of D2 at neutral pH is slightly higher than those of wt and D3 (Fig. 2 and Table 2), while no change is seen in the pH range 8–6. As an explanation, we suggest that D2 partitions somewhat more deeply into the membrane lipid bilayer than wt and D3 at neutral pH values, since His residues are expected to be only partially charged at neutral pH values, enhancing the hydrophobicity of the peptide TM and its affinity for the lipid bilayer. The decrease in fluorescence signal in the pH range 8–6 might be attributed to the partial quenching of emission of at least one of the Trp residues by one of the partially protonated His residues. At the same time, at neutral pH values, the peptide C-terminus containing four negative charges (two Asp, one Glu, and the C-terminus) does not partition into the membrane, keeping the peptide at the membrane surface. A further drop of the pH to pH 3–4 is associated with a fluorescence spectral maximum blueshift, an increase in fluorescence intensity (Fig. 2), and the appearance of a more pronounced negative band at 222 nm on CD spectra (Fig. 3), which is usually an indication of peptide insertion into the bilayer.[1] Reduction of pH leads to the protonation of negatively charged groups at the C-terminus and peptide insertion into the membrane. At the same time, we expect that protonation of His residues at low pH should occur; this might lead to the peptide's exit from the lipid bilayer or, alternatively, the formation of a pore channel in the lipid bilayer, where positively charged His residues would be pointed toward the channel. Calcein encapsulation control experiments that rule out the formation of pores in the membrane by the D2 and D3 peptides were performed (Fig. S2). Thus, most probably, the p$\mathbf{K}_a$ for the protonation of His is shifted to very

low pH values when it is embedded in a lipid bilayer. We carried out fluorescence pH titrations to compare the behaviors of D2 and wt peptides at pH values lower than 3.5 (Fig. S3). While no fluorescence change was detected for wt at acidic pH values, we observed that an additional process was present for D2 (with an apparent p$\mathbf{K}_a$ of 2.5), characterized by a fluorescence decrease and a redshift of the spectral maximum, which might be associated with peptide exit from the lipid bilayer.

To establish the orientation of each helix in the membrane, we performed oriented circular dichroism (OCD) measurements in which the light beam is oriented perpendicular to the planes of a stack of oriented lipid bilayers containing the peptides of interest. Theoretical calculations and experimental data indicate that helices oriented with axes parallel with the membrane surface (perpendicular to the incident light) give CD signals distinctly different from those of helices oriented across the bilayer (parallel with the incident light).[12, 13 and 14] In the range of 190–240 nm, the peptide CD spectrum is dominated by π–π* and n–π* transitions.[15] The π–π* transition in a helix splits into three components, one of which gives rise to a negative Gaussian band near 205 nm, with its electric transition dipole parallel with the helical axis. When the incident light propagates parallel with the helical axis, the electric field vector is orthogonal to the 205-nm π–π* dipole transition, and there is no interaction between the electromagnetic wave and the dipole, leading to the disappearance of the negative band at 205 nm in a CD spectrum. Thus, when the supported bilayers are oriented perpendicular to the light propagation, a helix with a TM orientation will have a CD spectrum that contains a positive 190-nm band and a negative 225-nm band. If the helix adopts a membrane surface orientation on the supported bilayer, then

all transitions are seen, and the OCD spectrum is the same as for a peptide CD spectrum in solution, with randomly oriented helices. Our data clearly indicate that D2 adopts a TM orientation at pH 3.5–4.5, while increasing the pH leads to peptide exit and the appearance of a membrane surface orientation of the helix (Fig. 4). The OCD spectrum at pH 1.9 does not correspond to a TM helix. Thus, we conclude that the p$\mathbf{K}_a$ of both or at least one of the His residues is significantly shifted from 6.3–6.9[16] to a lower value (2.5) due to their location at the bilayer interface in state II, emphasizing the important influence of bilayer surface properties on the p**K** values of dissociating groups in interacting peptides. A similar trend was previously observed for peptides that insert into membranes **via** the deprotonation of His residues, [17 and 18] although the magnitude of the p$\mathbf{K}_a$ shift was smaller. However, large changes in p$\mathbf{K}_a$ are typically observed when the side chains are in different environments, as the protonation of titratable amino acids depends on the dielectric properties of their environment.[19] A fitting example of large p$\mathbf{K}_a$ changes is found in the native environment of pHLIP, bacteriorhodopsin, where Asp14 and Asp25 have p$\mathbf{K}_a$ values of 7.5 and > 9, respectively,[20] significantly higher than the p$\mathbf{K}_a$ values of 3.7–4.0 found for fully solvated aspartic acid side chains.[16]

D1 has one less Asp residue at the C-terminus than D2. The slightly larger blueshift of fluorescence emission (Fig. 2) and the higher content of helicity observed in the presence of POPC at neutral pH values (Fig. 3) could be associated with an even deeper position of the peptide in the membrane. Fluorescence spectral blueshift and intensity increase, together with an increase in ellipticity at 222 nm, occur upon acidification; this might indicate protonation of Asp33, Glu34, and the C-terminus, as

well as peptide insertion into the lipid bilayer. The OCD spectrum obtained for D1 at pH 3.3 (Fig. 4) does not show a clear TM orientation of the helix: some decrease in ellipticity at 205–225 nm—which might indicate the existence of a mixture of TM and surface-parallel orientations of helices or the appearance of a significantly tilted TM helix—is observed. D0, in contrast to all other pHLIP variants described above, has a blueshifted maximum of fluorescence emission (Fig. 2) at neutral pH values in the presence of POPC, with a high content of helical structure (Fig. 3). Virtually no changes in spectral signal occur for D0 upon acidification (Figs. 2 and 3). The OCD data primarily reveal a surface orientation of the helix at low pH values (Fig. 4), as expected for a peptide with no aspartic acids.

To study the magnitude and directionality of the membrane insertion of the peptides, we used a biotin–avidin binding assay. A biotin moiety was attached to the C-terminus of each peptide. The level of binding to avidin was measured, and the protection of the biotin molecule from avidin interaction was used to assess the translocation of the peptide C-terminus into the liposome interior. The biotin moiety was linked to the C-terminal Cys of the peptides **via** a long polar polyethylene glycol (PEG) linker. The linker has a double purpose. It facilitates biotin access to the avidin binding site and—more critically for our experiments—helps to delineate between an intraliposomal location and an extraliposomal location of the biotin, since the polarity of the moiety makes a location inside the hydrophobic region of the bilayer unlikely. We quantified the amount of biotin that binds to avidin molecules present exclusively outside the liposomes (see Materials and Methods for details). We did not detect avidin binding to biotin for the D2 peptide at low pH (Fig. 5a) due to the biotin translocation across the

membrane, which complements our data (suggesting complete insertion of this peptide across the lipid bilayer) and confirms that the directionality of insertion is the same as for wt. Only partial translocation and no translocation of biotin across the membrane were seen for D1 and D0, respectively (Fig. 5a), in agreement with our results indicating partial (or tilted) insertion and no insertion into the lipid bilayer of D1 and D0, respectively. Additionally, the translocation of biotin (which can be considered as a cargo) across the membrane does not appear to significantly hinder the membrane insertion of the peptides. This might be explained by its small size (526 Da) and its moderate polarity (log$\boldsymbol{P}$ = − 1.4; see Materials and Methods for details), which are both well within the range of cargo properties that pHLIP has been reported to effectively translocate.[21] However, as the biotin assay used here is responsive to changes in the level of binding to avidin present outside of the liposomes, we cannot rule out the possible influences of different processes such as peptide aggregation, although we have no reason to suspect them.

How does the number of carboxyl groups affect the p$\boldsymbol{K}$ and cooperativity of insertion? We monitored the pH-induced changes in the position of the fluorescence emission maximum of the peptides, which provide details about peptide insertion into the lipid bilayer, in the presence of POPC (Fig. 6). A plot of the positions of the spectral maxima follows a sigmoid behavior as a function of pH, corresponding to the transition between the interfacial state and the inserted state for all variants (except for D0). Fitting the experimental data provides the two main parameters that describe the insertion process: p$\boldsymbol{K}_a$ and cooperativity (**m**). The p$\boldsymbol{K}_a$ of membrane insertion obtained for wt pHLIP is 5.94 ± 0.09, which is in agreement with previous reports. [1 and 7] For the

different variants, shifts of the p$\boldsymbol{K}_a$ to lower values (~ 5.2) were detected (Fig. 7a). The reason for this decrease is unclear, but it might be related to the lower number of aspartic residues or to the presence of histidines in the TM region of the pHLIP variants. We do not think that the N-terminal DDDED sequence will influence the p$\boldsymbol{K}_a$ values of the peptides in our study, since its polarity should preclude hydrophobic interaction with the lipid bilayer; thus, it is not expected to be involved in the insertion process. However, we cannot rule out that it might reduce the overall membrane affinity of the peptide. While the p$\boldsymbol{K}_a$ values for the variants changed very little, we observed a gradual decrease in the cooperativity of the insertion process (**m** parameter) for peptides with fewer Asp residues, as the titration occurred progressively over a wider pH range (~ 1 pH unit for wt and ~ 2 pH units for D1) (Figs. 6 and 7b). Our data indicate that the cooperativity of insertion is linked to the number of protonatable residues. Cooperativity and p$\boldsymbol{K}_a$ might also respond to the position of protonatable groups in the peptide sequences and their proximity to each other. When pHLIP is at the surface of the vesicle and the pH is lowered, the protonation of one Asp residue might facilitate the protonation of other protonatable residues, shifting their p$\boldsymbol{K}_a$ values. The protonation of the first Asp residue might induce partial insertion of the peptide into the membrane. In this scenario, the protonation of the neighboring Asp residues would be energetically favored to shield the negative charge (i.e., the p$\boldsymbol{K}_a$ value of the neighboring Asp is shifted to higher values in a more hydrophobic environment) and then a positive feedback would be established, triggering membrane insertion.

How do the number and the location of Asp residues affect peptide exit from the membrane? The CD and fluorescence changes associated with wt pHLIP lipid insertion at acidic pH are completely reversible.[11] Here we also followed changes in the CD and fluorescence signals and in the reversibility of biotin translocation across the membrane. The ellipticity increase associated with each peptide insertion into the membrane was found to be essentially reversible for wt and D3b (Fig. 3, broken blue lines overlap with continuous blue lines), while for D3a, D2, and D1, the reversibility was only partial. Since changes in the CD signal upon acidification for D2–D0 are less pronounced than those for wt and D3, the reversibility of the D2–D0 membrane insertion was also assessed by changes in the fluorescence signal (Fig. S4). It is interesting to note the different levels of reversibility of the two D3 peptides: the insertion process is significantly more reversible in D3b (90%) than in D3a (70%) (Fig. 5b), suggesting nonequivalence of the two buried positions. We observed an overall linear relationship between the number of aspartic acid residues interacting with the membrane and the degree of α-helix formation reversibility (Fig. 5b). The results obtained for the reversibility of the biotin translocation (exit process) were also in agreement (Fig. 5b).

An important consideration in the interpretation of the exit data is the time course of equilibration of the pH inside the liposomes, so we encapsulated the membrane-impermeable fluorescent probe 5(6)-carboxy-2′,7′-dichlorofluorescein in POPC liposomes to follow the pH changes. The fluorescence of the probe is pH-sensitive, with a p$\boldsymbol{K}_a$ of 5.1. When we varied the pH of the solution outside the liposomes, the fluorescence of the encapsulated probe changed in a sigmoid fashion, with an apparent

p$\boldsymbol{K}_a$ of 5.05 (data not shown). A relatively high proton permeation through unilamellar POPC liposomes in the minute timescale has been reported elsewhere. [22 and 23] On the other hand, our kinetic data suggest that the time of wt peptide exit (with two TM groups and four C-terminal protonatable groups) is in the range of milliseconds.[6] Thus, peptides exit from the lipid bilayer much faster such that the pH is completely equilibrated inside the liposomes and, most probably, C-terminal residues cross the membrane in their noncharged form. The question is: 'Why is the reversibility of D3a, D2, and, to some degree, D1 only partial?' To provide an explanation, we take into account the location of the Asp residues. For the peptide exit from the lipid bilayer to take place, the deprotonation of Asp residues must energetically destabilize the inserted state. Destabilization of the inserted state is mainly caused by the charges resulting from the deprotonation of groups deeply buried in the hydrophobic core of the membrane. Therefore, the exit of wt and D3b, which have two Asp or one Asp in the hydrophobic core of the membrane, is fully reversible. The reason for the difference in peptide insertion reversibility between D3a and D3b might be related to the presence of an arginine residue at position 11. Accordingly, the deprotonation of Asp25 in D3b would strongly destabilize the membrane-inserted state due to the presence of a negative charge in the hydrophobic core of the membrane, favoring the exit process. However, the negative charge of Asp14 in D3a might be forming a salt bridge with the neighboring side chain of Arg11, which would result in a weaker destabilization of the inserted state. Another potential explanation is an altered position of the TM domain, which was mentioned above. There is a possibility that the TM domain in variants is shifted toward the C-terminal residues, leading to a greater

exposure of the amino acid in position 14 (with His in D3a) to the aqueous environment and a shift to the hydrophobic core of amino acids at positions 31 and 33. As a result, the deprotonation of His14 in D3a might be associated with less destabilization of the helix than deprotonation of His25 in D3b. The side chains of Asp31 and Asp33 most probably are interacting with the headgroup region of the bilayer. The destabilization energy associated with their deprotonation is not enough to cause a complete exit from the membrane. Our results suggest that the deprotonation of acidic residues located in the hydrophobic core of the membrane ensures complete exit of the peptide.

Discussion

We have previously observed that even conservative changes in the pHLIP sequence can lead to peptide aggregation in solution at neutral pH.[7] Our results show that all the peptides in this study are soluble in solution, being essentially monomeric (the addition of a D-tag at the N-terminus and the L26G mutation appear to favor peptide solubility). Spectral data obtained with D3–D0 peptides indicate that the lower is the number of negatively charged groups in the peptide sequence, the deeper are the peptide partitions into a lipid bilayer and the greater is the helicity. At the same time, TM orientation (at least for the D3–D2 peptides) requires protonation of the Asp/Glu residues and the terminal carboxyl group at the C-terminus, which can readily go across a membrane in its noncharged form. We confirmed our previous finding[2] suggesting that TM Asp residues are not essential for peptide insertion. Interestingly, we have observed here that membrane insertion upon acidification occurs in our peptides in the presence of two His residues in the predicted TM region. Histidines

have been used in the past to drive the insertion of peptides into membranes at neutral pH values.[17 and 18] However, in these examples, acidic residues were completely absent in the sequence. For the peptides described in this article, the establishment of states II and III is driven by acidic residues. Since the protonated (charged) state of the side chains of His14 and His25 in the hydrophobic core of the membrane would be energetically very unfavorable, in the peptides, their p$\boldsymbol{K}_a$ values are expected to shift to lower values in the membrane-inserted state (favoring the unprotonated state). Further acidification eventually causes their protonation, resulting in a strong destabilization of the inserted TM helix and peptide exit. We cannot rule out that the diminished membrane insertion of the D1 and D0 peptides might be influenced by the hydrophobicity change concomitant to the Asp-to-Asn mutations at the C-terminus. The free energy of membrane transfer of the Asn side chain is 0.42 kcal/mol, which is a less favorable value than the free energy of transfer of the neutral state of Asp ($-$ 0.07 kcal/mol)[5]; thus, the membrane translocation of the C-terminus would be less favorable. A similar effect might occur in the insertion reversibility of D1.

We conclude that protonation of negatively charged residues located in the TM or in the C-terminal inserting end must occur in order to preserve the pH-dependent ability of pHLIP to interact with the membrane. These residues act as switches for pHLIP membrane insertion, as the negative charges of their side chains block membrane insertion. Acidification causes the protonation of these side chains, resulting in an increase in the overall hydrophobicity of the peptide, which leads to TM helix formation, shielding the hydrophobic residues of pHLIP from water molecules. When the pH is raised to near neutrality, the negatively charged state of the carboxyl groups

is again favored, decreasing the peptide hydrophobicity and resulting in exit from the TM position. Peptide exit from the lipid bilayer is completed when deprotonation of Asp/Glu residues located in the hydrophobic core of the membrane occurs and the TM helix is destabilized.

The knowledge gained from our experiments can be used as a guide to improve the imaging and therapeutic properties of pHLIP. For the specific case of tumor targeting, the pHLIP insertion characteristics should be finely tuned to exploit the low extracellular pH (pH_e) of tumors. Tumor targeting by wt pHLIP conjugated to a Cu^{64}–1,4,7,10-tetraazacyclododecane-1,4,7,10-tetraacetic acid chelate for positron emission tomography imaging correlates with the pH_e of tumors, where the contrast index was higher for LNCaP tumors (pH_e 6.78 ± 0.29) than for PC-3 tumors (pH_e 7.23 ± 0.10[24]). Thus, pHLIP variants where Asp14/Asp25 were replaced by Glu, with a higher pK_a (pK_a = 6.5),[7] might be more effective for targeting tumors with higher pH_e values. Our present results suggest that the number of Asp residues in the TM region can also modulate the pK_a value. Thus, a peptide containing an extra Asp in the TM region might have a higher pK_a and might be directed to tumors more effectively. Another important factor to be considered is the broadness of the pH transition of the peptide, which is dictated by the cooperativity of the transition. On one hand, for the case where the peptide pK_a is lower than the tumor pH_e but the transition is broad (**m** value is low), a significant part of the pH transition could intercept the pH_e value, resulting in a significant pHLIP tumor insertion. However, such a scenario will also lead to more accumulation in healthy tissue. Since it is usually desirable to have a high tumor/organ ratio, an insertion transition of high cooperativity might be best. This

would ensure greater differentiation between the amount of inserted peptides and the amount of noninserted peptides over a narrow range of pH values, favoring selective tumor targeting, since the difference in pH between normal tissue and cancerous tissue may be only 0.5–0.7 units. However, we must bear in mind that the measured pH_e provides an indication of the average acidity outside the cell for a given tumor and can vary between different tumor regions. Furthermore, pH_e may not reflect the precise pH on the exterior surface of the cells, since the cells pump protons to the extracellular medium and ΔpH will lead to proton accumulation at the membrane surface.[25] Another feature that is expected to shift the equilibrium toward the membrane-inserted form is the presence of Asp/Glu residues at the C-terminus of the peptide. After being translocated across the plasma membrane into the cytoplasm, where the pH is neutral, these groups would be deprotonated. Since the translocation of charges across membranes is unfavorable, the inserted form would be stabilized.

pHLIP shows promise as a means of targeting cells in acidic tissues and delivering agents for therapy and imaging. At the same time, we are learning more about the binding and insertion of peptides at the membrane surface. Here we have shown that variation in the positions and numbers of carboxyl group titrations modulates the p***K*** and cooperativity of insertion.

Materials and methods

Peptide synthesis and assessment of monomeric state

Peptides were made by solid-phase synthesis, using standard 9-fluorenylmethyloxycarbonyl chemistry, at the W. M. Keck Foundation Biotechnology Resource at Yale University (New Haven, CT) and were purified by reverse-phase chromatography (C18 column, using a water/acetonitrile gradient in 0.01% trifluoroacetic acid). Purity was checked by matrix-assisted laser desorption/ionization time-of-flight mass spectrometry. Peptides were quantified by absorbance spectroscopy using a molar extinction coefficient of 13,940 M^{-1} cm^{-1}. Some peptides contain a single Cys residue in the C-terminus and thus have the potential to form intermolecular disulfide bonds, leading to the formation of dimers. To rule out the possibility that this might occur under our experimental conditions, we ran HPLC on peptide samples incubated (at room temperature for 3 h) at concentrations higher than those used in our experiments and in the absence and in the presence of POPC. No dimer band could be detected, and concentrations in the range of 0.1 mM peptide and overnight incubation were required to detect a significant amount of dimer (~ 10%). The peptides described in Table 1 were used in the experiments, except for some experiments with D2–D0, where a Cys-less version was employed (similar results were obtained for both results; data not shown).

Analytical ultracentrifugation

Sedimentation velocity experiments were performed at 25 °C in a Beckman Optima XL-I analytical centrifuge at 35,000 rpm. Peptides at a concentration of 7 μM were

dissolved in 5 mM phosphate buffer (pH 8) after 1 h of incubation at room temperature. Absorbance at 280 nm was used to monitor centrifugation, and analysis was performed using SEDFIT.[26]

Liposome preparation

The required amount of chloroform-dissolved POPC (Avanti Polar Lipids) was placed in a glass tube, dried with argon, and then held under vacuum overnight. The dried film was resuspended in water or 10 mM phosphate buffer (pH 8) and vortexed. Extrusion to make unilamellar vesicles was performed using a Mini-Extruder (Avanti Polar Lipids), with Nuclepore polycarbonate membranes of 0.1 or 0.05 μm pore size (Whatman). To obtain the final large unilamellar vesicles, we performed 15–25 extrusion steps, depending on the lipid concentration.

Fluorescence spectroscopy

Peptides were dissolved in 5 or 10 mM phosphate buffer (pH 8) and incubated with POPC vesicles prepared in water, resulting in a molar lipid/peptide ratio of 250:1. The incubation time with POPC liposomes varied from 90 min to 18 h. The pH of the samples was adjusted with a 10 mM concentration of the buffers for the indicated pH ranges (H_3PO_4, pH 1.0–3.5; sodium acetate, pH 3.5–5.5; Na_2HPO_4/NaH_2PO_4, pH 5.5–8.0; sodium borate, pH 8.0–10.5) or by addition of concentrated HCl. The final peptide concentration was varied from 1.5 to 5 μM in different experiments. Emission spectra were measured in SLM-Aminco 8000C and PC2 ISS spectrofluorometers at

room temperature (controlled temperature), with excitation at 295 nm. The appropriate blanks were subtracted in all cases.

For determination of spectral maxima, we used the FCAT mode of the PFAST software, which fits the experimental spectra to log-normal components.[27 and 28] The spectral maxima values for each point of the pH curve were plotted and analyzed according to[29]:

$$F = \frac{\left(F_a + F_b 10^{m(pH-pKa)}\right)}{(1+10^{m(pH-pKa)})} \qquad \text{Equation(1)}$$

where $\boldsymbol{F}_a = (\mathbf{f}_A + \mathbf{S}_A pH)$ and $\boldsymbol{F}_b = (\mathbf{f}_B + \mathbf{S}_B pH)$; $\mathbf{f}_A$ and $\mathbf{f}_B$ are the spectral maxima for the acidic and basic forms, respectively; $\mathbf{S}_A$ and $\mathbf{S}_B$ are the slopes of the acidic and basic baselines, respectively; and **m** is the cooperativity parameter. Fitting by nonlinear least squares analysis was carried out with Origin software.

Circular dichroism

Samples were prepared as in the fluorescence experiments, but the final molar lipid/peptide ratio was 300:1, with the final peptide concentration varying from 2 to 5 μM. CD spectra were recorded in Jasco J-810 and MOS450 Biologic spectropolarimeters interfaced with a Peltier system. Spectra were recorded at 25 °C using 2- or 5-mm cuvettes, the scan rate was 50 nm/min, and 10–30 averaging steps were performed. Raw data were converted into mean residue ellipticity according to[30]:

$[\Theta]=\Theta/(10\boldsymbol{lcN})$

where Θ is the measured ellipticity, ***l*** is the path length of the cell, ***c*** is the protein concentration, and ***N*** is the number of amino acids.

For the study of membrane attachment, insertion, and its reversibility, the typical procedure was as follows: The samples were incubated with POPC vesicles at pH 8 for 90 min, the spectra were recorded, the pH was lowered to 4.0, and the measurements were performed after 30 min. Finally, the pH of the sample was increased with sodium borate buffer (pH 10.2) to a final pH of 7.5. After 30 min, 90 min, and 24 h, the spectra were recorded, and similar results were obtained in all cases. The degree of reversibility was established from the recovery of the signal at 222 nm. The final buffer concentration for the different experiments was in the range of 3–15 mM. Appropriate blanks were subtracted in all cases.

OCD measurements

For OCD measurements, supported bilayers were prepared on quartz slides with 0.2-mm-thick spacers on one side and with a special polish for far-UV measurements (Starna). Slides were cleaned by sonication for 10 min in cuvette cleaner solution (Decon Contrad 70, 5% in water), 2-propanol, acetone, and 2-propanol, and rinsed with deionized water. Then the slides were immersed in a mixture of concentrated sulfuric acid and hydrogen peroxide (3:1) for 5–10 min to completely remove any remaining organic material from the slides. The slides were then thoroughly rinsed with and stored in deionized water (Milli-Q purified water kept at 25 °C). A POPC lipid monolayer was deposited on a quartz substrate by the Langmuir–Blodgett

method using a KSV mini-trough. For the Langmuir–Blodgett deposition, a cleaned slide was vertically immersed in the clean subphase (Milli-Q purified water kept at 25 °C) of a Langmuir–Blodgett trough. A POPC lipid solution in chloroform was spread on the subphase, and chloroform was allowed to evaporate for about 30 min, followed by monolayer compression to 32 mN/m. The first layer was deposited by retrieving the slide from the subphase at a rate of 15 mm/min. The second layer of the bilayer was created by fusion. For this step, the monolayer on the slide was incubated with a solution of POPC vesicles (50 nm in diameter, obtained by extrusion) mixed with peptide solution at the required pH (0.5 mM POPC and 10 μM peptide). The fusion occurred for about 6 h under 100% humidity. Then, excess vesicles were carefully removed, and the slides were stacked to make a pile while filling up the spaces between them with a peptide solution (5 μM) at the required pH. The bilayers with the peptide solution were allowed to equilibrate for about 6 h. Measurements were taken in three steps during the process: when the monolayers were incubated with an excess of liposomes, soon after the spaces between the bilayers had been filled with the peptide solution and 6 h after the second measurement. Fourteen slides (28 bilayers) were assembled, and the OCD spectrum was recorded on a MOS-450 spectrometer at a sampling time of 2 s.

Biotin translocation assay

HABA dye (4′-hydroxyazobenzene-2-carboxylic acid) binds to avidin at a 1:1 stoichiometry and absorbs at 510 nm only in the avidin-bound state. This interaction is strongly displaced by the binding of biotin to avidin, resulting in a quantitative

reduction in HABA absorbance. This property was used to probe the location of the C-terminus of different peptides with regard to the liposome (inside or outside) (method modified from Nicol **et al.**[31]). The C-terminus of each of the peptide variants was labeled with biotin (see the text below). The rationale for the assay is that pH-driven insertion of the C-terminus would result in biotin translocation inside the liposome, causing shielding of the biotin from the medium outside the liposome, where a preformed HABA/avidin complex (Thermo Scientific) is added. If the biotin is inside the liposome, no change in absorbance is expected. On the other hand, if pHLIP lies at the exterior surface of the liposome, the C-terminal biotin would be accessible to the solution outside the liposome (as the biotin group is polar, it is expected not to be protected by the membrane) and would be able to bind to avidin and displace the HABA/avidin complex, with a consequent reduction in absorbance at 510 nm. Liposomes were prepared in 150 mM NaCl, and ionic strength was carefully maintained during all steps to avoid liposome osmotic shock. Biotin-labeled peptides were incubated in the presence of POPC at pH 8 for 2 h at room temperature (150:1 lipid/peptide ratio). For studies of C-terminal translocation, acetate buffer was added to the samples, resulting in a final pH of 4.3 prior to 1 h of incubation with the peptide. The HABA/avidin complex was added to the solution only after the final conditions had been established. The final peptide concentration for the measurement conditions was 3 μM. To determine the reversibility of the biotin translocation, we increased the pH by the addition of 10 mM sodium borate buffer (pH 10.2) to give a final pH of 7.4. Absorbance was measured after 1 h of incubation. For quantitation of the level of reversibility, the recovery of absorbance obtained for pHLIP labeled with

biotin at its C-terminus was taken as 100% reversibility, and that of pHLIP labeled at its N-terminus was taken as 0%.

Peptides were labeled at the C-terminal Cys residues using the membrane-impermeable compound maleimide–PEG_2–biotin (Thermo Scientific), which has a long polar spacer arm of 29.1 Å to allow adequate biotin binding to avidin. The synthesis reaction was performed in 10 mM phosphate buffer (pH 7.5; overnight incubation at 4 °C). Reaction products were purified by HPLC, and the mass of the biotin-labeled peptides was checked by matrix-assisted laser desorption/ionization time-of-flight mass spectrometry. The octanol/water partition coefficient of maleimide–PEG_2–biotin was determined experimentally by measuring the absorbance at 300 nm in the aqueous and octanol (previously preequilibrated with water) phases after 2 h of vortexing. A log***P*** value of − 1.07 ± 0.02 was obtained. As this value does not take into account the chemical changes in the cross-linking reaction (formation of a thioether bond between the maleimide moiety and the Cys side chain), the QikProp 3.0 software was employed to predict the log**P** value of the reacted form, resulting in a value of − 1.4, which is in the range of molecules that can be translocated by pHLIP.[21]

Acknowledgements

The authors are thankful to Miriam Alonso, Ming An, Justin Fendos (Yale University), and José Luis Neira (Universidad Miguel Hernández) for stimulating discussions and insightful comments on the manuscript. D.M.E. was supported by National Institutes of Health grant GM073857-04. O.A.A., D.M.E., and Y.K.R. were

supported by National Institutes of Health grant CA133890-03. F.N.B. was the recipient of a postdoctoral fellowship from the Fundación Alfonso Martín Escudero.

References

1. Hunt, J. F., Rath, P., Rothschild, K. J. & Engelman, D. M. (1997). Spontaneous, pH-dependent membrane insertion of a transbilayer alpha-helix. Biochemistry. 36, 15177-15192.

2. Andreev, O. A., Dupuy, A. D., Segala, M., Sandugu, S., Serra, D. A., Chichester, C. O., Engelman, D. M. & Reshetnyak, Y. K. (2007). Mechanism and uses of a membrane peptide that targets tumors and other acidic tissues in vivo. Proc. Natl Acad. Sci. U. S. A. 104, 7893-7898.

3. Reshetnyak, Y. K., Andreev, O. A., Lehnert, U. & Engelman, D. M. (2006). Translocation of molecules into cells by pH-dependent insertion of a transmembrane helix. Proc. Natl. Acad. Sci. U. S. A. 103, 6460-6465.

4. Reshetnyak, Y. K., Andreev, O. A., Segala, M., Markin, V. S. & Engelman, D. M. (2008). Energetics of peptide (pHLIP) binding to and folding across a lipid bilayer membrane. Proc. Natl. Acad. Sci. U S A 105(40):15340-5.

5. White, S. H. & Wimley, W. C. (1999). Membrane protein folding and stability;Physical principles. Annu. Rev. Biophys. Biomol. Struct. 28, 319-365.

6. Andreev, O. A., Karabadzhak, A. G., Weerakkody, D., Andreev, G. O., Engelman, D. M. & Reshetnyak, Y. K. (2010). pH (low) insertion peptide (pHLIP) inserts across a lipid bilayer as a helix and exits by a different path. Proc. Natl. Acad. Sci. U. S. A 107, 4081-4086.

7. Musial-Siwek, M., Karabadzhak, A., Andreev, O. A., Reshetnyak, Y. K. & Engelman, D. M. (2009). Tuning the insertion properties of pHLIP. Biochim. Biophys. Acta. 1798(6):1041-6

8. Melnyk, R. A., Partridge, A. W., Yip, J., Wu, Y., Goto, N. K. & Deber, C. (2003) Polar residue tagging of transmembrane peptides. Biopolymers.71(6):675-85.

9. Cunningham, F. & Deber, C. M. (2007). Optimizing synthesis and expression of transmembrane peptides and proteins. Methods 41, 370-380.

10. Fernandez-Escamilla, A. M., Rousseau, F., Schymkowitz, J. & Serrano, L. (2004). Prediction of sequence-dependent and mutational effects on the aggregation of peptides and proteins. Nat. Biotechnol. 22, 1302-1306.

11. Reshetnyak, Y. K., Segala, M., Andreev, O. A. & Engelman, D. M. (2007). A monomeric membrane peptide that lives in three worlds: in solution, attached to, and inserted across lipid bilayers. Biophys. J. (7); 2363-72.

12. Kuyper C.L., Kuo J.S., Mutch S.A. & Chiu D.T. (2006) Proton permeation into single vesicles occurs via a sequential two-step mechanism and is heterogeneous. J. Am. Chem. Soc. 128(10), 3233-40.

13. Deamer D.W. & Nichols J.W. (1989). Proton flux mechanisms in model and biological membranes. J. Membr. Biol. 107(2),91-103.

14. Thevenin, D., An, M. & Engelman, D. M. (2009). pHLIP-mediated translocation of membrane-impermeable molecules into cells. Chem. Biol 16, 754-762.

15. Pace, C. N., Grimsley, G. R. & Scholtz, J. M. (2009). Protein ionizable groups: pK values and their contribution to protein stability and solubility. J Biol Chem. 284, 13285-13289.

16. Bechinger, B. (1996). Towards membrane protein design: pH-sensitive topology of histidine-containing polypeptides. J. Mol. Biol. 263, 768-775.

17. Ladokhin, A. S. & White, S. H. (2004). Interfacial folding and membrane insertion of a designed helical peptide. Biochemistry 43 (19):5782 -91.

18. Harms, M. J., Castaneda, C. A., Schlessman, J. L., Sue, G. R., Isom, D. G., Cannon, B. R. & Garcia-Moreno, E. B. (2009). The pK(a) values of acidic and basic residues buried at the same internal location in a protein are governed by different factors. J Mol. Biol 389, 34-47.

19. Lanyi, J. K. (2006). Proton transfers in the bacteriorhodopsin photocycle. Biochim. Biophys. Acta 1757, 1012-1018.

20. Vavere, A. L., Biddlecombe, G. B., Spees, W. M., Garbow, J. R., Wijesinghe, D., Andreev, O. A., Engelman, D. M., Reshetnyak, Y. K. & Lewis, J. S. (2009). A novel technology for the imaging of acidic prostate tumors by positron emission tomography. Cancer Res. 69, 4510-4516.

21. Bränden, M., Sanden, T., Brzezinski, P. & Widengren, J. (2006). Localized proton microcircuits at the biological membrane-water interface. Proc. Natl. Acad. Sci. U. S. A 103, 19766-19770.

22. Schuck, P. (2000). Size-distribution analysis of macromolecules by sedimentation velocity ultracentrifugation and lamm equation modeling. Biophys. J. 78, 1606-1619.

23. Burstein, E. A., Abornev, S. M. & Reshetnyak, Y. K. (2001). Decomposition of protein tryptophan fluorescence spectra into log-normal components. I. Decomposition algorithms. Biophys. J 81, 1699-1709.

24. Shen, C., Menon, R., Das, D., Bansal, N., Nahar, N., Guduru, N., Jaegle, S., Peckham, J. & Reshetnyak, Y. K. (2008). The protein fluorescence and structural

toolkit: Database and programs for the analysis of protein fluorescence and structural data. Proteins 71, 1744-1754.

25. Ionescu, R. M. & Eftink, M. R. (1997). Global analysis of the acid-induced and urea-induced unfolding of staphylococcal nuclease and two of its variants. Biochemistry 36, 1129-1140.

26. Kelly, S. M. & Price, N. (2000). The use of Circular Dichroism in the investigation of protein structure and function. Current Protein and Peptide Letters 1, 349-384.

27.Nicol, F., Nir, S. & Szoka, F. C., Jr. (1999). Orientation of the pore-forming peptide GALA in POPC vesicles determined by a BODIPY-avidin/biotin binding assay. Biophys.
J 76, 2121-2141.

Tables

Table 1. Sequence of the peptides.

wt[a]	AAEQNPIYWARYA**D**WLFTTPLLLL**D**LALLV**D**A**D**EGTCG
D3a[b]	*DDD*E*D*NPIYWARYA**D**WLFTTPLLLL**H***G*ALLV**D**A**D**ECT
D3b	*DDD*E*D*NPIYWARYA**H**WLFTTPLLLL**D**GALLV**D**A**D**ECT
D2[c]	*DDD*E*D*NPIYWARYA**H**WLFTTPLLLL**H***G*ALLV**D**A**D**ECT
D1[c]	*DDD*E*D*NPIYWARYA**H**WLFTTPLLLL**H***G*ALLV**N**A**D**ECT
D0[c]	*DDD*E*D*NPIYWARYA**H**WLFTTPLLLL**H***G*ALLV**N**A**N**ECT
	14 25 31 33

[a] The pHLIP sequence is referred to as wt.

[b] The variant peptides are named by a D followed by the number of aspartic acid residues in the TM and C-terminal regions. Two different D3 peptides were studied, D3a and D3b, each with different transmembrane aspartic acid residues mutated. The acidic residues that are expected to interact with the hydrophobic core of the membrane at some stage of the insertion process (Asp 14, 25, 31 and 33, in red) were mutated to the polar residues marked in bold. The N-terminal Asp-tag and the Leu26Gly mutation are highlighted in italics. The transmembrane region of pHLIP was predicted, using the octanol scale[5], to be located between residues Ile7 and Leu29 (marked with inverted blue triangles). N- and C-terminus were not capped.

[c] A version of D2-D0 without cysteine were employed in experiments except of biotin translocation assay.

Table 2. Parameters describing the studied peptides.

	AUC [a]	Fluorescence					Circular Dichroism		
	Sed. Coef.	Spectral maximum, nm			Area curve		MRE 218 nm		
	State	State			State		State		
	I	I	II	III	II	III	I	II	III
wt	0.80±0.17[b]	347.7±0.6	347.2±1.6	336.7±0.1	1.04	2.10	-7.4	-7.4	-16.3
D3a	0.67±0.08	349.9±0.1	347.4±1.3	337.0±0.1	1.12	2.61	-7.6	-6.8	-15.4
D3b	0.66±0.09	349.1±1.0	345.5±0.7	334.6±0.2	1.08	2.11	-5.3	-6.1	-16.4
D2	0.84±0.16	348.2±0.1	344.9±1.4	336.5±0.7	1.09	1.53	-7.9	-9.3	-14.1
D1	0.88±0.18	346.2±3.6	343.7±1.6	337.4±1.0	1.10	1.46	-7.0	-10.5	-15.6
D0	0.75±0.20	347.2±1.0	341.0±0.6	338.0±0.9	1.71	1.21	-6.5	-13.5	-12.8

[a] The sedimentation coefficient for the peak corresponding to the monomer is showed.

[b] The averages and the standard deviations are provided.

[c] The spectral maxima were calculated with PFAST (see Methods).

Figures

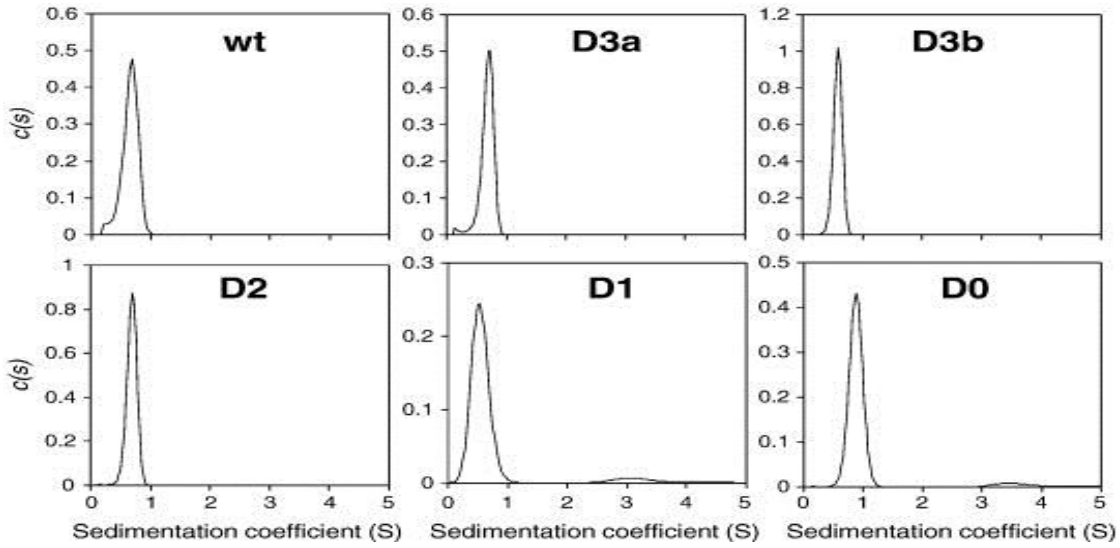

Figure 1. Sedimentation velocity of the different peptide variants. Apparent sedimentation coefficient distribution derived from sedimentation velocity profiles of the peptides(7 μM)) in 5 mM phosphate buffer at pH 8.

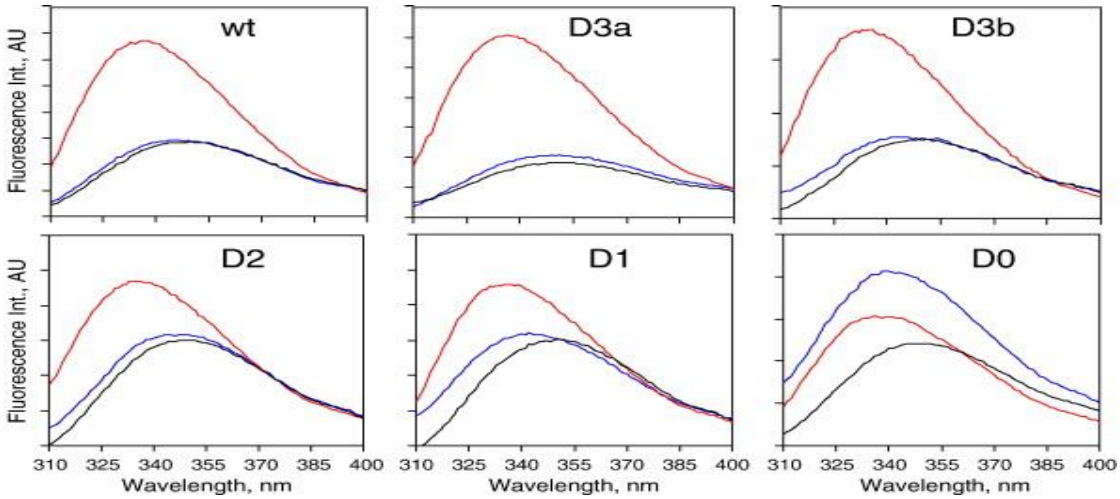

Figure 2. Fluorescence spectra of peptides in buffer and with POPC vesicles. Emission spectra of each variant were recorded under the following conditions: buffer at pH 7.5 (black lines), POPC at neutral pH (blue lines), and POPC at pH 4 (red lines). The pH values for the different POPC samples at neutral pH were selected according to the midpoint and slope of the transitions shown in Figure 6: wt, pH 7.5; D3a, pH 7.5; D3b, pH 7.1; D2, pH 6.5; D1, pH 6.2; D0, pH 8. The peptide concentration was 1.5 μM, and the lipid concentration was 375 μM. Fluorescence intensity is given in arbitrary units (AU).

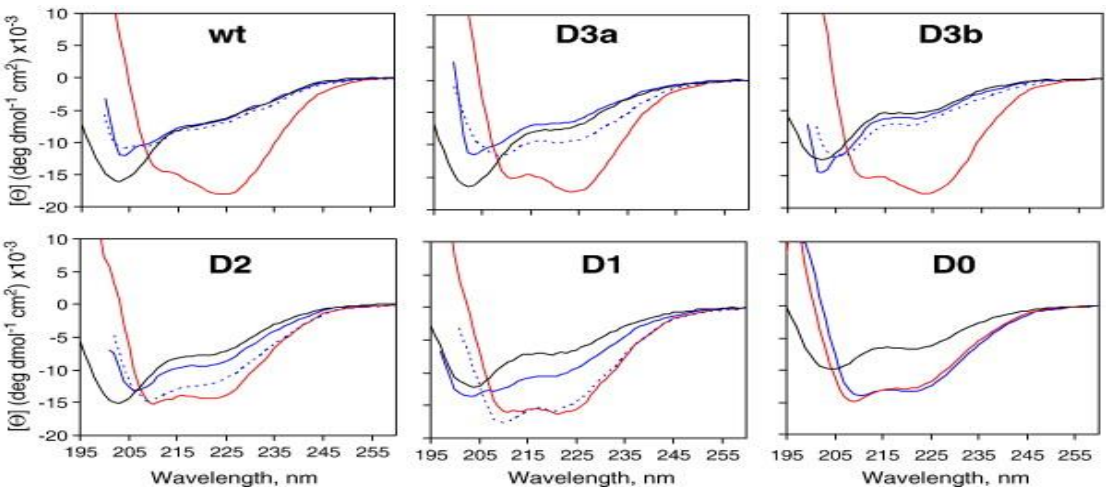

Figure 3. CD of peptides in buffer and with POPC vesicles. Far-UV CD spectra were recorded for all variants under different conditions: buffer at pH 7.5 (black lines), POPC at pH 7.4 (blue lines), and POPC at pH 4 (red lines). The reversibility of the insertion process was studied by raising the pH of the samples from pH 4 (broken blue line) to pH 7.4. Reversibility for D0 was not studied, as the ellipticity changes between the states at pH 7.5 and pH 4 were negligible. In all samples, the final peptide and lipid concentrations were 5 μM and 1.5 mM, respectively.

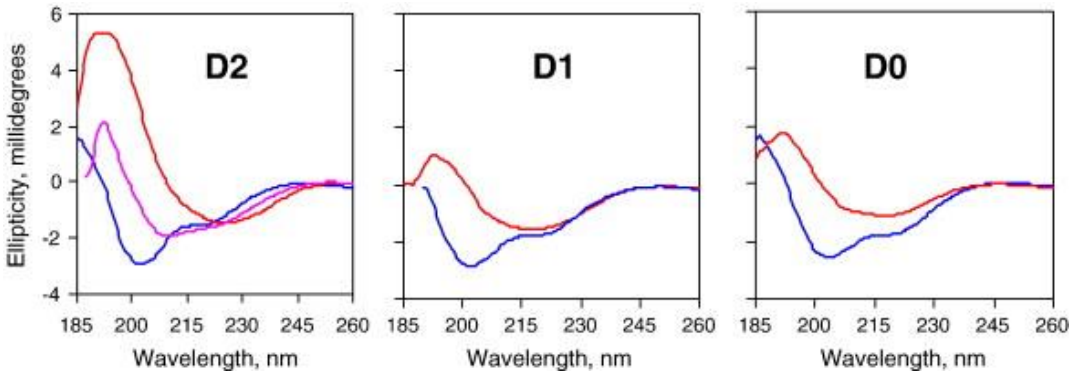

Figure 4. OCD spectra of D2, D1, and D0 measured on oriented POPC-supported bilayers at neutral (blue lines) and acidic (red lines) pH values. The OCD spectrum of D2 at pH 1.9 was also recorded (purple line). The experimental spectra are corrected for the lipid background.

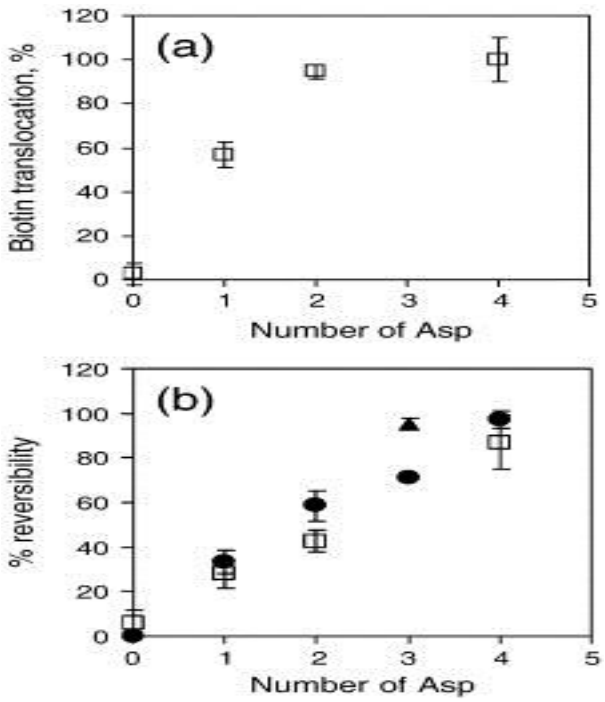

Figure 5. Quantification of membrane insertion (biotin translocation) and reversibility. Data corresponding to the biotin translocation assay (open squares) and CD (black symbols) were plotted against the number of Asp residues in the TM and C-terminal regions. (a) Degree of normalized biotin translocation (open squares). For data normalization, the translocation levels of wt pHLIP labeled with biotin at the C-terminus and N-terminus were used as 100% and 0%, respectively. Results from D3a and D3b are not shown for the biotin translocation assay, as the biotin labeling for these peptides affected the interaction with lipids (data not shown). No adverse effects of labeling were observed for the rest of the peptides tested. Averages and standard deviations are shown. (b) The percent reversibility of the biotin translocation of the samples used in (a) is shown (open squares). For CD experiments (Fig. 3), the degree of reversibility was determined by monitoring the relative changes in ellipticity at

222 nm (black symbols). Averages and standard deviations are shown. Data corresponding to D3b appear as a triangle, while the rest of the CD data appear as circles. All data points were used for linear fitting ($\mathbf{R}^2 = 0.95$).

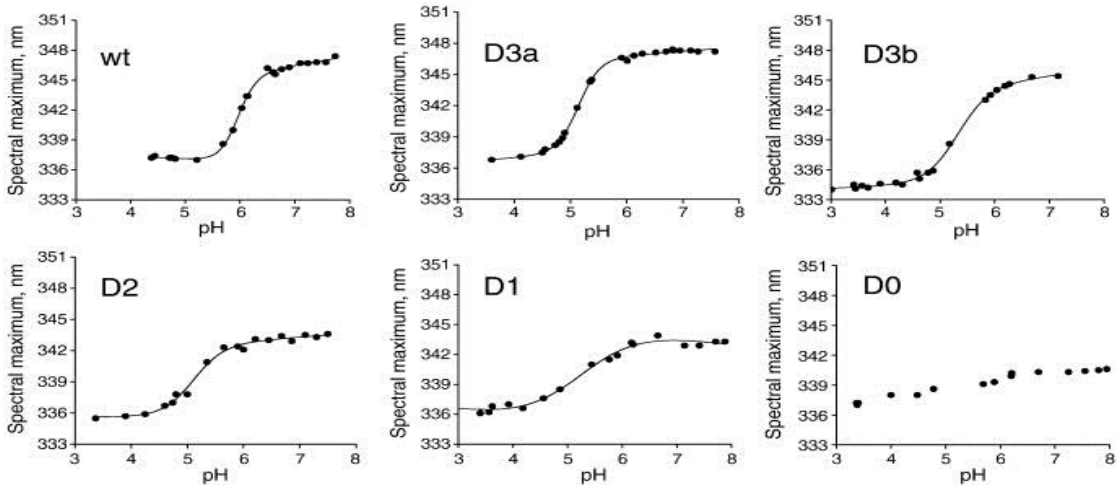

Figure 6. Fluorescence spectral maximum changes upon pH titration. The pH-controlled transitions of the peptides in POPC were followed by monitoring the variations in the spectral maxima. The experimental data for the different peptides were fitted to Eq. (1) (black lines). Representative experiments are shown.

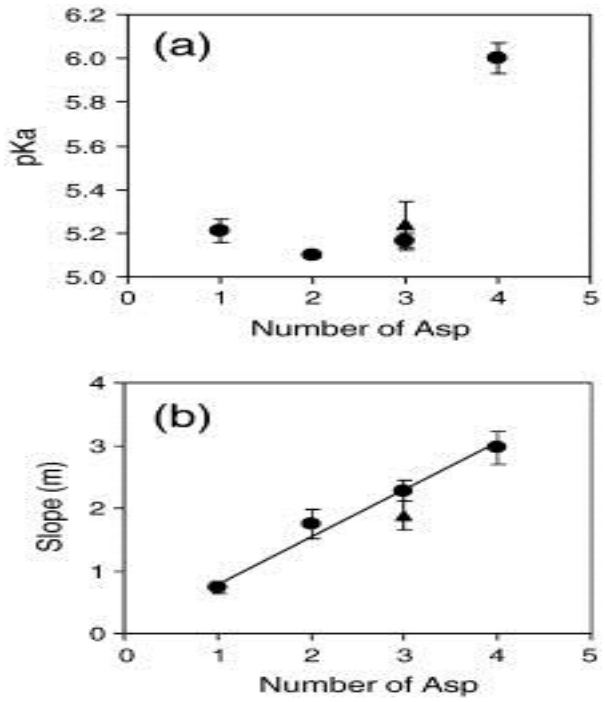

Figure 7. Parameters obtained from the fitting of fluorescence pH transitions. The p$\mathbf{K}_a$ (a) and **m** parameter (b) values obtained from the fitting of the data in Figure 6 to Eq. (1) are shown in black symbols. Data from the D3b variant are shown as triangles (to maintain the representation as in Fig. 5). The line corresponds to the fitting of all data points ($\mathbf{R}^2$ = 0.93). Averages and standard deviations are shown.

Supplementary information

Roles of carboxyl groups in the transmembrane insertion of peptides.

Francisco N. Barrera, Dhammika Weerakkody, Michael Anderson, Oleg A. Andreev,

Yana K. Reshetnyak and Donald M. Engelman

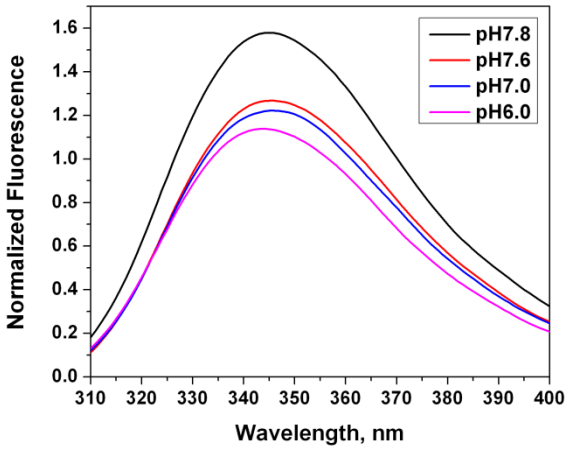

Figure S1. Fluorescence of D2 in presence of POPC at various pH values**.**

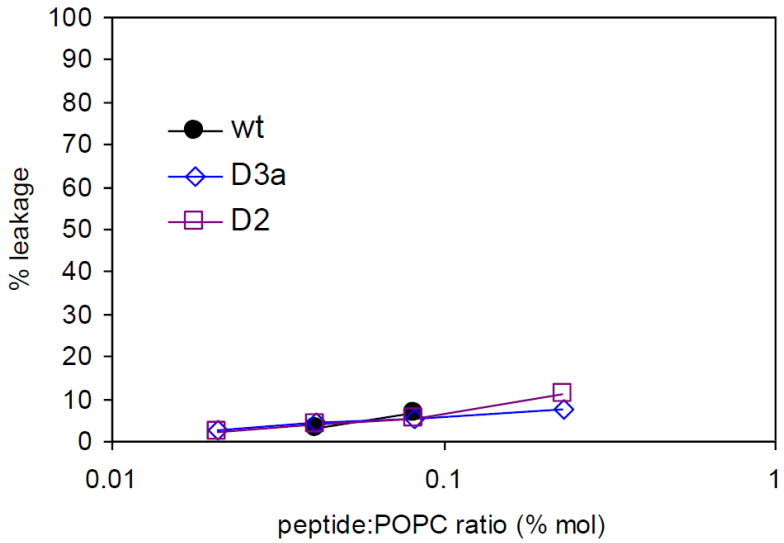

Figure S2. Leakage of encapsulated calcein. The release of calcein encapsulated in large unilamellar POPC liposomes was measured by following the fluorescence at 515 nm in the presence of different concentrations of peptides. Little disruption by peptide interaction is seen. The level of 100% disruption of liposomes was determined by addition of 0.05% Triton X-100

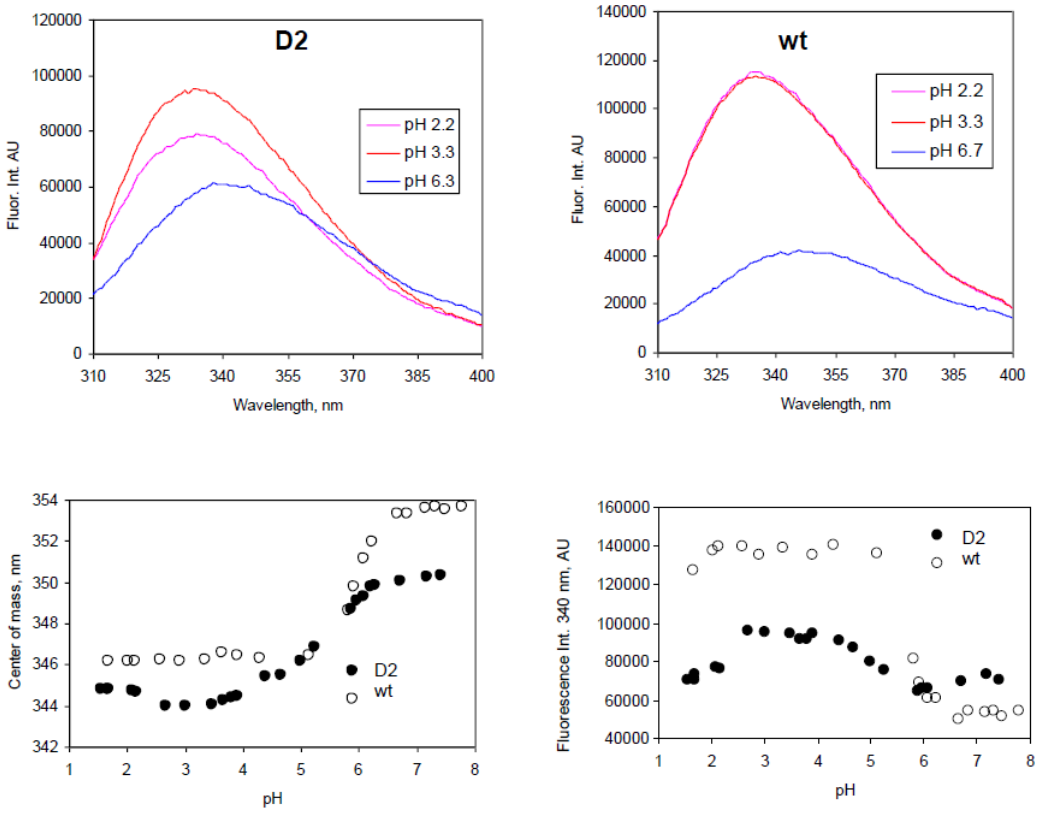

Figure S3. Fluorescence of wt and D2 at low pHs. The usual range of pHs was extended to lower values to study the protonation state of His residues. D2 was employed as an example of peptide containing two His residues. *Upper panels:* Emission spectra in POPC liposomes at pH 2.2, 3.3 and 6.3. *Lower panels:* the fluorescence intensity and center of mass were calculated for the complete pH range studied for D2 and wt pHLIP.

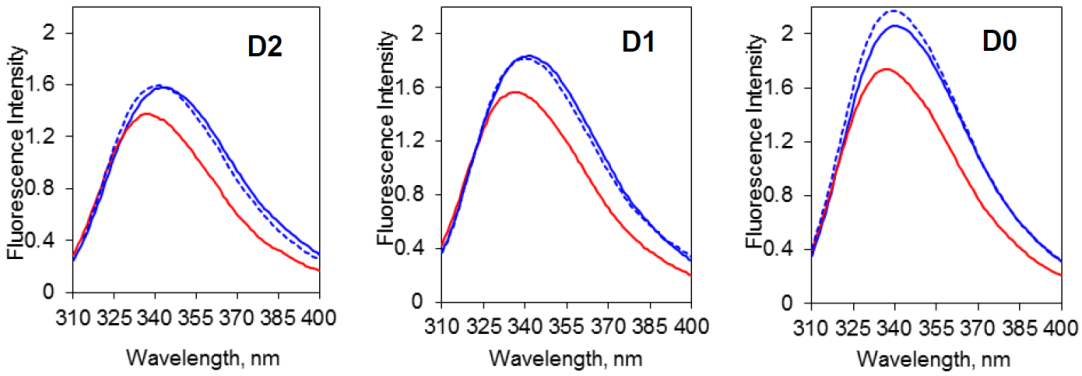

Figure S4. Fluorescence studies of the reversibility of the membrane insertion for D2, D1 and D0. Spectra were measured of the peptides in the presence of POPC at pH 4.1 (red lines) and 7.8 (straight blue lines). The pH of the samples at pH 4.1 was increased back to 7.8 (dashed blue lines) to study reversibility. For D2, where acidification caused TM helix formation occurs, the two blue lines have a good overlap, suggesting a high degree of reversibility. For D1 and D0, a TM helix is not formed in a pH-dependent fashion, so the interpretation of the reversibility data is less straightforward.

CHAPTER 2

Published in Proceedings of National Academy of Sciences (PNAS) on

20nd of May, 2014

BIOLOGICAL SCIENCES: Applied Biological Sciences

The Hot Side of pHLIP: Understanding the Pharmacological Properties of a Metabolic PET Tracer in Prostate Cancer

Nerissa Therese Viola-Villegas[1,2], Sean D. Carlin[1,2], Ellen Ackerstaff[3], Kuntal K. Sevak[2], Vadim Divilov[2], Inna Serganova[4], Natalia Kruchevsky[3], Michael Anderson[6], Ronald G. Blasberg[1,2,4], Oleg A. Andreev[6], Donald M. Engelman[7], Jason A. Koutcher[1,2,3,5], Yana K. Reshetnyak[6], Jason S. Lewis[1,2*]

Author Affiliations: [1]Program in Molecular Pharmacology and Chemistry, Department of [2]Radiology, [3]Medical Physics, [4]Neurology, [5]Medicine, Memorial Sloan-Kettering Cancer Center, 1275 York Avenue, New York, NY 10065 USA; [6]Physics Department, University of Rhode Island, 2 Lippitt Road, Kingston, RI 02881; [7]Department of Molecular Biophysics and Biochemistry, Yale University, P.O. Box 208114, New Haven, CT 06520

*** Corresponding Author:**

Jason S. Lewis, Ph.D.

Radiochemistry and Imaging Sciences Service — Tel: (646)8883038

Memorial Sloan-Kettering Cancer Center — Fax: (646)8883059

1275 York Avenue, New York, NY 10065 — Email: lewisj2@mskcc.org

Running Title: Non-invasive measurement of extracellular acidification in prostate tumor models

Keywords: Tumor acidosis, pHLIP, PET, prostate cancer

Disclosure of potential conflicts of interest:

There are no conflicts of interest.

Abstract

Solid tumors are inherently acidic, with more aggressive growth producing greater acidity. If the acidity could be targeted as a biomarker, it would provide a means to gauge the pace of tumor growth and degree of invasiveness as well as providing a basis for predicting responses to pH-dependent chemotherapies. We have developed a new ^{64}Cu-pHLIP peptide for targeting, imaging and quantifying acidic tumors by positron emission tomography, and our findings reveal utility in assessing prostate tumors. The new pHLIP version limits indiscriminate healthy tissue binding, and we demonstrate its targeting of extracellular acidification in three different prostate cancer models, each with different vascularization and acid-extruding protein carbonic anhydrase IX (CAIX) expression. We then describe the tumor distribution of this radiotracer *ex vivo,* in association with blood perfusion and known biomarkers of acidity such as hypoxia, lactate dehydrogenase A and CAIX. We find that the new probe reveals metabolic variations between and within tumors, and discriminates between necrotic and living tumor areas.

Introduction

The rapid growth and division of tumor cells creates an enhanced need for glucose and other nutrients, which the cells take up at a high rate, overwhelming their mitochondrial capacity to use all of the glucose efficiently (1). The result is aerobic glycolysis, which elevates lactate and proton production: the "Warburg" effect (1, 2). Further, some tumors are starved for oxygen, resulting in even more glycolytic acid production (3, 4). Under the resulting low pH conditions, normal cells have a tendency to undergo p53-induced apoptosis (5, 6), whereas cancerous cells invoke alternative routes, manipulating ion fluxes with proton extruders and other transporters to afford continuous survival (7). Pumping the acidic components out of the cell maintains cytoplasmic pH and enhances the pH gradient (ΔpH) and the cellular exterior surfaces become more acidic than those of cells in normal tissues (8). The level of extracellular acidification, however, is variable, depending on (i) the reliance of the malignancy on glycolysis (9-12), a phenomenon resulting from the pleiotropic adaptation of cancer cells towards a glycolytic phenotype, (ii) the impact of variation in the distal vascular delivery of nutrients, and (iii) the state of hypoxia (13, 14). The low pH environment stimulates cell invasion, angiogenesis and finally, metastasis (15-17).

Tumor acidosis could be a useful biomarker for selective drug delivery, targeting and delineation of malignancies. With the discovery of a membrane-inserting peptide (pHLIP) that preferentially binds to cell membranes at low pH, practical clinical imaging and delivery of therapeutic payloads may be possible (18-22). At normal pH, pHLIP binds as a largely unstructured peptide at a membrane surface, but at acidic pH it folds and inserts across the plasma membrane as an alpha helix (23).

We have previously demonstrated that pHLIP might be useful as a PET (Positron Emission Tomography) probe with ^{64}Cu ($t_{1/2}$~12.7 h) (24). Tumor uptake in prostate cancer models was achieved, and related to a low extracellular pH (pHe), but shortcomings were apparent (24). The success of the probe as a marker of acidosis was found to have contrast and clearance complexities associated with the pharmacokinetics (PK) of pHLIP, warranting further development efforts. Targeting of fluorescent pHLIP variants were recently studied, and a range of potential properties was found, including altered kinetics of insertion (Scheme 1) (25). Here, we describe a much improved PET probe that was developed using three strategies: modification of the 1) peptide sequence, 2) radiometal and 3) chelate. We confirmed the lead radiotracer's specificity for a low pH gradient by demonstrating an association between pHLIP-PET and pHe in different prostate cancer models, i) PC3-wt, ii) the constitutively expressing carbonic anhydrase IX-transduced PC3 (PC3-CAIX) and, iii) LNCaP cancer cells. Lastly, we extended our study by offering a representative relationship of pHLIP with perfusion, tumor viability and pathways associated with acidity (i.e. lactate via the lactate dehydrogenase A (LDH-A) protein subunit, hypoxia and CAIX overexpression). The new probe gives useful contrast, reveals metabolic variations within tumors and discriminates between necrotic and living tumor areas.

Scheme 1. pHLIP variants and their sequence

Name	Sequence
pHLIP-WT	ACEQNPIYWARYADWLFTTPLLLLDLALLVDADEGT
Var1	ACEDQNPYWARYADWLFTTPLLLLDLALLVDG
Var2	ACEDQNPYWRAYADLFTPLTLLDLLALWDG
Var12	ACEDQNPWARYADLLFPTTLAW
Var13	ACEEQNPWARYAELLFPTTLAW

Var10	ACEDQNPWARYADWLFPTTLLLLD
Var11	ACEEQNPWARYAEWLFPTTLLLLE
Var7	ACEEQNPWARYLEWLFPTETLLLEL
Var5	ACDDQNPWRAYLDLLFPTDTLLLDLLW
K-WT (control)	ACEQNPIYWARYAKWLFTTPLLLLKLALLVDADEGT

Results

Appropriate peptide sequence, radionuclide and chelating ligand modifications can significantly improve pHLIP-PET properties.

***In Vitro* Studies.** We made several modifications to reduce the non-specific binding of the PET probe to normal tissues in order to maximize contrast while maintaining tumor specificity. Based on reports revealing that simple replacement of a radionuclide can significantly alter the PK characteristics of a PET probe (26-28), we labeled WT and truncated versions of pHLIP from Scheme 1 with ^{68}Ga ($t_{1/2}$ ~ 68 min) in lieu of ^{64}Cu ($t_{1/2}$ ~ 12.7 h). Variants of pHLIP were conjugated with DOTA via a thioether linkage made via a nucleophilic reaction between the maleimide side chain of the macrocycle and the thiol functional group of a cysteine in pHLIP. ^{68}Ga-radiolabeling of these variants was facilitated via a microwave-assisted reaction at 90 °C for 1 min at pH~5.5. Assays performed *in vitro* were used to identify our lead pHLIP variant for studies *in vivo*. Measurements of the octanol/water partition coefficient (Log P) showed that, among the pHLIP variants tested, ^{68}Ga-DOTA-WT is the most hydrophilic (Log P ~ -2.26 ± 0.04) while ^{68}Ga-DOTA-Var7 is the most hydrophobic (Log P ~ -1.10 ± 0.05) (**Table 1**). Binding assays using PC3-wt prostate cancer cells in different pH-buffered environments (pH~ 6.3, 6.7, 7.0) showed that these peptides target cells at low pH. The binding activity of each radiolabeled pHLIP variant, expressed as "% Bound" normalized to the added amount of probe, is

displayed in **Fig. 1**. Variants WT and Var7 were selected as lead compounds for small animal PET imaging and biodistribution studies *in vivo*, due to their differential but favorable binding at low pH and significantly lower uptake at neutral pH, resulting in an improved dynamic range/contrast in the pH range of interest (pH 6 - 7.4). The control peptide, K-WT, showed a reverse trend, with enhanced binding at high pH. The lysine residues in K-WT are in their charged form at low pH, inhibiting membrane insertion, while in a more alkaline environment these lysine residues may be partially protonated, enhancing peptide-membrane interaction (29).

^{68}Ga-DOTA-WT vs. ^{68}Ga-DOTA-Var7. Encouraged by the results of our assays *in vitro*, we conducted *in vivo* experiments with subcutaneous (s.c.) PC3-wt prostate tumor xenografts. Serial PET images acquired (**SI Fig. 1**) at 1-4 h post-injection (p.i.) of ^{68}Ga-DOTA-WT demonstrate non-specific tissue binding of the probe, resulting in poor contrast visualization of the tumors implanted on the shoulder. *Ex vivo* tissue biodistribution analysis was conducted to measure the amount of probe bound to tumor and normal tissues at 1 h, 2 h, and 4 h p.i. to parallel the kinetics observed in the PET images. These data (**SI Table 1**) showed tumor uptake, expressed as % of injected dose per gram of tissue (%ID/g) at 1 h (1.87 ± 0.45 %ID/g), 2 h (2.36 ± 0.40 %ID/g) and 4 h (2.86 ± 0.75 %ID/g), in good agreement with previously reported data using ^{64}Cu, demonstrating probe affinity for the tumor (24). However, non-specific binding of ^{68}Ga-DOTA-WT to normal tissues observed in the biodistribution results (**Fig. 2A, SI Table 1**) even at 4 h p.i. explains the poor contrast seen in the PET images (**SI Fig. 1**). For example, tumor-to-healthy tissue ratios versus muscle (2.02 ±

1.97), blood (0.43 ± 0.16), liver (0.40 ± 0.05) and kidneys (0.37 ± 0.16) at 4 h p.i. were poor, necessitating further improvement (**Table 2**).

The shorter ^{68}Ga-DOTA-Var7 variant was examined in the same PC3-wt tumor model using similar methods of preparation. Compared to the WT sequence, ^{68}Ga-DOTA-Var7 exhibited significantly improved properties. From the tissue distribution (**SI Table 2**), the probe accumulation within the tumor progressed from 2.47 ± 0.19 %ID/g at 1 h to finally, 5.60 ± 0.30 %ID/g at 4 h p.i. The acquired PET images further reflected the observed tissue distribution (**SI Fig. 2**).

A direct comparative analysis between the two ^{68}Ga-labeled probes demonstrated a higher tumor uptake with the shorter sequence compared to the parent WT. The blood residence at 4 h p.i. was similar; however, slightly increased non-specific tissue binding was demonstrated by ^{68}Ga-DOTA-Var7 (**Fig. 2A**). Compared to the WT peptide, the kidney uptake for Var7 was elevated, which can be rationalized as resulting from faster probe clearance. Comparing tumor-to-background ratios of both radiotracers in **Table 2**, an overall increase in contrast with Var7 is seen. Based on these observations, Var7 was chosen as the lead pHLIP variant for further preclinical evaluation.

DOTA vs. NOTA. Even with shorter variants, the residence time of pHLIP appears longer than the physical half-life of ^{68}Ga, so we reconsidered using ^{64}Cu to better match the biological half-life of pHLIP. ^{64}Cu radiolabeling of DOTA-Var7 was conducted using methods similar to that of ^{68}Ga labeling. *Ex vivo* biodistribution results (**SI Table 3**) using PC3-wt tumor-bearing mice displayed tumor uptake at 1 h p.i. (1.19 ± 0.55 %ID/g), and significant retention after 24 h (1.64 ± 0.38 %ID/g, **Fig.**

2B). The blood residence activity improved with a final tumor-to-blood ratio of 2.63 ± 0.57 at 24 h p.i. (**Table 3**). Despite improvements made on the pHLIP backbone, concerns still remained with radiotracer retention in key organs. Hepatic uptake of the radiotracer displayed unremarkable retention over 24 h with 6.05 ± 1.36 %ID/g (**Fig. 2B-C**), similar to the values reported for the ^{64}Cu-DOTA-WT construct (4.88 ± 0.98 %ID/g at 24 h) (24); this uptake is likely to be from random scavenging of radioactive metabolites, including de-metallated ^{64}Cu in the liver (30, 31). The tracer distribution in the kidney revealed only nominal reduction, even after 24 h (19.6 ± 4.0 %ID/g), likely due to the renal acidic environment (pH~5), which is expected to cause binding of these pHLIP variants for a period of time (32), but possibly including other effects, since it could be improved (see below).

Our efforts to limit indiscriminate tissue accretion of pHLIP PET probes led us to seek improvements of the radiometal-chelate stability and the resistance to proteolytic degradation. Var7 was modified with the NOTA ligand. In addition, since previous reports described superior chelate affinity for ^{64}Cu (33-35) and, in addition, we employed D-amino acids (named Var7(D) from now on), known for resistance to enzymatic proteolysis compared to L-peptidomimetics (36-38). Similar ^{64}Cu radiolabeling conditions were employed as described above. In PC3-wt xenografts, no differences in tumor accretion were seen between ^{64}Cu-NOTA-Var7(D) (**Fig. 2B**, **SI Table 4**) and the DOTA scaffold (**Fig. 2B, SI Table 3**).

The design changes in ^{64}Cu-NOTA-Var7(D) resulted in significant improvements of several properties. First, renal accumulation showed a greatly improved, exponential clearance from 13.27 ± 0.65 %ID/g (1 h) to 5.84 ± 0.89 %ID/g (4 h) and finally, 3.86

± 1.14 %ID/g (24 h). Second, a new route of clearance - via the intestinal organs - was found (**SI Table 4**). Third, negligible hepatic radiotracer retention was seen at 24 h (0.88 ± 0.26 %ID/g, **Fig. 2B**). Finally, the significant clearance of ^{64}Cu-NOTA-Var7(D) from healthy tissues gave clear visualization of tumors as tumor-to-tissue contrasts (**Table 3**) progressed over 24 h, for example, against blood (0.81 ± 0.22), muscle (7.81 ± 0.88), liver (1.56 ± 0.40), small intestines (3.7 ± 1.0) and kidneys (0.39 ± 0.17).

PET images using ^{64}Cu-NOTA-Var7(D) acquired on mice implanted with bilateral s.c. PC3-wt (right shoulder) and LNCaP (left shoulder) xenografts exhibited promising PK properties (**Fig. 2D, left**) with progressive clearance of the tracer from the liver, muscle, gut and kidneys over 24 h, which were key problem areas with previous pHLIP PET probes.

Biophysical characterization of ^{64}Cu-NOTA-Var7(D), our lead compound.

We tested the new compound, ^{64}Cu-NOTA-Var7(D), for solubility and for the pHLIP property of pH dependent insertion to form a transmembrane helix. Sedimentation velocity measurements show that Cu-NOTA-Var7(D) forms a dimer in aqueous solution at concentrations of 7-8 μM at high and neutral pHs, in contrast to more aggregated forms of other Cu-pHLIP constructs (see **SI Table 5** and **SI Fig. 3**). The pH-dependent changes in circular dichroism (**Fig. 3A**) and tryptophan fluorescence signals (**Fig. 3B**) are similar to those observed for the peptide with no chelate and metal (25) indicating pH-dependent interaction of the pHLIP portion with the membrane. The apparent pKa of insertion was ~ 5.9 (**Fig. 3C**), which is slightly higher than for the peptide alone (5.5), probably due to the presence of the chelate.

The log P value of ^{64}Cu-NOTA-Var7(D) was measured as -2.45 ± 0.13, revealing a significantly polar compound. The properties of increased solubility and the elevation of the pK of insertion may contribute to its improved properties *in vivo*.

Probe accumulation correlates with acidity.

We wanted to explore disparities, if any, in the extacellular pH (pHe) of tumors with and without pHe regulators, particularly in tumors transduced to overexpress CAIX, a carbonic anhydrase elevated in tumor cells to cope with high CO_2 production. Thus, CAIX-transduced PC3 (PC3-CAIX) prostate cancer cells were established via the transduction of PC3-wt cells with a newly developed retroviral vector SFG-CAIX-IRES2-GFP. Via cell sorting, populations of GFP-expressing cells were collected (**SI Fig. 4A**) and Western blots confirmed higher CAIX expression in PC3-CAIX than in the wt cells under normal oxygen conditions (20 % O_2) (**SI Fig. 4B**).

The intrinsic acidity of the three prostate xenografts (PC3-wt, PC3-CAIX and LNCaP) was evaluated by measuring pHe and pHi (intracellular pH) via ^{1}H-decoupled ^{31}P-MRS using 3-APP (**Fig. 4A**). Each of the three tumor models exhibited a lower whole-tumor pHe (**Fig. 4B**) than its whole-tumor pHi (**Fig. 4C**), in concordance with previous studies (39-42). Of all the tumor models, LNCaP tumors had the highest pHi (7.28 ± 0.07) and pHe (7.07 ± 0.04) while the PC3-wt xenografts exhibited both the lowest pHi (6.94 ± 0.07) and pHe (6.93 ± 0.03). In contrast to the wt model, the CAIX-enhanced tumor implants displayed an alkaline-shifted pHi (7.26 ± 0.09, P = 0.012) and pHe (7.07 ± 0.06, P = 0.035). Analysis of the ΔpH (pHi-pHe) of these tumors revealed similar proton fluxes in LNCaP (0.27 ± 0.10, P = 0.020) and PC3-

CAIX (0.33 ± 0.13, P = 0.018), establishing greater extracellular acidification gradients in these two xenografts than in PC3-wt (-0.010 ± 0.055) (**Fig. 4D**).

Uptake of ^{64}Cu-NOTA-Var7(D) correlates inversely with pHe when data from all three tumor models are taken into account. Each mouse used for pH MRS measurements was also used for PET and biodistribution experiments, giving greater confidence in the correlations (for pairing details see **SI Table 6**). In the plot of pHe versus ^{64}Cu-NOTA-Var7(D) uptake (PET imaging at 1 h p.i. and 24 h *ex vivo* tissue sampling radioactivity assays) taken from the distribution studies (**Fig. 5A**), incremental accumulation of the radiotracer is seen as the tumor acidity increases. By pooling all data points from all prostate xenografts (**Fig. 5B**), threshold limits can be established from the data, showing that a tumor pHe < 6.9 provides high probe localization (> 3.0 %ID/g), whereas a pHe range of 6.9 – 7.4 results in lower probe uptake (< 3.0 %ID/g).

***Ex vivo* autoradiography demonstrates pHLIP accumulation in tumor regions associated with elevated metabolism**

Histological staining was used to examine viability and metabolic features of the tissues that stain or do not stain with the probe. **Figures 6A-C** shows the distribution of ^{64}Cu-NOTA-Var7(D) (autoradiography)**,** and correlative histologic markers pimonidazole (green, hypoxia), Hoechst 33342 (blue, vascular perfusion) and lactate dehydrogenase A (LDH-A, red) in representative PC3-CAIX (top row), LNCaP (middle row) and PC3-wt (bottom row) tumors. Histological stains (hematoxylin and eosin) were also conducted to determine tumor tissue viability (**SI Fig. 5**). In all tumors, the ^{64}Cu-NOTA-Var7(D) distribution is heterogeneous, with increasing

accumulation seen in perinecrotic, hypoxic tumor regions. Binding of ^{64}Cu-NOTA-Var7(D) is also observed in the animal skin, an inherent acidic tissue, indicated by the red arrows on the tumor sections. **Figures 6D-F** contains re-binned scatterplots of the relative pixel intensity values of the images shown in **Fig. 6A-C** respectively. In all cases, the regions of highest ^{64}Cu-NOTA-Var7(D) uptake corresponded with regions of highest pimonidazole and LDH-A staining, with the converse lowest ^{64}Cu-NOTA-Var7(D) corresponding to the regions of lowest LDH-A expression and pimonidazole uptake. There appeared to be no relationship between Hoechst 33342 staining intensity and ^{64}Cu-NOTA-Var7(D) uptake. Thus, we find that probe uptake is correlated with hypoxia and LDH-A.

Discussion

By creating a useful probe for imaging tumor acidosis, we enable assessment of a universal trait associated with tumor invasiveness in most malignancies. We illustrated the improvements made toward better PK and dosimetric properties of pHLIP as a non-invasive PET radiotracer. More importantly, this probe was able to distinguish highly acidic tumors, with a direct association to tumor pHe. Furthermore, we extended our efforts to understanding the mechanism of uptake of this probe through autoradiographic and histologic studies of all three tumor models to provide insights on its target.

Based on a set of observations with earlier pHLIP-based probes, we were able to design a new version that should prove useful in clinical applications. The Var7 variant sequence of pHLIP proved to offer faster clearance and tumor delivery than the parent pHLIP; however, its prolonged residence in healthy tissue paired with the short

physical half-life of ^{68}Ga was mismatched, and degradation of the peptide was suspected. To cope with these we synthesized the peptide from D-amino acids and revisited the use of ^{64}Cu, which has a longer half-life to allow clearance of the probe from healthy tissue. The relatively poor chelating properties of DOTA for ^{64}Cu had resulted in accumulation of unbound Cu in tissues (i.e. liver) (31), so we searched for a better chelation group, deciding on NOTA. This set of design choices gave us ^{64}Cu-NOTA-Var7(D)**.** The superiority of NOTA to DOTA is clear in the comparisons of biodistribution, tumor-to-tissue contrast ratios and PET imaging (**Fig. 2C-D, SI Tables 3-4**). A much lower uptake is seen in the liver, intestines, spleen and kidneys, resulting in improved contrast ratios between these tissues and the tumor. We now have a workable probe to develop for clinical use.

Our results differ in some respects from those reported earlier. In our hands, comparison of two of the tumor models (LNCaP and PC3 wt) in the right shoulder of athymic nude mice, the pHe showed a trend opposite to that observed by Vavere *et al.* (24). They also used LNCaP and PC3 but for tumors implanted in the flanks of athymic nu/nu mice and for tumor volumes > 500 mm^3, so the observed differences may potentially be due to the smaller tumor size (< 400 mm^3) used in our study and the differences in tumor location (shoulder vs flank). Our goal was to use tumors with only moderate necrosis for best comparison with tumors seen in the clinic, hence our choice of small to medium-sized tumors. Further, we used ^{1}H decoupled ^{31}P MRS, which may influence the average chemical shift of 3-APP, since without ^{1}H decoupling the signal shape and width is not only determined by T_2 relaxation and the pHe tissue distribution, but also by the multiplet structure of 3-APP (43). We did not

find a significant relationship between tumor size and pHe for tumors < 400 mm^3 (**SI Table 6**), which is consistent with the data by Raghunand *et al.* where tumoral pH was observed to decrease over a tumor size range of ~ 200 – 1500 mm^3 (42), while not significantly decreasing in smaller tumors (< 400 mm^3). Although decreases of mean tumor pHe and pHi with increasing tumor size have been observed in rodent tumors when measured over a large tumor size range (40, 42), in human tumors both decreasing pH with increasing tumor size and a lack of such a relationship have been reported (44).

In retrospect, we find that the outcomes of measuring pH as an average do not give a true representation of tumor acidity, as evidenced by the broad pH distributions observed from ^{31}P MRS. Instead, details of pH variation within a tumor may be key, even at the cellular level. Variations in the spatial distribution of pHe have been reported such that gradients exist at the interface of the cellular membrane and cytosol (45, 46), prompting us to examine the differences between cytosolic and extracellular pH, and to derive the net proton flux (although we still needed to use average values). We observed that the transduced PC3-CAIX and the LNCaP implants had greater extracellular pH gradients (ΔpH) than the wild type (PC3-wt) model; however, the measured pHe values of the two models followed an opposite trend from the ΔpH values. We rationalize that these contrasting measurements may be due to the vast heterogeneity in tumor homeostasis and development, governed by an intricate mesh of metabolic pathways including rate of glycolytic metabolism, expression of acid extruding protein, and diverse buffering capacities and O_2 concentrations in the blood vessel network, to name a few (44, 47, 48). Despite these uncertainties, we observed a

correlation of targeting with absolute pHe, where at a pHe < 6.9, higher tumor accumulation of the radiotracer was observed, with > 3 %ID/g. However, at pHe > 6.9, measuring and imaging tumor acidity using this probe is poorly resolved. We postulate that this may be an effect of the insertion pKa of the full construct (pKa ~ 5.9).

The development and use of pHLIP variants with a higher and lower pKs of insertion across cellular membranes, combined with favorable thermodynamics and kinetics properties, would allow measurement of a wider dynamic range of potential extracellular pH probed by pHLIP-technology. Also, pHLIP variants tuned over a pKa range could expand the applicability of minimally invasive pH measurements to applications beyond cancer. Thus, pHLIP-based acidosis imaging probes may offer a relative read-out of distributions of pHe, which may in turn allow clinical analysis of tumor invasiveness and regionalization. As we move forward, associating pHLIP tumor uptake with tumor acidosis using a regional pHe map is deemed more appropriate; these studies are currently underway.

Autoradiography and histology performed on excised tumor sections revealed a heterogeneous distribution of ^{64}Cu-NOTA-Var7(D) within the tumors, again emphasizing the need to avoid gross averaging of pH measurements to solely correlate the target/s of our probe with markers related to acidity. We used pimonidazole (a hypoxia tracer) and LDH-A (involved in the interconversion of pyruvate and lactate) as markers for comparison with the pHLIP distribution, in the absence of a direct histological marker of low pHe. ^{64}Cu-NOTA-Var7(D) localization appears preferentially in perinecrotic regions (**SI Fig. 5**) that display high uptake of the

hypoxia marker pimonidazole, but shows no clear relationship to the vascular perfusion marker Hoechst 33342 (**Fig. 6**). The LDH-A-mediated conversion of pyruvate to lactate is postulated to be one of the principal sources of tumor acidity (49, 50); elevated LDH-A would be expected to result in concomitant elevated pHLIP binding.

LDH-A expression, while previously been shown to be hypoxia-regulated (via the HIF-1 transcription factor), has not yet been individually validated as a marker of low pHe (51). However, for these studies we took elevated expression of LDH-A as a stable marker of regional lactic acidosis, which is not susceptible to perfusion-mediated fluctuations in extracellular microenvironment (52). The predicted cellular half-life of LDH-A is tissue-type dependent, but is generally in the order of several days (53), which is appropriate to our experimental protocols.

The expression of CAIX, which could also be taken to indicate regions of lowered pHe, is similarly regulated by HIF-1, and has a similar cellular half-life to LDH-A (54). While arguably inversely related to lowered pHe, both LDH-A and CAIX expression cannot be assumed to linearly relate to absolute pHe. Taken together with the induced, constitutive CAIX expression in the PC3-CAIX model and the very low observed CAIX expression in the LNCaP model, these facts render CAIX expression an unsuitable marker for low pHe or pO_2 in our study. For these reasons, we also included pimonidazole binding in our analysis. Unlike LDH-A expression, there is no reported protein biomarker dependence of pimonidazole uptake, and its affinity is primarily dependent on low pO_2, making pimonidazole a general marker of a hypoxic

tumor microenvironment (55). Our data demonstrate that, in the tumor models used in this study, LDH-A expression and pimonidazole binding have similar but discordant spatial distributions, in good agreement with previous reports that lactic acidosis and hypoxia are not always interdependent (10, 46, 48). It is likely that tumor regions of poor vascularity and low pO_2 will also possess excess extracellular H^+ ions due to anaerobic glucose metabolism and local lactic acidosis. While we observed a trend towards increasing ^{64}Cu-NOTA-Var7(D) uptake with increasing pimonidazole uptake, the relationship appears to be non-linear (**Fig. 6C-D**). This may in part be due to the effect of pHe on absolute pimonidazole uptake, although this is likely to be a minor effect over the pHe ranges measured in this study (56).

By finding a probe that marks the acidosis inherent in tumor metabolism, we have defined a new clinical potential for marking tumors and measuring their aggressive characteristics. Defining a probe with usable imaging properties could allow it to be used to follow the progression of a tumor and to monitor the effects of therapy.

Methods

Additional details of materials, methods and equipment used are found in the provided supplemental information**.**

Synthesis, purification and characterization of DOTA- and NOTA-conjugates of pHLIP. Variants of pHLIP were synthesized and purchased from C.S. Bio Co. Inc. (Menlo Park, CA). Peptides were derivatized with either maleimido-monoamide-DOTA (Macrocyclics, Inc., Dallas, TX) or *p*-SCN-Bn-NOTA (Macrocyclics, Inc., Dallas, TX).

Radiolabeling and purification with $^{68}GaCl_3$ and $^{64}CuCl_2$. Radiolabeling of pHLIP-DOTA or -NOTA with ^{68}Ga or ^{64}Cu was conducted via a microwave-assisted reaction at 90 °C at 1 min. in 0.5 M ammonium acetate, pH ~ 5.5. Unbound radiometal was removed via a C18 solid phase extraction cartridge (Grace, Deerfield, Il). The pure labeled peptide was eluted with 0.5% 2 M HCl in ethanol. Radiochemical purities of > 95% were ensured before administering to animals.

Cell Culture and Growth. All tissue culture manipulations were conducted under a laminar flow hood using aseptic technique. LNCaP prostate cancer cells were grown as adherent monolayers in RPMI 1640 (GE Healthcare, Austria) containing 2 mM glutamine, 10 mM HEPES, 1 mM sodium pyruvate, 4.5 g/L glucose, and 1.5 g/L sodium bicarbonate. PC3-CAIX and PC3-wt cells were cultured in RPMI 1640 containing 2 mM L-glutamine. All media were supplemented with 10% fetal calf serum, 100 units/mL penicillin and 100 µg/mL streptomycin. Cells were grown in a 5% CO_2 atmosphere at 37 □C to 80% confluence and harvested with 0.25% Trypsin and 0.53 mM EDTA in Hank's Buffered Salt Solution (HBSS) with no calcium or magnesium present.

***In vitro* cell binding.** PC3-wt cells were incubated with different ^{68}Ga-labeled pHLIP-DOTA variants for 1 h at 37 °C at different pH ranging ~ 6.3 - 7.0. The cells were then washed twice with the same media used for incubation to remove unbound activity and the retained activity was counted using a Wizard^2 2480 gamma counter (Perkin Elmer).

pH-dependence. The pH-dependent partitioning of the peptides into lipid bilayers using POPC liposomes was investigated by measuring the shift of the intrinsic

fluorescence spectral maximum of the peptide as the pH is lowered from pH 8 to 2, as previously described (25). The spectra were analyzed by decomposition algorithms using an on-line PFAST toolkit (Protein Fluorescence and Structural Toolkit: http://pfast.phys.uri.edu/) to obtain spectral maxima (λ_{max}). Finally, the positions of the fluorescence spectral maxima (λ_{max}) of the single component solutions were plotted versus pH and the Henderson–Hasselbalch equation was used to fit the data:

$$\lambda_{max} = \lambda^2_{max} + \frac{(\lambda^1_{max} - \lambda^2_{max})}{1 + 10^{(pH-pKa)}}$$

where λ^1_{max} and λ^2_{max} are the beginning and end of the transition, and the pKa is the midpoint of the transition.

Steady-state fluorescence and circular dichroism measurements. Tryptophan fluorescence and circular dichroism (CD) measurements were carried out on a PC1 ISS spectrofluorometer (ISS, Inc.) and a MOS-450 spectrometer (Biologic, Inc.), respectively, at 25 ºC, as previously reported (25).

Partition coefficient. The log P values (n=3) were determined for each labeled peptide by measuring the amount of activity from equal volume of samples obtained from the octanol and 1×PBS (pH~7) layers.

Cell transduction. Stable clones of PC3-CAIX were developed by transducing PC3-wt cell with SFG-CAIX-IRES2-GFP. PC3-wt cells at ~50% confluence were incubated with virus-containing medium for 12 hours in the presence of polybrene (8 mg/ml; Sigma, St.Louis, MO, USA) as previously described (57). Cells were sorted several times using a fluorescence-activated cell sorter (FACS; BD Bioscience, CA, USA) (**SI Fig. 4A)** with Western blot experiments confirming CAIX expression (**SI Fig. 4B**).

Animal models. All animals were treated according to the guidelines set by the Institutional Animal Care and Use Committee. Tumors were induced in male, athymic nu/nu mice (Taconic Farms, Inc., Hudson, NY or Harlan Laboratories, Indianapolis, IN) on the shoulder by subcutaneous injection of 3×10^6 million cells of either PC3-wt, PC3-CAIX or LNCaP cells in a 200 μL suspension of 1:1 media:Matrigel Basement Membrane Matrix (BD Sciences, Bedford, MA). Mice were utilized once volumes reached 150-300 mm^3.

***In vivo* animal PET imaging and biodistribution.** Imaging experiments were accomplished with a microPET Focus 120 or R4 scanner (Concorde Microsystems). Mice (n=3-5) were administered with $^{68}Ga/^{64}Cu$-radiolabeled pHLIP variants (200-300 μCi, 15-25 μg) in 100-200 μL 0.9% saline formulations via lateral tail vein injections. PET whole body acquisitions were recorded on mice at 1-24 h p.i., while anesthetized with 1.5-2.0% isofluorane (Baxter Healthcare) in air. The images were analyzed using ASIPro VM™ software (Concorde Microsystems). Regions-of-interest (ROI) were drawn and plotted vs. time.

Biodistribution studies were performed on male athymic nu/nu mice bearing separate subcutaneous prostate xenografts (n=3-5). ^{68}Ga- or ^{64}Cu-radiolabeled pHLIP variants (20-50 μCi, 1-2 μg) in 100 μL 0.9 % saline were administered intravenously on the lateral vein. At a predetermined timepoint (1-24 h), the mice were euthanized by asphyxiation with CO_2. Blood was collected immediately via cardiac puncture while the tumor along with chosen organs was harvested. The radioactivity bound to each organ was counted using a gamma counter. The percentage of tracer uptake expressed as % injected dose per gram (%ID/g) was calculated as the activity bound to

the tissue per organ weight per actual injected dose and decay-corrected to the time of counting.

For studies demonstrating correlation of extracellular acidification and pHLIP-PET, pH, PET imaging and biodistribution measurements were conducted on the same tumors. On the same mice, ^{64}Cu-NOTA-Var7(D) was administered intravenously post-MRS. PET images were acquired at 1-24 h p.i. with the mice subsequently euthanized after the last scan for *ex vivo* tissue analysis. Pairing of tumors is detailed in **SI Table 6**.

***In Vivo* pH Measurements by ^{1}H-decoupled ^{31}P Magnetic Resonance Spectroscopy (MRS).** The MR experiments were performed on a horizontal-bore 7T MR spectrometer (Bruker, Germany) using a home-built ^{1}H / ^{31}P MR coil assembly. Prior to the MR measurements, a tail vein catheter was inserted, facilitating the administration of 3-APP via a home-built catheter line assembly during the MR experiment. For the duration of the MR experiment, the mice were kept anesthetized with < 2% isoflurane in 100% oxygen and the core temperature was maintained at 34-37°C. A bolus of 480 mg/kg 3-APP was injected i.v. via the tail vein catheter directly before the acquisition of a ^{1}H-decoupled ^{31}P MR single pulse spectrum averaged over 17 min 4 s, acquired using a 60° excitation pulse, 2 s relaxation delay, 10 kHz spectral width, 2048 points, and 512 averages. Directly following the first acquisition, a 2nd bolus of 480 mg/kg 3-APP was injected *i.v.* and a 2nd ^{1}H-decoupled ^{31}P MR spectrum acquired. For each tumor, the free induction decays (FIDs) of the two ^{31}P MR spectra were added up, resulting in a 34 min 8 s MR spectrum, and an exponential line broadening of 20 Hz applied. The resulting FIDs were Fourier transformed, phase

corrected, and the α-NDP/α-NTP signal calibrated to -10.05 ppm (**Fig. 4A**). The MR spectra were fitted in the time domain, using the software package XsOsNMR (kindly provided by Dr. Dikoma Shungu and Xiaoling Mao) and the intracellular and extracellular pH (pHi, pHe) calculated from the chemical shifts of inorganic phosphate (Pi) and 3-aminopropylphosphonate (3-APP) respectively, described previously (43). The inorganic phosphate signal, Pi represents primarily intracellular pH (pHi) (58, 59). The chemical shifts δ of Pi and 3-APP relative to α-NTP at -10.05 ppm, δ(Pi) and δ(3-APP) respectively, are related to pHi and pHe by their respective Henderson-Hasselbach equations and calculated as follows:

$$\mathrm{pHi} = 6.85 + \log_{10}\frac{\delta(\mathrm{Pi}) - 0.58}{3.14 - \delta(\mathrm{Pi})}$$

$$\mathrm{pHe} = 6.91 + \log_{10}\frac{\delta(\text{3-APP}) - 21.10}{24.32 - \delta(\text{3-APP})}$$

pH values were reported as the mean ± standard error of the mean (SEM).

Autoradiography and fluorescence microscopy. Animals were intravenously administered 80 mg/kg pimonidazole hydrochloride (Hypoxyprobe-1, NPI, Burlington, MA) in a final injection volume of 200 μL 1 h before sacrifice. Hoechst 33342 trihydrochloride (Sigma; 1mg in 100 μL of physiologic saline) was injected 5 min before euthanizing. Following sacrifice, tumors were excised and embedded in OCT mounting medium (Optimal Cutting Temperature (OCT), Sakura Finetek, CA), frozen on dry ice, and cut in several 10 μm sections throughout the tumor. Digital autoradiography (DAR) was performed by placing tissue sections in a film cassette against a phosphor imaging plate (Fujifilm BAS-MS2325) for an appropriate exposure period at -20 ºC. Phosphor imaging plates were read at a pixel resolution of 25 μm ×

25 μm in-plane resolution using a Typhoon FLA 7000IP (General Electric, USA) phosphor imager. Following autoradiographic exposure, the same or sequential sections were then used for fluorescence and H&E staining and microscopy.

Immunofluorescence staining for pimonidazole was carried out as previously described (54), the major difference being the use of a rabbit polyclonal anti-pimonidazole primary antibody (NPI). Secondary detection was carried out using goat anti-rabbit Alexa-488 (Invitrogen, Grand Island, NY) (1:100 in blocking buffer). Images were acquired as previously described (60). Lactate dehydrogenase A (LDH-A) staining was carried out using a rabbit polyclonal anti-LDH-A antibody (Novus Biologicals, NBP1-48336, 1:50), and secondary detection with goat anti-rabbit Alexa-568 (Invitrogen). Whole tumor montage images were obtained by acquiring multiple fields at 40× magnification, followed by alignment using MicroSuite Biological Suite (version 2.7, Olympus USA).

Pixel re-binning and scatterplot generation

Pixel re-binning was done using an adaptation of the methods described in (61) and (62). Briefly, registered image sets were re-sampled to 50×50×10 μm^3 pixel size, each image converted to an 8-bit grayscale image, and pixel values with their corresponding image location recorded. The data from the DAR image was designated as independent and the fluorescence image data as dependent. Data were then sorted in ascending order of the independent variable while maintaining the association between independent and dependent values. The data set was then split into deciles, each containing the same number of data points, i.e. the 10% of the data points lowest in terms of the independent variable, then the next lowest 10%, etc.

Statistical Analysis

Data values were expressed as the mean ± S.D. unless otherwise stated. Statistical analysis was performed using GraphPad Prism version 5.03 software using student's t-test. A *P* value of < 0.05 is considered statistically significant.

Acknowledgements

This work was funded by NIH R01 CA138468 (J.S.L.). Acknowledgements are also extended to the grant-funding support provided by the NIH Small-Animal Imaging Research Program (SAIRP, R24-CA83084) and the NIH MSKCC Center Grant (P30-CA08748). The authors would like to express their deep appreciation to Dr. Pat Zanzonico, Dr. Alexander Karabadzhak, Valerie Longo, Blesida Punzalan, Nick Ramos, and Charles Davis for technical assistance.

References

1. Gottfried E, Kreutz M, & Mackensen A (2012) Tumor metabolism as modulator of immune response and tumor progression. *Semin Cancer Biol* 22(4):335-341.

2. Vander Heiden MG, Cantley LC, & Thompson CB (2009) Understanding the Warburg effect: the metabolic requirements of cell proliferation. *Science* 324(5930):1029-1033.

3. Chiche J, Brahimi-Horn MC, & Pouyssegur J (2010) Tumour hypoxia induces a metabolic shift causing acidosis: a common feature in cancer. *J Cell Mol Med* 14(4):771-794.

4. Guillaumond F, *et al.* (2013) Strengthened glycolysis under hypoxia supports tumor symbiosis and hexosamine biosynthesis in pancreatic adenocarcinoma. *Proc Natl Acad Sci U S A* 110(10):3919-3924.

5. Park HJ, Lyons JC, Ohtsubo T, & Song CW (1999) Acidic environment causes apoptosis by increasing caspase activity. *Br J Cancer* 80(12):1892-1897.

6. Williams AC, Collard TJ, & Paraskeva C (1999) An acidic environment leads to p53 dependent induction of apoptosis in human adenoma and carcinoma cell

lines: implications for clonal selection during colorectal carcinogenesis. *Oncogene* 18(21):3199-3204.

7. Neri D & Supuran CT (2011) Interfering with pH regulation in tumours as a therapeutic strategy. *Nat Rev Drug Discov* 10(10):767-777.

8. Zhang X, Lin Y, & Gillies RJ (2010) Tumor pH and its measurement. *J Nucl Med* 51(8):1167-1170.

9. Rodriguez-Enriquez S, Gallardo-Perez JC, Marin-Hernandez A, & Moreno-Sanchez R (2012) The Warburg Hypothesis and the ATP Supply In Cancer Cells Is Oxidative Phosphorylation impaired in malignant neoplasias? *Curr Pharm Biotechnol*.

10. Mazzio EA, Boukli N, Rivera N, & Soliman KF (2012) Pericellular pH homeostasis is a primary function of the Warburg effect: inversion of metabolic systems to control lactate steady state in tumor cells. *Cancer Sci* 103(3):422-432.

11. de Groof AJ, *et al.* (2009) Increased OXPHOS activity precedes rise in glycolytic rate in H-RasV12/E1A transformed fibroblasts that develop a Warburg phenotype. *Mol Cancer* 8:54.

12. Wu M, *et al.* (2007) Multiparameter metabolic analysis reveals a close link between attenuated mitochondrial bioenergetic function and enhanced glycolysis dependency in human tumor cells. *Am J Physiol Cell Physiol* 292(1):C125-136.

13. Gatenby RA & Gillies RJ (2004) Why do cancers have high aerobic glycolysis? *Nat Rev Cancer* 4(11):891-899.

14. Carmeliet P, *et al.* (1998) Role of HIF-1alpha in hypoxia-mediated apoptosis, cell proliferation and tumour angiogenesis. *Nature* 394(6692):485-490.

15. Martinez-Zaguilan R, *et al.* (1996) Acidic pH enhances the invasive behavior of human melanoma cells. *Clin Exp Metastasis* 14(2):176-186.

16. Schlappack OK, Zimmermann A, & Hill RP (1991) Glucose starvation and acidosis: effect on experimental metastatic potential, DNA content and MTX resistance of murine tumour cells. *Br J Cancer* 64(4):663-670.

17. Jang A & Hill RP (1997) An examination of the effects of hypoxia, acidosis, and glucose starvation on the expression of metastasis-associated genes in murine tumor cells. *Clin Exp Metastasis* 15(5):469-483.

18. An M, Wijesinghe D, Andreev OA, Reshetnyak YK, & Engelman DM (2010) pH-(low)-insertion-peptide (pHLIP) translocation of membrane impermeable phalloidin toxin inhibits cancer cell proliferation. *Proc Natl Acad Sci U S A* 107(47):20246-20250.

19. Andreev OA, Engelman DM, & Reshetnyak YK (2010) pH-sensitive membrane peptides (pHLIPs) as a novel class of delivery agents. *Mol Membr Biol* 27(7):341-352.

20. Moshnikova A, Moshnikova V, Andreev OA, & Reshetnyak YK (2013) Antiproliferative Effect of pHLIP-Amanitin. *Biochemistry*.

21. Daumar P, *et al.* (2012) Efficient (18)F-labeling of large 37-amino-acid pHLIP peptide analogues and their biological evaluation. *Bioconjug Chem* 23(8):1557-1566.

22. Yao L, Daniels J, Wijesinghe D, Andreev OA, & Reshetnyak YK (2013) pHLIP((R))-Mediated Delivery of PEGylated Liposomes to Cancer Cells. *J Control Release*.

23. Andreev OA, *et al.* (2010) pH (low) insertion peptide (pHLIP) inserts across a lipid bilayer as a helix and exits by a different path. *Proc Natl Acad Sci U S A* 107(9):4081-4086.

24. Vavere AL, *et al.* (2009) A novel technology for the imaging of acidic prostate tumors by positron emission tomography. *Cancer Res* 69(10):4510-4516.

25. Weerakkody D, *et al.* (2013) Family of pH (low) insertion peptides for tumor targeting. *Proc Natl Acad Sci U S A* 110(15):5834-5839.

26. Antunes P, *et al.* (2007) Are radiogallium-labelled DOTA-conjugated somatostatin analogues superior to those labelled with other radiometals? *Eur J Nucl Med Mol Imaging* 34(7):982-993.

27. Chakraborty S & Liu S (2010) (99m)Tc and (111)In-labeling of small biomolecules: bifunctional chelators and related coordination chemistry. *Curr Top Med Chem* 10(11):1113-1134.

28. Wadas TJ, Wong EH, Weisman GR, & Anderson CJ (2010) Coordinating radiometals of copper, gallium, indium, yttrium, and zirconium for PET and SPECT imaging of disease. *Chem Rev* 110(5):2858-2902.

29. Andreev OA, *et al.* (2007) Mechanism and uses of a membrane peptide that targets tumors and other acidic tissues in vivo. *Proc Natl Acad Sci U S A* 104(19):7893-7898.

30. Anderson CJ (2001) Metabolism of radiometal-labeled proteins and peptides: what are the real radiopharmaceuticals in vivo? *Cancer Biother Radiopharm* 16(6):451-455.

31. Bass LA, Wang M, Welch MJ, & Anderson CJ (2000) In vivo transchelation of copper-64 from TETA-octreotide to superoxide dismutase in rat liver. *Bioconjug Chem* 11(4):527-532.

32. Feng B, LaPerle JL, Chang G, & Varma MV (2010) Renal clearance in drug discovery and development: molecular descriptors, drug transporters and disease state. *Expert Opin Drug Metab Toxicol* 6(8):939-952.

33. Ait-Mohand S, *et al.* (2011) Evaluation of 64Cu-labeled bifunctional chelate-bombesin conjugates. *Bioconjug Chem* 22(8):1729-1735.

34. De Silva RA, *et al.* (2012) Copper-64 radiolabeling and biological evaluation of bifunctional chelators for radiopharmaceutical development. *Nucl Med Biol* 39(8):1099-1104.

35. Simecek J, Wester HJ, & Notni J (2012) Copper-64 labelling of triazacyclononane-triphosphinate chelators. *Dalton Trans* 41(45):13803-13806.

36. Li C, McCarthy JB, Furcht LT, & Fields GB (1997) An all-D amino acid peptide model of alpha1(IV)531-543 from type IV collagen binds the alpha3beta1 integrin and mediates tumor cell adhesion, spreading, and motility. *Biochemistry* 36(49):15404-15410.

37. Brugidou J, Legrand C, Mery J, & Rabie A (1995) The retro-inverso form of a homeobox-derived short peptide is rapidly internalised by cultured neurones: a new basis for an efficient intracellular delivery system. *Biochem Biophys Res Commun* 214(2):685-693.

38. Fischer PM (2003) The design, synthesis and application of stereochemical and directional peptide isomers: a critical review. *Curr Protein Pept Sci* 4(5):339-356.

39. Gillies RJ, Raghunand N, Garcia-Martin ML, & Gatenby RA (2004) pH imaging. A review of pH measurement methods and applications in cancers. *IEEE Eng Med Biol Mag* 23(5):57-64.

40. Gillies RJ, Raghunand N, Karczmar GS, & Bhujwalla ZM (2002) MRI of the tumor microenvironment. *J Magn Reson Imaging* 16(4):430-450.

41. Vaupel P, Kallinowski F, & Okunieff P (1989) Blood flow, oxygen and nutrient supply, and metabolic microenvironment of human tumors: a review. *Cancer Res* 49(23):6449-6465.

42. Raghunand N, *et al.* (1999) Plasmalemmal pH-gradients in drug-sensitive and drug-resistant MCF-7 human breast carcinoma xenografts measured by 31P magnetic resonance spectroscopy. *Biochem Pharmacol* 57(3):309-312.

43. Raghunand N (2006) Tissue pH measurement by magnetic resonance spectroscopy and imaging. *Methods Mol Med* 124:347-364.

44. Tannock IF & Rotin D (1989) Acid pH in tumors and its potential for therapeutic exploitation. *Cancer Res* 49(16):4373-4384.

45. Paradise RK, Whitfield MJ, Lauffenburger DA, & Van Vliet KJ (2013) Directional cell migration in an extracellular pH gradient: a model study with an engineered cell line and primary microvascular endothelial cells. *Exp Cell Res* 319(4):487-497.

46. Helmlinger G, Yuan F, Dellian M, & Jain RK (1997) Interstitial pH and pO2 gradients in solid tumors in vivo: high-resolution measurements reveal a lack of correlation. *Nat Med* 3(2):177-182.

47. Thistlethwaite AJ, Leeper DB, Moylan DJ, 3rd, & Nerlinger RE (1985) pH distribution in human tumors. *Int J Radiat Oncol Biol Phys* 11(9):1647-1652.

48. Molavian HR, Kohandel M, Milosevic M, & Sivaloganathan S (2011) Deriving mechanisms responsible for the lack of correlation between hypoxia and acidity in solid tumors. *PLoS One* 6(12):e28101.

49. Chen JL, *et al.* (2008) The genomic analysis of lactic acidosis and acidosis response in human cancers. *PLoS Genet* 4(12):e1000293.

50. Dhup S, Dadhich RK, Porporato PE, & Sonveaux P (2012) Multiple biological activities of lactic acid in cancer: influences on tumor growth, angiogenesis and metastasis. *Curr Pharm Des* 18(10):1319-1330.

51. Semenza GL (2008) Tumor metabolism: cancer cells give and take lactate. *J Clin Invest* 118(12):3835-3837.

52. Al-Husari M & Webb SD (2013) Theoretical predictions of lactate and hydrogen ion distributions in tumours. *PLoS One* 8(8):e72020.

53. Nadal-Ginard B (1978) Regulation of lactate dehydrogenase levels in the mouse. *J Biol Chem* 253(1):170-177.

54. Russell J, *et al.* (2009) Immunohistochemical detection of changes in tumor hypoxia. *Int J Radiat Oncol Biol Phys* 73(4):1177-1186.

55. Arteel GE, Thurman RG, Yates JM, & Raleigh JA (1995) Evidence that hypoxia markers detect oxygen gradients in liver: pimonidazole and retrograde perfusion of rat liver. *Br J Cancer* 72(4):889-895.

56. Kleiter MM, *et al.* (2006) A comparison of oral and intravenous pimonidazole in canine tumors using intravenous CCI-103F as a control hypoxia marker. *Int J Radiat Oncol Biol Phys* 64(2):592-602.

57. Serganova I, *et al.* (2004) Molecular imaging of temporal dynamics and spatial heterogeneity of hypoxia-inducible factor-1 signal transduction activity in tumors in living mice. *Cancer Res* 64(17):6101-6108.

58. Soto GE, Zhu Z, Evelhoch JL, & Ackerman JJ (1996) Tumor 31P NMR pH measurements in vivo: a comparison of inorganic phosphate and intracellular 2-deoxyglucose-6-phosphate as pHnmr indicators in murine radiation-induced fibrosarcoma-1. *Magn Reson Med* 36(5):698-704.

59. Prichard JW, Alger JR, Behar KL, Petroff OA, & Shulman RG (1983) Cerebral metabolic studies in vivo by 31P NMR. *Proc Natl Acad Sci U S A* 80(9):2748-2751.

60. Li XF, *et al.* (2007) Visualization of hypoxia in microscopic tumors by immunofluorescent microscopy. *Cancer Res* 67(16):7646-7653.

61. Carlin S, *et al.* (2009) In vivo characterization of a reporter gene system for imaging hypoxia-induced gene expression. *Nucl Med Biol* 36(7):821-831.

62. Carlin S, *et al.* (2010) Molecular targeting of carbonic anhydrase IX in mice with hypoxic HT29 colorectal tumor xenografts. *PLoS One* 5(5):e10857.

Tables

Table 1. Tumor-to-background tissue contrast ratios [mean ± SD (rel. u.)] obtained for the ^{68}Ga-labeled WT and Var7 variants at 4 h p.i. and for ^{64}Cu-Var7 with either DOTA or NOTA as a ligand at 24 h p.i

T/B	^{68}Ga-DOTA-WT	^{68}Ga-DOTA-Var7	^{64}Cu-DOTA-Var7	^{64}Cu-NOTA-Var7(D)
Tumor/blood	0.43 ± 0.16	0.69 ± 0.18	2.63 ± 0.57	0.81 ± 0.22
Tumor/liver	0.40 ± 0.05	0.61 ± 0.15	0.28 ± 0.08	1.56 ± 0.40
Tumor/kidney	0.37 ± 0.16	0.02 ± 0.01	0.08 ± 0.01	0.39 ± 0.17
Tumor/muscle	2.02 ± 1.97	3.17 ± 0.91	7.81 ± 1.78	7.81 ± 0.88
Tumor/bone	0.25 ± 0.13	0.57 ± 0.41	1.94 ± 0.41	6.04 ± 2.34

Absolute uptake values are listed in Table S2 for ^{68}Ga-DOTA-WT, Table S3 for ^{68}Ga-DOTA-Var7, Table S4 for ^{64}Cu-DOTA-Var7, and Table S5 for ^{64}Cu-NOTA-Var7(D). rel. u., relative units; T/B, tumor-to-background tissue.

Table 1. Partition coefficients (mean ± S.D.) of ^{68}Ga-labeled pHLIP-DOTA variants show different lipophilic characteristics.

Table 2. Tumor-to-tissue contrast ratios obtained for the ^{68}Ga labeled WT and Var7 variants at 4 h p.i.

Tissue	^{68}Ga-DOTA-WT	^{68}Ga-DOTA-Var7
Blood	**0.43 ± 0.16**	**0.69 ± 0.18**
Liver	**0.40 ± 0.05**	**0.61 ± 0.15**
Kidney	**0.37 ± 0.16**	**0.02 ± 0.01**
Muscle	**2.02 ± 1.97**	**3.17 ± 0.91**
Bone	**0.25 ± 0.13**	**0.57 ± 0.41**

Table 2. Tumor-to-tissue contrast ratios (mean ± S.D., [rel. u.]) obtained for the ^{68}Ga labeled WT and Var7 variants at 4 h p.i.

Table 3. Tumor-to-tissue contrast ratios obtained for ^{64}Cu-Var7 with either DOTA or NOTA as ligands.

Tissue	^{64}Cu-DOTA-Var7	^{64}Cu-NOTA-Var7(D)
Blood	**2.63 ± 0.57**	**0.81 ± 0.22**
Liver	**0.28 ± 0.08**	**1.56 ± 0.40**
Kidney	**0.08 ± 0.01**	**0.39 ± 0.17**
Muscle	**7.81 ± 1.78**	**7.81 ± 0.88**
Bone	**1.94 ± 0.41**	**6.04 ± 2.34**

Table 3. Tumor-to-tissue contrast ratios (mean ± S.D. [rel. u.]) obtained for ^{64}Cu-Var7 with either DOTA or NOTA as ligands at 24 h p.i.

Figures

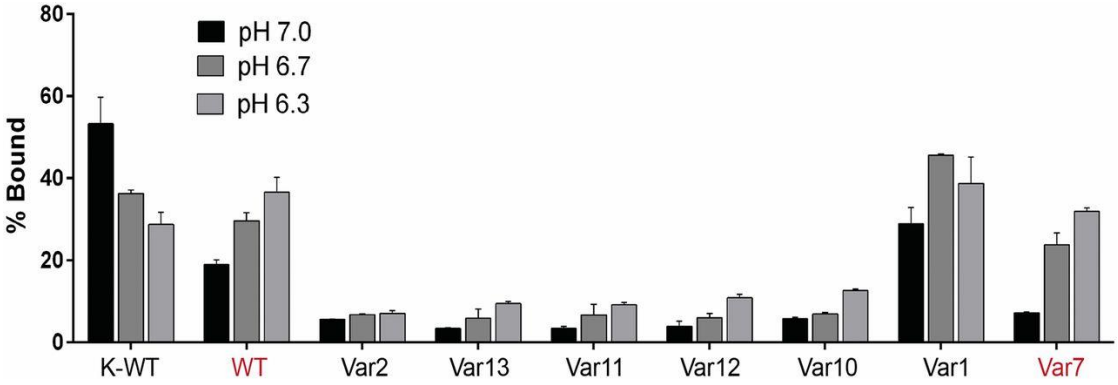

Figure 1. ^{68}Ga-DOTA-labeled pHLIP variants. *In vitro* binding studies (n=3) display higher binding of ^{68}Ga-DOTA-WT and ^{68}Ga-DOTA-Var7 variants as the pH of the incubation medium is decreased. Note that the opposite was observed with the control peptide, K-WT.

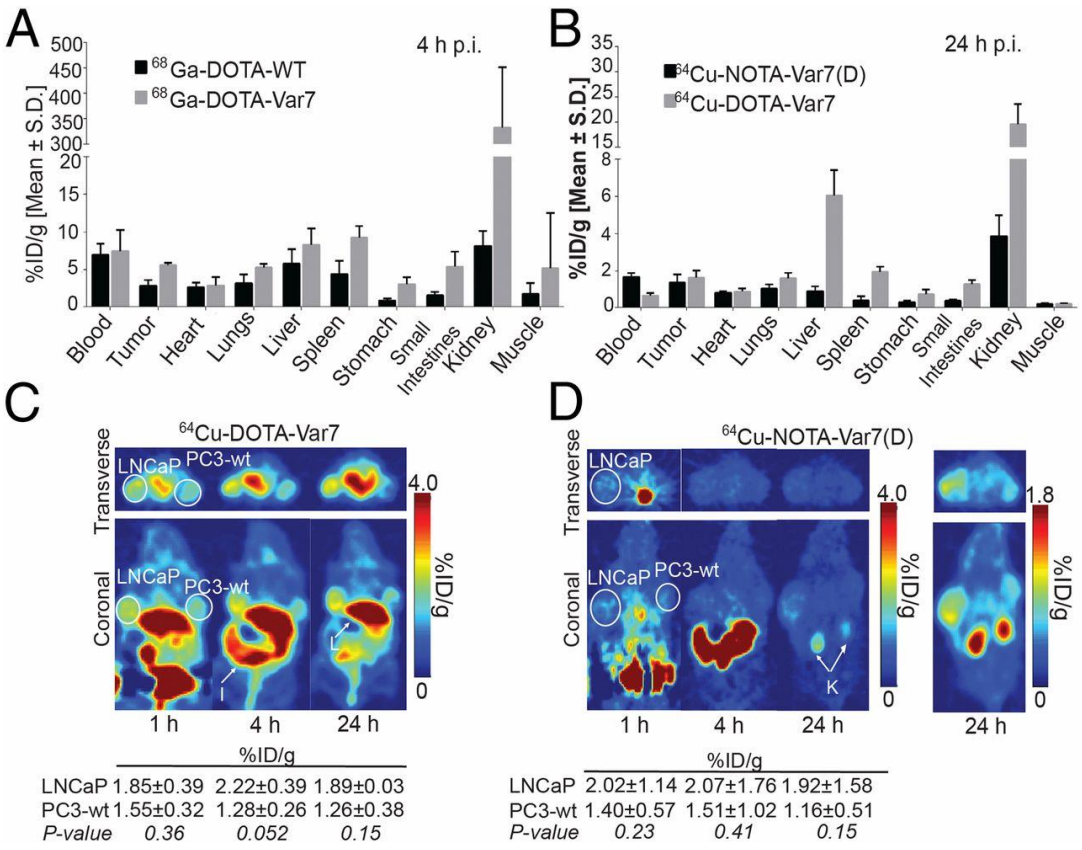

Figure 2. ***In vivo*** **pharmacokinetic optimization studies in prostate tumor xenografts.** Tissue distribution analysis of ^{68}Ga-DOTA-labeled WT and Var7 demonstrate superiority of the latter in terms of tumor uptake at 4 h p.i. in PC3-wt tumor implants (**A**); in the same tumor model, the distribution of ^{64}Cu-NOTA-Var7(D) displays faster clearance and less non-specific binding of the NOTA scaffold, particularly in hepatobiliary (L=liver), intestinal (I=intestines) and renal (K=kidneys) tissues, in contrast to ^{64}Cu-DOTA-Var7. However, tumor uptake of both probes was comparable at 24 h p.i. (**B**); acquired PET images (**C, D**) from 1-24 h were consistent with the biodistribution data (**A, B**) for both LNCaP and PC3-wt xenografts. The PET images clearly demonstrate the advantages of ^{64}Cu-NOTA-Var7(D) compared to ^{64}Cu-DOTA-Var7, due to more rapid clearance from hepatobiliary and intestinal tissues.

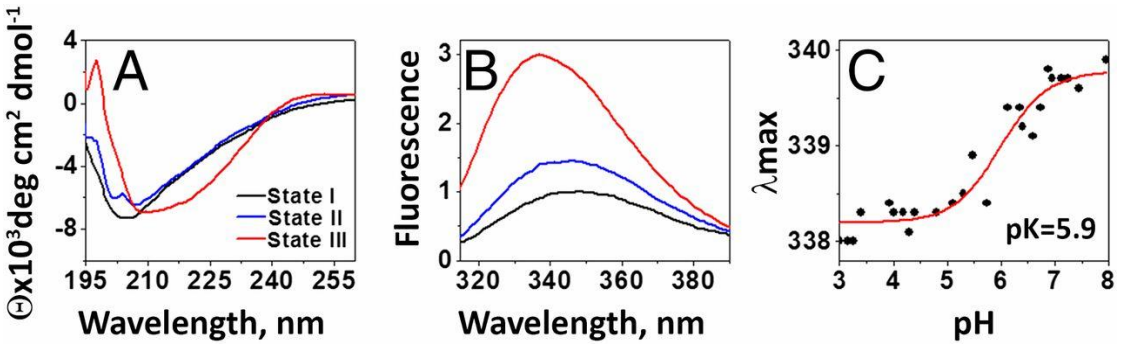

Figure 3. pH-dependent interaction of Cu-NOTA-Var7(D) with the lipid membrane bilayer. Cold Cu-NOTA-Var7(D) was studied for the presence of the three basic states of pHLIP; state I is the peptide in solution at pH 8; state II is the peptide in the presence of POPC liposomes at pH 8; state III is the folding and insertion of the peptide with POPC liposomes from pH 8 to 3.6. The states were monitored by changes of the steady-state circular dichroism (the spectra D-version of the peptide were multiplied by -1) (**A**) and tryptophan fluorescence spectroscopy at λ_{ex} = 295 nm (**B**). Changes in the intrinsic fluorescence of the construct were monitored as a function of pH as a result of the peptide's insertion wherein a pKa ~ 5.9 was obtained (**C**). The values obtained from the results of analyzed spectral data are given in SI Table 5.

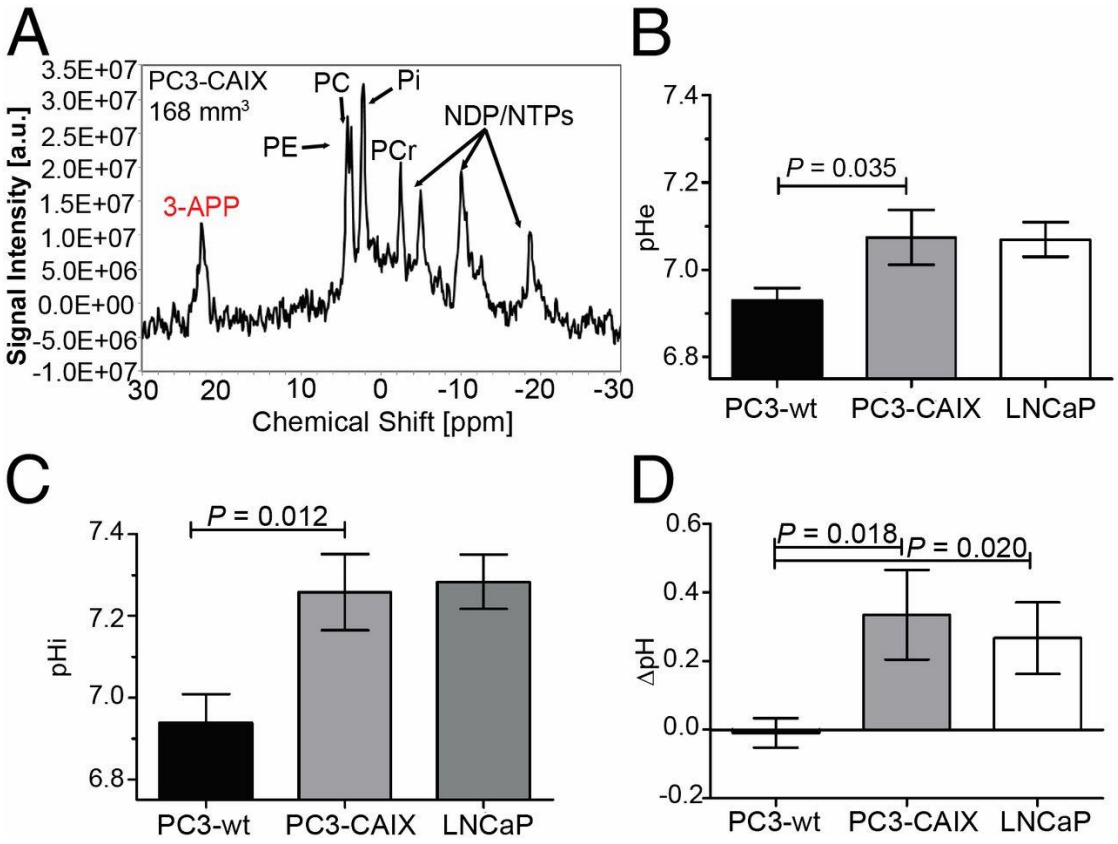

Figure 4. *In vivo* pHe measurements. Representative ^{1}H-decoupled ^{31}P MR spectrum of a PC3-CAIX tumor after 3-APP injection. Signal assignments are: 3-aminopropylphosphonate (3-APP), phosphoethanolamine (PE), phosphocholine (PC), inorganic phosphate (Pi), phosphocreatine (PCr), nucleoside di- and triphosphates (NDP/NTPs) (**A**); pHe measurements among three prostate tumor models show PC3-wt as the most acidic (6.93 ± 0.03, P = 0.035) compared to the PC3-CAIX (7.07 ± 0.06) and LNCaP (7.07 ± 0.04) xenografts (**B**); The intracellular acidity of PC3-wt (6.94 ± 0.07, P = 0.012) is higher than the other prostate implants (**C**); positive proton fluxes, corresponding to a respective extracellular to intracellular pH gradient, are observed for PC3-CAIX (0.33 ± 0.13, n=5, P = 0.018) and LNCaP (0.27 ± 0.10, n=5, P = 0.020) tumors, but not for PC3-wt tumors (-0.010 ± 0.055, n=5) (**D**).

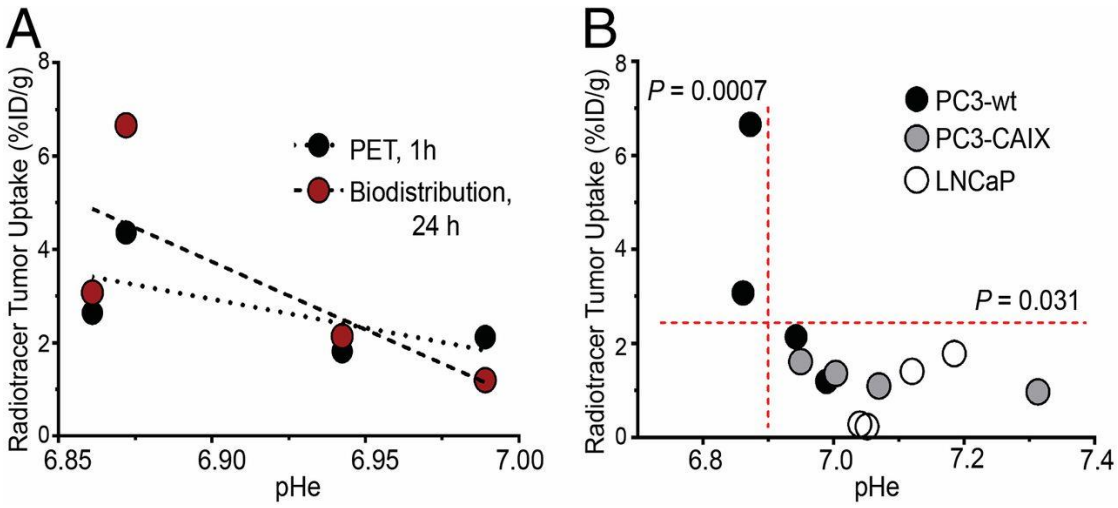

Figure 5. Tumor uptake of pHLIP-PET shows a direct association with extracellular acidity. An increasing trend of ^{64}Cu-NOTA-Var7(D) uptake was displayed as the pHe of the PC3-wt tumor model decreases (**A**); A plot of the pHe against tumor uptake (%ID/g, 24 h p.i.) of the radiotracer for data pooled from all three tumor models demonstrate a notable threshold where higher probe accretion (>3%ID/g) correlates to a very acidic extracellular space with pHe < 6.9 (**B**).

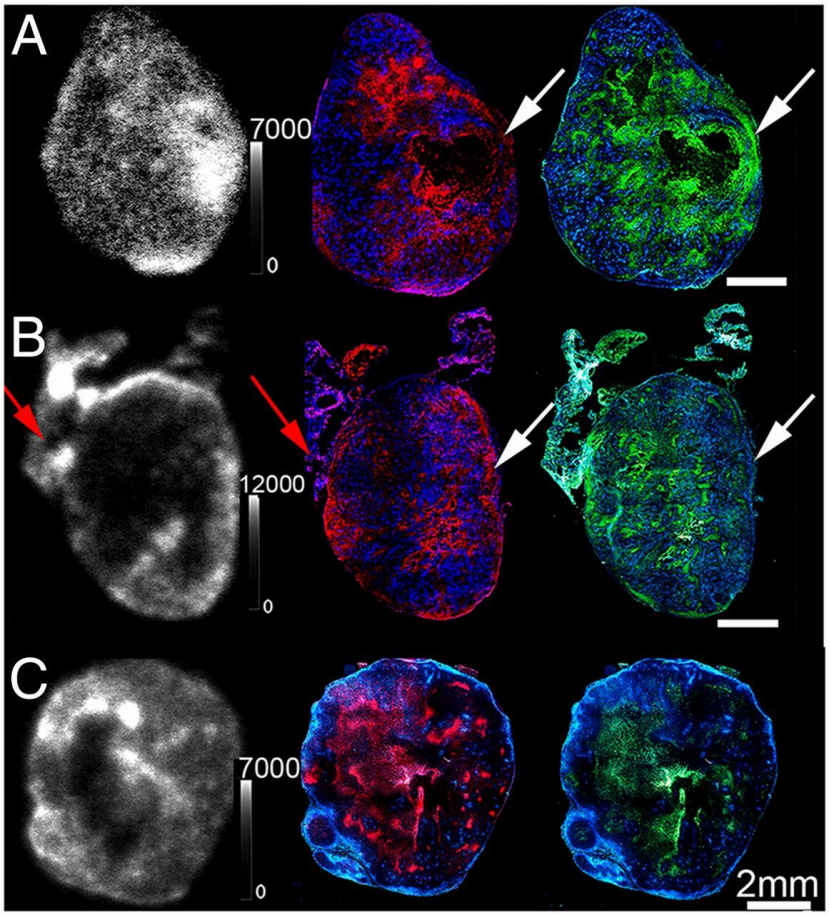

Figure 6. Histology and autoradiography. ^{64}Cu-NOTA-Var7(D) autoradiography (24 h p.i.) and correlative histology from 10 μm adjacent sections obtained from representative PC3-CAIX (**A**), LNCaP (**B**), and PC3-WT (**C**) tumors. The distributions of ^{64}Cu-NOTA-Var7(D) (white), pimonidazole (hypoxia, green) Hoechst 33342 (perfusion, blue), and expression of LDH-A (red) are shown (Bar = 2 mm). White arrows indicate examples of discordance between pimonidazole uptake and LDH-A expression. Red arrows indicate accumulation of ^{64}Cu-NOTA-Var7(D) on the skin. Re-binned pixel-by-pixel scatterplots, derived from the PC3-CAIX, LNCaP and PC3-wt sections shown in **A-C** respectively, show the relationship between autoradiographic counts and the staining intensity of the markers pimonidazole, LDH-A and Hoechst 33342 (**D-F)**.

Supplementary Information

Materials and Methods

All chemicals were obtained from Sigma Aldrich (St. Louis, MO), unless stated otherwise. Removal of trace metals from ultrapure water (>18.2 MΩ·cm at 25 ºC, Milli-Q, Millipore, Billerica, MA) was performed by soaking overnight in Chelex 100 resin (Bio-Rad Laboratories, Hercules, CA) at a ratio of 5 g per 100 ml. Radioactivity doses were measured with a Capintec CRC-55tR Dose Calibrator (Capintec, Ramsey, NJ). Samples with radioactivity were scanned on a calibrated Perkin Elmer (Waltham, MA) Automatic Wizard^2 gamma counter which was set to decay correct at the start of the assay. ^{68}Ga/^{64}Cu-radiolabeling reactions were monitored by using silica-gel impregnated glass-fiber instant thin-layer chromatography (ITLC-SG) paper (Pall Corp., East Hills, NY) and analyzed on a radio-ITLC plate reader (Bioscan System 200 Imaging Scanner) coupled to a Bioscan Autochanger 1000 (Bioscan Inc., Washington, DC), using Win-Scan Radio-TLC software v3.0.

Liposome preparation. Large unilamellar vesicles (LUVs) were prepared by extrusion: 1-palmitoyl-2-oleoyl-sn-glycero-3-phosphocholine (POPC, Avanti Polar Lipids, Inc.) dissolved in chloroform was de-solvated on a rotary evaporator and dried under vacuum for several hours. The phospholipid film was then rehydrated in 10 mM phosphate buffer pH 8.0, vortexed until the lipid layer was completely dissolved in buffer, and repeatedly extruded through membranes with 50 nm pore sizes to obtain LUVs.

Analytical ultra-centrifugation measurements. Sedimentation velocity measurements were carried out on a Beckman XL-I ultra-centrifuge with a Beckman

XL-A absorbance meter under temperature control. The states of Cu-NOTA-pHLIP constructs at 8 μM in 10 mM phosphate buffer (pH 8) were investigated. Loaded sample cells were placed inside the centrifuge for at least 3 hours before starting the experiment to allow the temperature to be equilibrated to 20 ^{o}C and the vacuum to reach 50 μm Hg. Measurements were made at 42K RPM following the peptide by absorbance at 280 nm for each cell every minute for approximately 20 hours. This resulted in acquiring at least 200 data points for each set of sample. The resulting data were then analyzed using SEDFIT software (NIH, Bethesda, MD). The buffer viscosity and density values were calculated with SEDNTERP (Biomolecular Interaction Technologies Center at the University of New Hampshire), and were set as 0.01005 and 0.99967 respectively. Values for the partial specific volume and F-ratio were 0.73 and 0.95, respectively. The distribution of sedimentation coefficients obtained for each construct was analyzed using Gaussian fitting functions.

Generation of SFG-CAIX-IRES2-GFP vector. All DNA manipulations were performed using restriction enzymes, T4 DNA ligase, and buffers according to standard procedures and manufacturer's instructions (New England BioLabs, CA, USA). The retroviral vector SFG-FLuc-IRES2-GFP (1) was used to generate a new retroviral vector SFG-CAIX-IRES2-GFP. To construct the SFG-CAIX-IRES2-GFP vector, the gene of full length CAIX cDNA was amplified from pCMV6-ENTRY plasmid with human CAIX (carbonic anhydrase IX) cDNA (NM_001216) linked with two tags Myc-DKK (# RC204839, OriGene Tech, MD, USA). Amplification of the *CAIX* gene was performed by PCR using one primer for the 5' end of cDNA that incorporated the *Sgf*I restriction site 5'- GCGATCGCCATGGCTCCCCTGTGCC-3'

and a 2nd primer 5'-GGAAGATCTTTAAACCTTATCGT-3', bearing the *Bgl*II restriction site. The resulting PCR product was used for *Sgf*I/*Bgl*I ligation into the SFG-FLuc-IRES2-GFP backbone to obtain the final plasmid SFG-CAIX-IRES2-GFP where the *CAIX* gene was separated from the *GFP* by an IRES element. SFG-CAIX-IRES2-GFP retroviral plasmid was transfected into a GPG293 producer cell line using LipofectAMINE 2000 (Invitrogen, CA), as described previously (2). The retrovirus-containing medium was collected over four consecutive days and stored at -80°C.

Western blotting. Cell preparations were extracted using Mammalian Protein Extraction Reagent (Pierce, Rockford, IL, USA). Protein concentrations were determined by Bio-Rad protein assay (Bio-Rad, Hercules, CA, USA). The proteins in equivalent amounts (10-40 µg/well) were separated by electrophoresis in a NuPAGE gradient 4-12% *bis*-Tris Gel (Invitrogen, Carlsbad, CA, USA) and were immuno-blotted with anti-CAIX antibody (Epitomics Inc., CA, USA) at a 1:1000 dilution, anti-DKK and anti-Myc antibodies (OriGene Tech, MD, USA) at 1:1000 dilution, and anti-ß-actin antibodies (Abcam Inc., Cambridge, MA, USA) at a 1:5000 dilution. Immune complexes were detected by horseradish-peroxidase labeled antibodies and enhanced chemiluminescence reagent (Amersham, Buckinghamshire, UK).

MRS

The MR experiments were performed on mice using a horizontal-bore 7T MR spectrometer (Bruker, Germany), employing a home-built ^{1}H / ^{31}P MR coil assembly. Prior to the MR measurements, a tail vein catheter was inserted, facilitating the administration of 3-APP via a home-built catheter line assembly during the MR experiment. For the duration of the MR experiment, the mice were kept anesthetized

with < 2% isoflurane in 100% oxygen and the core temperature was maintained at 34-37°C. The breathing rate, monitored using a pressure sensor, was kept at 50-80 breath/min by adjusting the isoflurane level. The rodent core temperature was maintained at 34-37°C using an MR-compatible, small rodent Heater System. After tuning and matching of the ^{1}H and ^{31}P MR coils, the water line width across the tumor was optimized to 35-80 Hz full-width-half-maximum using field map-based shimming. Two baseline ^{1}H-decoupled ^{31}P MR single pulse spectra, averaged over 17 min 4 s, each were acquired using a 60° excitation pulse, 2 s relaxation delay, 10 kHz spectral width, 2048 points, and 512 averages. Following these, a bolus of 480 mg/kg 3-APP was injected i.v. via the tail vein catheter directly before the acquisition of another ^{1}H-decoupled ^{31}P MR spectrum; directly following the first post-APP acquisition, a 2nd bolus of 480 mg/kg 3-APP was injected *i.v.* and a 2nd ^{1}H-decoupled ^{31}P MR spectrum acquired. For each tumor, the free induction decays (FIDs) of the two ^{31}P MR spectra, before and after 3-APP injection respectively, were added up, resulting in a 34 min 8 s MR spectrum for each, and an exponential line broadening of 20 Hz applied. The resulting FIDs were Fourier transformed, phase corrected, and the α-NDP/α-NTP signal calibrated to -10.05 ppm (**Fig. 4A**). The MR spectra were fitted in the time domain, using the software package XsOsNMR (kindly provided by Dr. Dikoma Shungu and Xiaoling Mao) and the intracellular and extracellular pH (pHi, pHe) calculated from the chemical shifts of inorganic phosphate (Pi) and 3-aminopropylphosphonate (3-APP) respectively, as described in detail previously (3). As the inorganic phosphate signal in tumors is predominantly comprised of intracellular Pi, due to the densely-packed cells, the pH calculated from its chemical

shift represents primarily intracellular pH (pHi) (4, 5). The chemical shifts δ of Pi and 3-APP relative to α-NTP at -10.05 ppm, δ(Pi) and δ(3-APP) respectively, are related to pHi and pHe by their respective Henderson-Hasselbalch equations and calculated as follows:

$$\mathrm{pHi} = 6.85 + \log_{10}\frac{\delta(\mathrm{Pi}) - 0.58}{3.14 - \delta(\mathrm{Pi})}$$

$$\mathrm{pHe} = 6.91 + \log_{10}\frac{\delta(\text{3-APP}) - 21.10}{24.32 - \delta(\text{3-APP})}$$

pH values were reported as the mean ± standard error of the mean (SEM).

Supplementary Tables

SI Table 1. Tissue uptake (mean %ID/g ± S.D.) of ^{68}Ga-DOTA-WT administered via lateral tail vein in male, athymic nu/nu mice bearing PC3-wt prostate cancer xenografts.

Tissue	1 h n=4			2 h n=4			4 h n=4		
Blood	13.78	±	2.56	10.55	±	2.07	6.94	±	1.51
PC3 tumor	1.87	±	0.45	2.36	±	0.40	2.86	±	0.75
Heart	3.99	±	1.28	3.26	±	0.73	2.63	±	0.62
Lungs	6.67	±	1.60	4.83	±	0.26	3.17	±	1.16
Liver	7.21	±	2.43	5.22	±	0.68	5.79	±	1.91
Spleen	2.87	±	0.53	2.28	±	1.26	4.36	±	1.78
Stomach	0.60	±	0.20	0.66	±	0.24	0.80	±	0.31
Small intestines	1.29	±	0.55	1.36	±	0.13	1.50	±	0.46
Large intestines	0.37	±	0.09	0.29	±	0.08	0.66	±	0.31
Kidney	6.38	±	2.39	7.60	±	2.00	8.15	±	1.98
Muscle	0.76	±	0.33	0.67	±	0.29	1.67	±	1.55
Bone	2.09	±	0.97	4.67	±	3.37	5.31	±	4.49
Brain	0.34	±	0.17	0.30	±	0.12	0.55	±	0.11
Contrast calculated as Tumor to Organ Ratio [rel. u.]									
Tumor/Blood	*0.12*	±	*0.02*	*0.23*	±	*0.02*	*0.43*	±	*0.16*
Tumor/Liver	*0.27*	±	*0.02*	*0.45*	±	*0.03*	*0.40*	±	*0.05*
Tumor/Kidney	*0.30*	±	*0.05*	*0.32*	±	*0.05*	*0.37*	±	*0.16*
Tumor/Muscle	*2.14*	±	*0.40*	*3.92*	±	*1.26*	*2.02*	±	*1.97*
Tumor/Bone	*1.09*	±	*0.67*	*0.80*	±	*0.63*	*0.25*	±	*0.13*

SI Table 2. Tissue uptake (mean %ID/g ± S.D.) of ^{68}Ga-DOTA-Var7 administered via lateral tail vein in male, athymic nu/nu mice bearing PC3-wt prostate cancer xenografts.

Tissue	1 h n=4			2 h n=5			4 h n=4		
Blood	4.54	±	0.69	6.49	±	1.62	7.46	±	2.80
PC3 tumor	2.47	±	0.19	4.37	±	1.46	5.60	±	0.30
Heart	2.15	±	0.38	3.13	±	0.36	2.89	±	1.10
Lungs	4.18	±	0.67	5.07	±	0.86	5.26	±	0.52
Liver	4.01	±	0.37	4.39	±	0.53	8.30	±	2.14
Spleen	4.12	±	0.68	5.29	±	0.30	9.26	±	1.52
Stomach	1.46	±	0.33	2.35	±	0.57	3.05	±	0.94
Small intestines	2.53	±	0.29	2.86	±	0.17	5.38	±	2.02
Large intestines	1.21	±	0.17	1.56	±	0.45	7.73	±	1.06
Kidney	103.54	±	13.23	134.40	±	32.79	332.24	±	118.92
Muscle	1.00	±	0.16	2.03	±	0.46	5.16	±	7.34
Bone	6.62	±	1.87	14.39	±	1.95	13.33	±	9.87
Brain	0.52	±	0.11	0.79	±	0.16	0.55	±	0.32
Contrast calculated as Tumor to Organ Ratio [rel. u.]									
Tumor/Blood	*0.55*	±	*0.05*	*0.72*	±	*0.30*	*0.69*	±	*0.18*
Tumor/Liver	*0.62*	±	*0.04*	*0.87*	±	*0.47*	*0.61*	±	*0.15*
Tumor/Kidney	*0.020*	±	*0.002*	*0.03*	±	*0.01*	*0.020*	±	*0.006*
Tumor/Muscle	*2.51*	±	*0.25*	*2.28*	±	*0.75*	*3.17*	±	*0.91*
Tumor/Bone	*0.39*	±	*0.09*	*0.39*	±	*0.14*	*0.57*	±	*0.41*

SI Table 3. Tissue uptake (mean %ID/g ± S.D.) of ^{64}Cu-DOTA-Var7 administered via lateral tail vein in male, athymic nu/nu mice bearing PC3-wt prostate cancer xenografts.

Tissue	1 h n=5			4 h n=5			24 h n=5		
Blood	1.89	±	0.70	0.68	±	0.05	0.63	±	0.13
PC3 tumor	1.19	±	0.55	1.45	±	0.19	1.64	±	0.38
Heart	0.95	±	0.28	0.71	±	0.08	0.86	±	0.17
Lungs	1.33	±	0.35	1.16	±	0.34	1.61	±	0.28
Liver	5.03	±	1.33	4.83	±	0.90	6.05	±	1.36
Spleen	1.08	±	0.59	1.05	±	0.36	1.95	±	0.27
Stomach	0.67	±	0.34	0.95	±	0.45	0.72	±	0.26
Small intestines	1.72	±	0.82	1.46	±	0.14	1.29	±	0.20
Large intestines	0.56	±	0.21	2.17	±	0.70	2.38	±	0.69
Kidney	27.98	±	8.62	32.24	±	7.90	19.59	±	3.99
Muscle	0.26	±	0.05	0.15	±	0.02	0.21	±	0.02
Bone	0.88	±	0.38	1.02	±	0.50	0.87	±	0.23
Brain	0.07	±	0.03	0.11	±	0.04	0.10	±	0.05
Contrast calculated as Tumor to Organ Ratio [rel. u.]									
Tumor/Blood	*0.63*	±	*0.16*	*2.15*	±	*0.27*	*2.63*	±	*0.57*
Tumor/Liver	*0.24*	±	*0.08*	*0.31*	±	*0.04*	*0.28*	±	*0.08*
Tumor/Kidney	*0.05*	±	*0.02*	*0.05*	±	*0.01*	*0.08*	±	*0.01*
Tumor/Muscle	*4.59*	±	*1.58*	*10.24*	±	*2.46*	*7.81*	±	*1.78*
Tumor/Bone	*1.44*	±	*0.59*	*1.18*	±	*0.19*	*1.94*	±	*0.41*

SI Table 4. Tissue uptake (mean %ID/g ± S.D.) of ^{64}Cu-NOTA-Var7(D) administered via lateral tail vein in male, athymic nu/nu mice bearing PC3-wt prostate cancer xenografts.

Tissue	1 h n=5			4 h n=5			24 h n=5		
Blood	2.81	±	0.76	2.14	±	0.76	1.67	±	0.21
PC3 tumor	1.62	±	0.24	1.07	±	0.33	1.36	±	0.43
Heart	0.95	±	0.13	0.84	±	0.31	0.79	±	0.10
Lungs	2.55	±	0.51	1.33	±	0.75	1.02	±	0.25
Liver	2.25	±	0.67	2.07	±	0.89	0.88	±	0.26
Spleen	0.75	±	0.11	0.41	±	0.14	0.38	±	0.23
Stomach	0.52	±	0.27	0.69	±	0.44	0.28	±	0.09
Small intestines	22.78	±	16.42	1.16	±	0.30	0.37	±	0.06
Large intestines	15.37	±	5.76	27.64	±	3.50	0.53	±	0.11
Kidney	13.27	±	0.65	5.84	±	0.89	3.86	±	1.14
Bone	0.55	±	0.18	0.20	±	0.09	0.20	±	0.04
Muscle	0.72	±	0.55	0.34	±	0.27	0.27	±	0.17
Contrast calculated as Tumor to Organ Ratio [rel. u.]									
Tumor/Blood	*0.60*	±	*0.09*	*0.43*	±	*0.17*	*0.81*	±	*0.22*
Tumor/Liver	*0.75*	±	*0.15*	*0.46*	±	*0.20*	*1.56*	±	*0.40*
Tumor/Kidney	*0.11*	±	*0.01*	*0.13*	±	*0.04*	*0.39*	±	*0.17*
Tumor/Muscle	*3.13*	±	*0.79*	*4.25*	±	*0.64*	*7.81*	±	*0.88*
Tumor/Bone	*3.05*	±	*1.41*	*0.36*	±	*2.99*	*6.04*	±	*2.34*
Tumor/Sm. Intestines	*0.14*	±	*0.15*	*0.94*	±	*0.69*	*3.71*	±	*1.04*

SI Table 5. The apparent pK (pKa) of pHLIP peptide insertion into membrane, the sedimentation coefficients (Sed. Coeff.) and calculated molecular masses of the peptides in solution at pH 8.0, and the spectral parameters of peptides in the states I, II and III are presented. The spectral parameters were obtained from the analysis of the fluorescence and CD spectra: the maximum position of the fluorescence spectrum λ_m, *S* – the normalized area under the spectra (normalized with respect to the area under the spectrum of pHLIP in state I); θ_{225} x 10^3, deg cm^2 $dmol^{-1}$ – the molar ellipticity at 225 nm.

	pKa	**Sed. Coef. / Mass / Mol. weight (kDa)**	**State I**	**State II** λ_m / *S* / θ_{225} x10^3	**State III**
Var7	5.9	1.04/7.03/3.58	348 /1.0/-3.18	345/1.39/-3.05	337/2.62/-5.03
Var5	5.5	1.16/7.31/3.73	352/1.0/-2.44	347/1.64/-2.88	339/1.79/-7.16
WT	--*	1.52/14.30/4.68	340/1.0/-6.80	340/1.21/-6.19	340/3.38/-7.23

* The pKa was not calculated for WT, since there is no shift of the position of maximum of fluorescence spectra between states I, II and III.

SI Table 6. Table detailing the values obtained from the independent *in vivo* MR, *in vivo* PET, and *ex vivo* experiments performed and the corresponding pairing as used in the figures. Tumors used for autoradiography and immunohistochemistry (green highlight) were not used for biodistribution studies. Abbreviations: BL pHi – intracellular pH before 3-APP injection, pHi – intracellular pH after 3-APP injection, pHe – extracellular pH determined from 3-APP signal, ΔpHi = BL pHi-pHi, ΔpH = pHi-pHe, T – tumor, T/M – tumor to muscle ratio. Data in red depict experiments with missing values, and were not included in the analyses.

Tumor		***In Vivo* MRS**					***In Vivo* PET**			***Ex Vivo* Biodistribution**	
Type	**Size**	**BL pHi**	**pHi**	**pHe**	**ΔpHi**	**ΔpH**	**1 h**	**4 h**	**24 h**	**T**	**T/M**
PC-3 wt - RS	248	7.12	7.11	6.99	0.00	0.12	2.12	1.99	1.61	1.20	5.29
	185						*1.26*	*1.54*	*1.58*	*1.25*	*2.49*
	104	7.02	6.92	6.94	0.09	-0.02	1.82	1.67	1.39	2.14	7.90
	254	6.78	6.85	6.83	-0.07	0.02	0.86	0.85	0.79	0.84	7.02
	95	7.299									
PC-3-CA-IX - RS	189	7.25	7.12	7.01	0.13	0.11					
	209	7.47	7.35	7.00	0.12	0.35	3.26	2.02	1.56	1.37	5.64
	151	7.29	7.78	6.95	-0.49	0.83	2.77	2.09	1.72	1.62	8.22
	169	*7.35*	*7.44*		-0.08		*0.80*	*0.89*	*0.80*	*0.90*	*3.71*
	168	*7.12*	*7.12*	*7.04*	0.00	0.08	2.19	2.27	2.09	*IHC*	*IHC*
	156	7.02	7.23	7.07	-0.21	0.16	1.75	1.78	1.30	1.10	6.90
	271	7.03	6.95	7.31	0.08	-0.36	1.73	1.65	1.30	0.97	6.01
	161	6.96	7.07	6.84	-0.10	0.22	0.72	0.80	0.85	0.89	5.41
	157	6.72	6.72	6.86	0.00	0.00	2.64	2.40	1.27	3.08	12.52
	160	6.89	6.85	6.87	0.04	-0.02	4.36	2.13	5.06	6.66	12.73
LNCaP - RS	287	7.15	7.23	7.18	-0.08	0.05	4.43	6.19	5.14	1.79	2.70
	344	7.32	7.40	7.12	-0.09	0.28	2.27	2.40	2.42	1.41	9.74
	314	7.43	7.26		0.18						
	338	*7.08*	*7.05*		0.03		*1.94*	*2.40*	*2.27*	*1.92*	*16.24*
	128	*7.30*	*7.60*	*6.95*	-0.30	0.65	3.10	3.72	2.74	*IHC*	*IHC*
	113	7.34	7.27	7.04	0.07	0.23	1.84	0.66	0.45	0.29	0.10
	167	7.24	7.17	7.05	0.07	0.12	1.63	1.06	0.81	0.23	0.03

Supplementary Figures

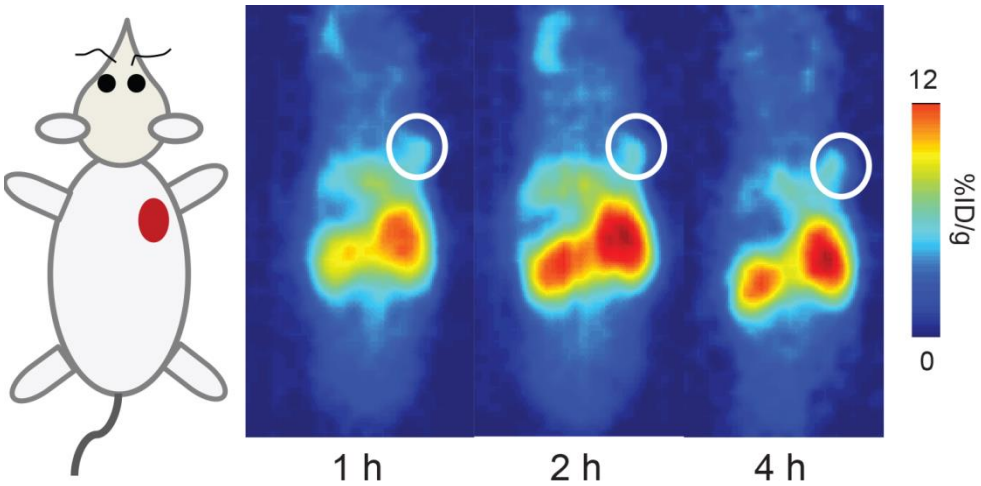

SI Fig. 1 Serial PET images of a representative PC3-wt prostate tumor obtained after 1 h, 2 h and 4 h post injection of ^{68}Ga-DOTA-WT, demonstrating non-specific binding of the pHLIP variant to healthy tissue (e.g. liver, kidney). The white circle delineates the subcutaneous shoulder tumor.

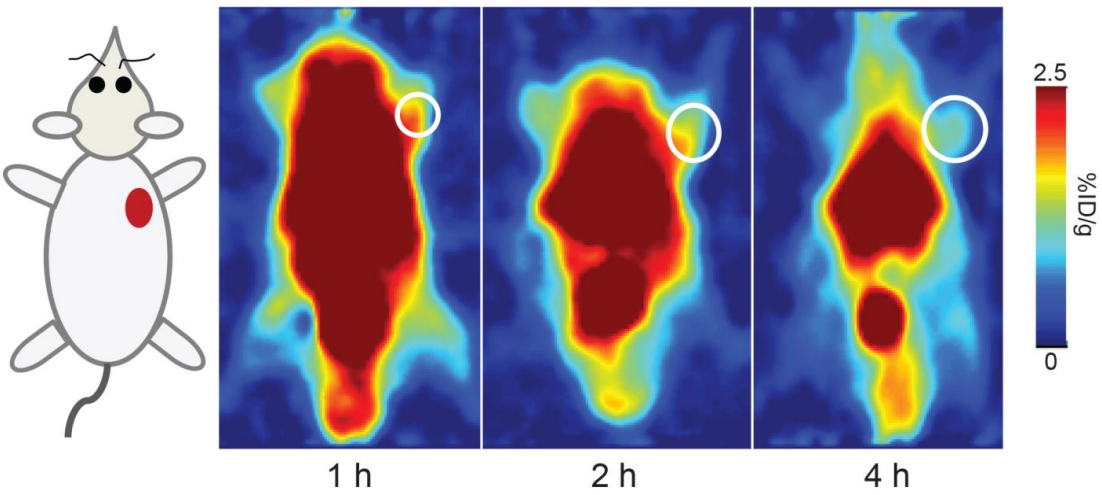

SI Fig. 2 Serial PET images with ^{68}Ga-DOTA-Var7 in PC3-wt prostate models acquired after 1-4 h p.i., demonstrating poor tumor-to-background contrast**.** The white circle delineates the subcutaneous shoulder tumor.

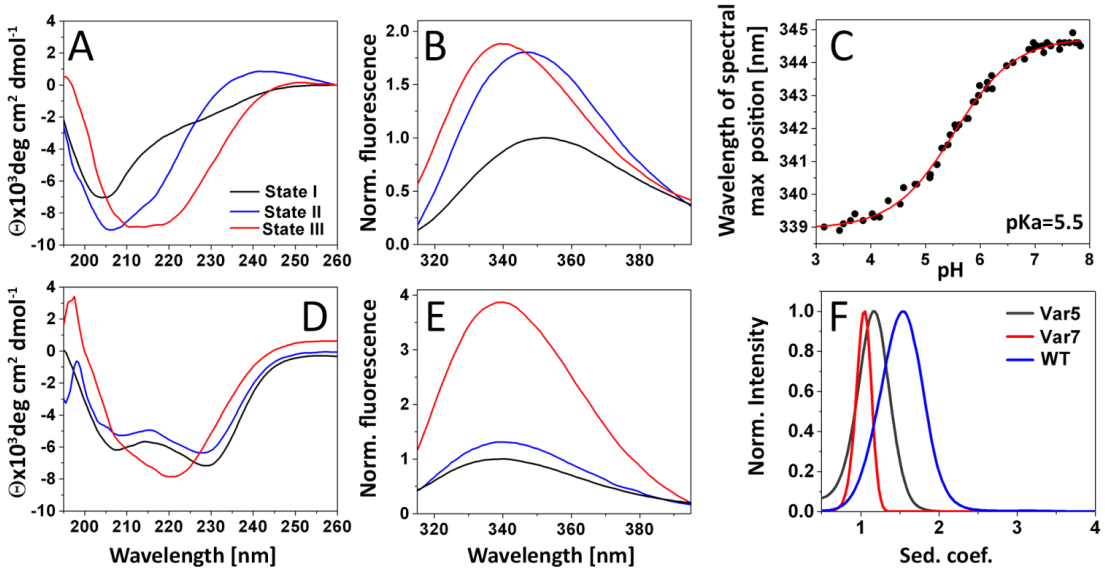

SI Fig. 3 pH-dependent interactions of Cu-NOTA-Var5 and Cu-NOTA-WT with a lipid membrane bilayer. The constructs were studied for the presence of the three basic states of pHLIP; state I is the peptide in solution at pH 8; state II is the peptide in the presence of POPC liposomes at pH 8; state III is the folding and insertion of the peptide with POPC liposomes from pH 8 to 3.6. The states were monitored by changes of the steady-state circular dichroism (**A, D**) and tryptophan fluorescence at λ_{ex} = 295 nm (**B, E**) spectroscopy for Cu-NOTA-Var5 (A, B) and Cu-NOTA-WT (D, E), respectively. Changes in the intrinsic fluorescence of the Cu-NOTA-Var5 were monitored as a function of pH as a result of the peptide's insertion wherein a pKa ~ 5.5 was obtained (**C**). The oligomeric states of Cu-NOTA-Var5 (Var5), Cu-NOTA-Var7(D) (Var7) and Cu-NOTA-WT (WT) were investigated by analytical ultracentrifugation, the obtained sedimentation coefficients for all constructs in buffer at pH 8 are shown in **F**. The spectral data were analyzed and resulting values are given in SI Table 5.

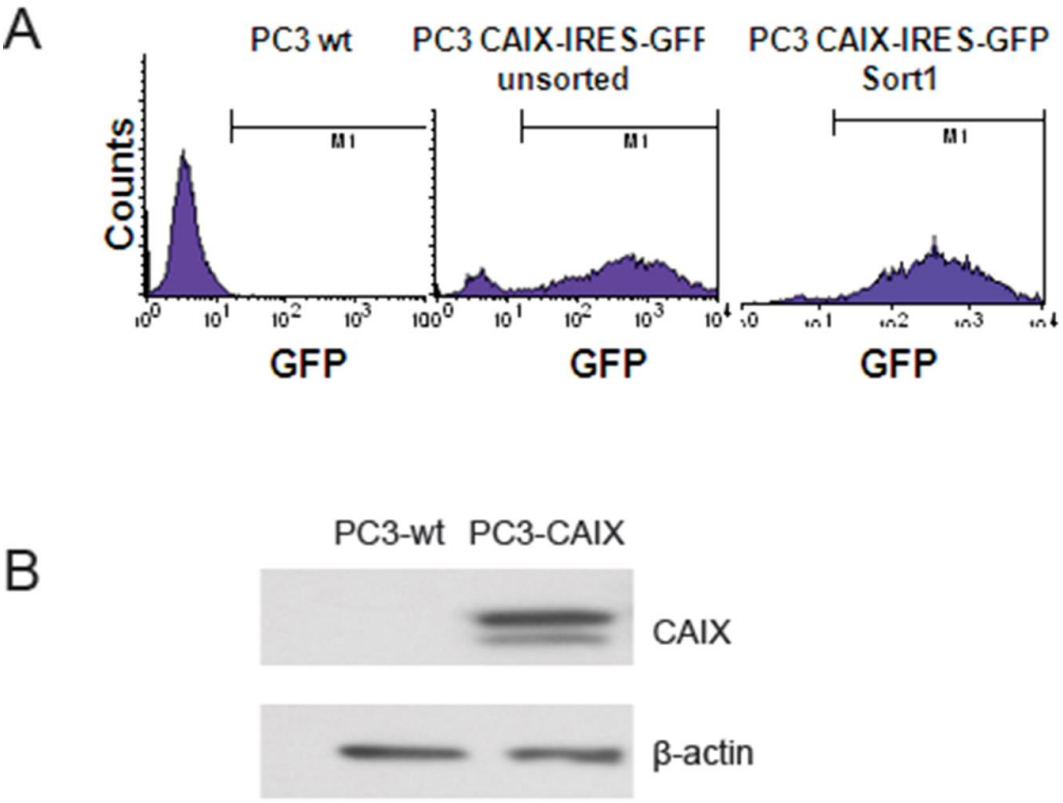

SI Fig. 4 CAIX transduction in PC3-wt cells. PC3-wt cells were transduced with the SFG-CAIX-IRES-GFP vector and sorted several times to select the populations of GFP-expressing cells **(A)**. Higher levels of CAIX expression in sorted cells (PC3-CAIX) than in PC3-wt cells was confirmed by Western blotting of PC3-wt and CAIX-transduced PC3 cells **(B)**.

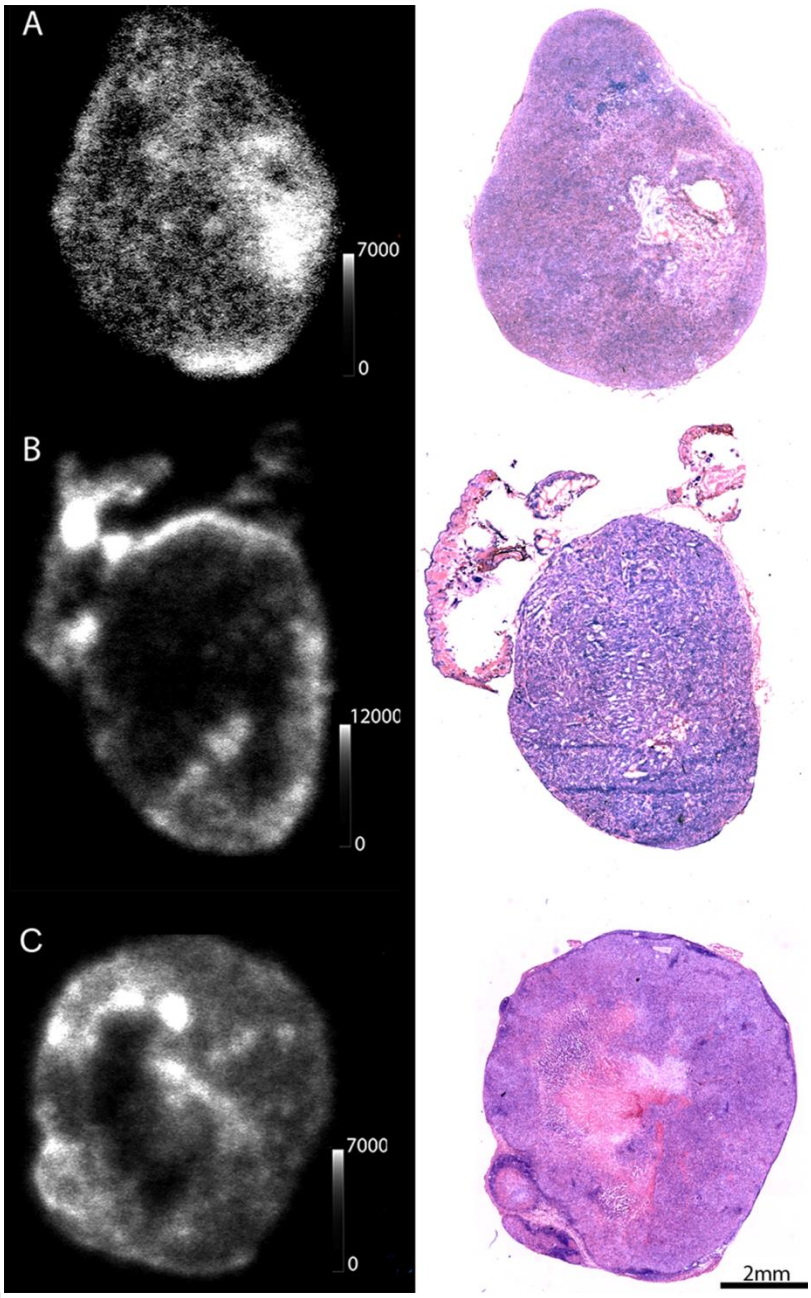

SI Fig. 5 ^{64}Cu-NOTA-Var7(D) autoradiography (24 h p.i.) and correlative histology from 10 µm adjacent sections obtained from representative PC3-CAIX (**A**), LNCaP (**B**), and PC3-WT (**C**) tumors. Comparison of ^{64}Cu-NOTA-Var7(D) distribution versus H&E staining of a sequential 10 µm section adjacent to the one used for autoradiographic evaluation. Areas containing skin and regions of tumor necrosis are clearly visible. Bar = 2 mm.

Reference:

1. Moroz E, *et al.* (2009) Real-time imaging of HIF-1alpha stabilization and degradation. *PLoS One* 4(4):e5077.
2. Helmlinger G, Yuan F, Dellian M, & Jain RK (1997) Interstitial pH and pO2 gradients in solid tumors *in vivo*: high-resolution measurements reveal a lack of correlation. *Nat Med* 3(2):177-182.
3. Raghunand N (2006) Tissue pH measurement by magnetic resonance spectroscopy and imaging. *Methods Mol Med* 124:347-364.
4. Soto GE, Zhu Z, Evelhoch JL, & Ackerman JJ (1996) Tumor ^{31}P NMR pH measurements *in vivo*: a comparison of inorganic phosphate and intracellular 2-deoxyglucose-6-phosphate as pHnmr indicators in murine radiation-induced fibrosarcoma-1. *Magn Reson Med* 36(5):698-704.
5. Prichard JW, Alger JR, Behar KL, Petroff OA, & Shulman RG (1983) Cerebral metabolic studies *in vivo* by ^{31}P NMR. *Proc Natl Acad Sci U S A* 80(9):2748-2751.

CHAPTER 3

In Preparation for Publication

Insertion of short peptide into lipid bilayer: negative hydrophobic mismatch

Dhammika Weerakkody[1], Alexander G. Karabadzhak[1,#], Michael Anderson[1], Fallon Laliberte[1], Oleg A. Andreev[1], Theyencheri Narayanan[2,*], Yana K. Reshetnyak[1,*]

[1]Department of Physics, University of Rhode Island, Kingston, RI 02881[#]Present address: Department of Molecular Biophysics and Biochemistry, Yale University, New Haven, CT 06520[2]ESRF, CS40220, 38043 Grenoble, France

***Corresponding authors:** Yana K. Reshetnyak (reshetnyak@uri.edu) and Theyencheri Narayanan (narayan@esrf.fr)

Keywords: fluorescence, FRET, dual quenching, SAXS, membrane thinning, lipid bilayer

Running title: Negative hydrophobic mismatch

Abstract

Small angle x-ray scattering studies showed membrane thinning by 18% induced by insertion of short-pHLIP (truncated version of pH Low Insertion Peptide) into bilayer. Thinning allows to reduce stress on membrane associated with negative hydrophobic mismatch. Also we observed 12% of membrane thinning when long-pHLIP partitions into outer leaflet of bilayer at high pH adopting coil conformations. The long-pHLIP at high pH creates an asymmetric inclusion in the bilayer, which results in increase of tension leading to the bilayer thinning. The tension and thinning is released when long-pHLIP inserts into bilayer as a transmembrane helix at low pH.

Introduction

Membrane-associated folding is accompanied by the insertion of a polypeptide into the heterogeneous environment of a lipid bilayer of membrane. The stability of folded structures in a membrane is determined by the match between the thickness of the bilayer and the hydrophobic length of the transmembrane (TM) segments (1-4). Hydrophobic mismatch results in significant energetic penalties, which can lead to structural perturbations in a polypeptide, alteration in a polypeptide's mobility and/or membrane thickness changes (5-7).

Here we have performed a comparative investigation of long and short pHLIPs (pH Low Insertion Peptides) interactions with the lipid bilayer of a membrane. Long-pHLIPs are well investigated water-soluble membrane polypeptides, which insert into a lipid bilayer and form a stable TM alpha-helix as a result of a drop in pH (8-11). The insertion of the peptides of pHLIP family is employed for the targeting of acidic diseased tissue including tumors and intracellular delivery of polar cell-impermeable cargo molecules across membrane (*8, 12-15*).

Truncated versions of pHLIPs (short-pHLIP), if inserted into membrane, should create negative hydrophobic mismatch. We used several spectroscopic assays to prove that short-pHLIP's interaction with a lipid bilayer at low pH leads to the membrane inserted state of the peptide. Small angle x-ray scattering (SAXS) experiments performed on long and short peptides allowed us to demonstrate the thinning of a lipid bilayer of membrane as a result of short-pHLIP's insertion into the bilayer. The

experimental design was based on the comparison between interactions with membranes of well-characterized long-pHLIPs and truncated short-pHLIP.

Methods and Materials

The detailed information about all methods could be found in Supporting Information. All peptides were synthesized and purified at W.M. KECK Biotechnology center at Yale. The peptides were dissolved either directly in buffer or 3 M urea and then centrifuge to remove large aggregates or passed through G-10 column to remove urea, respectively. Concentrations of the peptides were calculated spectrophotometrically by measuring absorbance at 280 nm. Large unilamellar and multilamellar vesicles were prepared by extrusion. Lipids were dissolved in chloroform, desolvated in a rotary evaporator and dried under high vacuum followed by rehydration and extrusion.

Steady-state fluorescence and circular dichroism (CD) signals were measured for the peptides in absence and presence of POPC liposomes at pH 8.0 and 4.0. The quenching of tryptophan fluorescence of the peptides by acrylamide or 10-doxylnonadecane (10DN) was performed in the presence of POPC liposomes without and with 10% of the lipids replaced by 10DN at pH 8.0 and pH 4.0. Acrylamide was added to the samples containing POPC liposomes without 10DN. The peptide concentration in all samples was kept constant. Asymmetrically NBD-labeled POPC liposomes (labeled at inner leaflet) were incubated with the peptides and FRET from tryptophan residues to NBD at inner leaflet of the bilayer was monitored.

Synchrotron SAXS measurements were carried out at beamline ID02 of the ESRF in Grenoble, France (*16*). The measured two dimensional SAXS patterns were normalized to an absolute intensity scale using the standard procedure and azimuthally averaged to obtain the intensity profile as a function of *q*. The background buffer was also measured and subtracted from each averaged sample intensity profile before fitting the data.

Results

The main focus of our research is an investigation of interactions with lipid bilayer of membrane of short-pHLIP peptide, which is a truncated version of full-length pHLIPs (long-pHLIPs). Our experimental strategy is a comparison between membrane interactions of short-pHLIP and well-characterized long-pHLIPs.

Short-pHLIP: AEQNPIY**W**ARYADLLFPTTLA**W**

Long-pHLIP: AEQNPIY**W**ARYAD**W**LFTTPLLLLDLALLVDADET

Long-pHLIP*: AEDQNPY**W**RAYADLFTPLTLLDLLAL**W**DG

In the dual quenching and FRET spectroscopic assays we used long-pHLIP* peptide (with truncated flanking sequence), which has Trp residues located at the beginning and end of TM part, as in a short-pHLIP. We demonstrated previously truncated long pHLIP adopts TM helical orientation in membrane at low pH similar to a full-length long-pHLIP (11). We also attempted to investigate single-Trp mutants of short and long pHLIPs with the goal of simplifying the interpretation of spectroscopic data. However we found that some single-Trp mutants of short peptide did not exhibit pH-dependent properties and most probably do not insert into membrane (further

investigation is needed). Therefore, here we present results obtained with long and short pHLIPs containing both tryptophan residues.

Previously we demonstrated that long-pHLIPs insert into the lipid bilayer of membranes and form TM helices in a result of a drop in pH, and we used fluorescence and circular dichroism (CD) spectroscopic methods to monitor transitions (8-11). Here we show that short-pHLIP also exhibits very similar pH-dependent changes of CD signal, increase of tryptophan fluorescence and short wavelengths shift of the spectrum (Figure 1). Two negative peaks around 208-210 and 222-225 nm observed on CD spectra at low pH (Figure 1b, red line) are indicative of helical structure appearance. However, the overall strength of the CD signal was less than half compared to the signal of long pHLIPs (8), and the first minimum (at 208-210 nm) has higher amplitude compared to the second one at 222-225 nm. The CD signal could be attributed to the presence of a mixture of α-helical structures and random coil conformations or formation of a 3_{10} helix. Usually, the overall strength of the CD signal for 3_{10} helix is lower than for α-helix. Additionally its ratio of 222/208 nm < 1 (it is in the range of 0.3-0.4) compared to the same ratio for an α-helix (*17*).

To establish location of tryptophan residues (thus pHLIPs) within a lipid bilayer of membrane a dual quenching assay was employed (*18*). Effective quenching of Trp fluorescence by acrylamide occurs when tryptophan residues are exposed to polar parts of the outer or inner leaflets of a bilayer. At the same time tryptophan residues located in the middle of a membrane could be effectively quenched by another

quencher of tryptophan fluorescence, 10DN. We performed dual-quenching assay at pH 8.0 and pH 4.0 for short and long pHLIPs both containing Trp residues at the beginning and end of the expected TM region of the peptides (Figure 2). At pH 8.0 short-pHLIP just barely partitions into the bilayer and therefore tryptophan fluorescence is quenched by acrylamide very well (Figure 2a and Table 1). Long-pHLIP* being more hydrophobic, is located much deeper into the bilayer, which correlates well with our previous data (*11, 19*). Lowering the pH reduces quenching of Trp fluorescence by acrylamide (from 79.1 to 48.1% for short-pHLIP and from 44.1 to 31.1% for long-pHLIP) and increases quenching by 10DN (from 12.3 to 34.7% for short-pHLIP and from 32.7 to 44.6% for long-pHLIP) (see Figure 2 and Table 1). The overall trend of short-pHLIP's partition into bilayer at low pH is similar to long-pHLIP's. However, Trp residues in short-pHLIP are more exposed to acrylamide compared to Trp residues of long-pHLIP. According to our published data the truncated peptides have a lower affinity to the bilayer compared to long pHLIPs (8), thus higher amount of short-peptides could be found in solution, which will lead to the enhanced quenching by acrylamide.

The dual-quenching assay provides information about degree of partitioning of Trp residues into bilayer. However it does not allow distinguishing between the inner or outer leaflets location of acrylamide-accessible Trp residues. To further investigate location of tryptophan residues in membrane we also performed NBD-FRET assay (*20, 21*). First, symmetrically-labeled (with NBD dye) POPC liposomes were prepared. Then, membrane-impermeable dithionite was used to chemically modify and

quench the fluorescence of NBD in outer leaflet of the bilayer, followed by the removal of dithionite by gel filtration. As a result, asymmetrically-labeled liposomes with NBD at the inner leaflet were obtained. The absence of potential flip-flopping of lipids was accessed by absence of quenching of NBD fluorescence by addition of dithionite. FRET was monitored from the tryptophan residues of peptides to NBD. Energy transfer occurs when both fluorophores (Trp and NBD) are in a close proximity to each other (the Förster distance for Trp-NBD donor-acceptor pair is about 10 Å (*22*)). Thus, when tryptophan residues are located in the outer leaflet of the bilayer, there is no any significant energy transfer to NBD at the inner leaflet. This is the situation that was observed at pH 8.0 for both peptides, but was less pronounced for long-pHLIP, which partitions deeper into the membrane. At the same time, at low pH the FRET signal was comparable for both peptides (Figure 3b, d, red lines). We observed that the NBD fluorescence signal increased by 11.7 and 12.9 times for short-pHLIP and long-pHLIP, respectively, in the presence of POPC at low pH compared to the baseline. It indicates that Trp residues (located at the C-terminus) in long and short pHLIPs both are in close proximity to the headgroups of inner leaflet of bilayer. Thus, we can conclude that short-pHLIP inserts into lipid bilayer of membrane and spans bilayer similar to long-pHLIP.

When a short peptide is inserted into a membrane, as it is well known, a hydrophobic mismatch is created. We already mentioned about the possibility of presence of some elements of 3_{10} helical structures in short-pHLIP at low pH in membrane. 3_{10} is a stretched helix, where each residue increases the length of the helix by 2 Å in contrast

to 1.5 Å as in an α-helix. Thus, the presence of 3_{10} helical structures would help to reduce the mismatch. At the same time, the lipid bilayer might change thickness to match to the peptide length. To investigate potential changes, which might occur in the lipid bilayer when polypeptides interact with it, we carried out SAXS measurements on POPC liposomes in the absence and presence of long and short pHLIPs at high and low pHs. We used small (about 80 nm in diameter) and larger (about 120 nm in diameter) POPC liposomes. From the SAXS data, only the bilayer form factor was analyzed and the full vesicle scattering function was not included in the model.

The main features of the bilayer form factor of POPC liposomes in the presence of short-pHLIP at pH 8 (blue lines, Figure 4a, b) were very similar to that of original liposomes (black lines on Figure 4). At low pH, the maximum of the bilayer form factor of POPC liposomes in the presence of short-pHLIP (red lines Figure 4a, b) was shifted and became broader, indicating that the insertion of the peptide into the membrane caused a change in the bilayer structure. In contrast to the changes associated with short-pHLIP interaction with bilayer, the most significant changes of the bilayer form factor of liposomes was observed when long-pHLIP partitions into bilayer as an asymmetric inclusion at pH 8 (blue lines, Figure 4c, d). At low pH, when long-pHLIP inserts into membrane as a TM helix, the changes of the bilayer form factor was minimal compared to the form factor of liposomes in absence of the peptide.

Since, multilamelar features were observed for 120-nm liposomes (Figure 4b, d), only the data obtained with 80-nm liposomes was used for further analysis (fitting) to minimize the number of variable parameters. We employed a Gaussian model to describe electron density profiles [Eq. (1)]. The fitting was performed for the ED profiles obtained in different experiments with different concentrations of peptides and lipids. The representative fits are shown in Figure 5a-e. Table 2 summarizes the mean and standard deviation of the parameters calculated from the Gaussian fitting of SAXS data obtained in different experiments. The fitting of the data for short peptide in the presence of POPC at pH 8 proved to be the most problematic (the highest discrepancy between the fitting curves and experimental data). This is most likely due to the presence of free peptides, which was expected since truncated peptides have a lower binding affinity to the bilayer at pH 8 (8). The bilayer thickness for liposomes alone was set as 100%. The thinning of bilayer of liposomes calculated for different experiments were averaged and presented in Figure 5f. The electron density profile for POPC liposomes in the absence and presence of peptides are shown in Figure 5g, h. We observed an increase of electron density in the outer leaflet and in the middle of the bilayer and about 12% of bilayer thinning for POPC liposomes in the presence of long peptide at pH 8.0, when it partitions into the membrane in the form of random coil. At low pH, when long-pHLIP forms TM helix, the thinning is released. The short-peptide does not partition as deep into membrane as long-pHLIP and has a lower affinity to the bilayer at high pHs, thus the thinning is about twice less (7 %). The strongest thinning of the membrane by about 18% is observed in the case of short peptide insertion into bilayer at low pH. The significant membrane thinning at low pH

can indicate on insertion of short-pHLIP into bilayer. We can conclude that membrane thinning occurs to reduce a hydrophobic mismatch and an overall energy of the system.

Analysis of SAXS data

The scattered intensity can be expressed as $I(q) \propto \langle F(q)^2 \rangle$ (*23*), where $F(q)$ is the size averaged scattering form factor of vesicles, which is the Fourier transform of the bilayer electron density profile. By describing the electron density (ED) profile along the normal of the phospholipid bilayer of outer leaflet headgroups, hydrocarbon tails and inner leaflet headgroups as a sum of Gaussian functions (*23*-*27*):

$$\rho(z) = \sum_{k=1}^{n} \rho_k \cdot exp\left[-\frac{(z-z_k)^2}{2\sigma_k^2}\right] \quad (1)$$

we can obtain the following expression for the scattered intensity:

$$I(q) \propto \langle F(q)^2 \rangle = q^{-2} \sum_{k,k'} (R_0 + z_k)(R_0 + z_{k'})\rho_k \rho_{k'} \sigma_k \sigma_{k'} \cdot exp\left(\frac{-q^2\left(\sigma_k^2 + \sigma_{k'}^2\right)}{2}\right) \cos\left(q(z_k - z_{k'})\right) \quad (2)$$

where ρ_k, z_k and σ_k are the relative weight, position and width of the k-th Gauss function, respectively. For the bilayer $k = 1$ represents inner headgroups, $k = 2$ represents hydrocarbon tails, and $k = 3$ represents outer headgroups. We assume that

the center of the bilayer coincides with the center of the hydrocarbon tail, which means z_2 will be close to zero. The ED of liposomes in absence and presence of peptides was fitted by the sum of exponential functions. Fitting was performed using Origin 9.0. The best fit was defined as the one with the smallest χ^2.

Discussion

Previously we established that at the low lipid:peptide ratios we used in this study, the peptide is adsorbed to 50-60 lipids on average and an additional 50–60 lipids are perturbed. In contrast, a peptide in the transmembrane state III is estimated to affect only ~22 lipids, roughly one layer around the helix (10). Also we showed that long-pHLIP interacting with the biological membranes of human red blood cells (RBCs) at neutral pH induces appearance of spicules on the surface of the majority of cells (no leakage of hemoglobin by RBCs was observed) (*28*). The formation of spicules when the peptide is bound to the membrane was interpreted as the consequence of extra area occupied by pHLIP on the outer leaflet of the lipid bilayer. At pH 6, i.e., when a higher population of the peptides inserted into the membrane, the number of spikes is greatly reduced. A related observation was obtained from lipid fluidity measurements by the fluorescence anisotropy of TMA-DPH incorporated into the bilayer of membrane (*19*). The results of SAXS measurements indicate a 12% and 7% thinning of the lipid bilayer when long-pHLIP or short-pHLIP occupy the outer leaflet of bilayer at high pH, respectively, compared to the same liposomes with no peptide. Our results are also in agreement with the data obtained by Huang and co-authors indicating that amphipathic peptides, which adopt helical conformation at the surface

of bilayer, induce membrane thinning (*29, 30*). When a peptide is adsorbed into the surface of a bilayer, it pushes the lipid headgroups aside. Since the total volume of the chains is constant, this causes the membrane to thin. Thus, polypeptide that is adsorbed by a bilayer even in coil conformations, like in the case of pHLIPs, induces some membrane tension and stress, which leads to the membrane thinning. The interaction of short pHLIP with a membrane causes the membrane thinning to a lesser extent, since the affinity of truncated pHLIPs to lipid bilayer at pH 8.0 is lower (8), and according to the results of dual quenching and NBD-FRET assays short-pHLIP does not partition into a bilayer as deep as long-pHLIP. Our previous kinetics studies demonstrated the formation of a helical intermediate on the surface of a membrane during the folding and insertion of the long-pHLIP across the membrane (11). We suspect that the membrane thinning may reach a maximum value, when long-pHLIP transforms from coil configurations to the helical membrane-surface orientations. The transition from the helical membrane-surface conformations to the stable TM could be driven by the release of membrane tension and the restoration of the original membrane thickness. We propose to carry out kinetic SAXS measurements to monitor changes in the lipid bilayer of the membrane during pHLIP insertion and folding into the membrane.

When long-pHLIP inserts into a membrane at low pH, the thickness of bilayer is restored. However, at low pH in the presence of short peptide the membrane thins by about 18% of its original size. Low pH induces protonation of Asp/Glu residues and promotes propagation of the short-pHLIP into the bilayer. Our data indicates that the

peptide spans the bilayer. Since the peptide has a truncated TM part, its insertion into a membrane is expected to lead to a negative hydrophobic mismatch. As it was proposed early, there are number of ways a system might reduce negative energy of hydrophobic mismatch, such as the thinning of lipids, aggregation of peptides and stretching from the alpha-helical to 3_{10}-helical conformations. The ideal alpha-helix has a periodicity of 3.6 residues per turn, encloses 13 atoms in a ring by formation of an ***i, i* + 4** C=O:::H-N hydrogen bonds, making it a 3.6_{13}-helix. The 3_{10}-helix is a more tightly wound less stable helix, stabilized by ***i, i* + 3** C=O:::H-N hydrogen bonds. However, there is no disallowed region between the alpha-helical and the 3_{10}-helical conformations in the Ramachandran plot, and therefore transitions between helices can easily occur (44). Furthermore, the hydrophobic environment of protein interiors or lipid membranes could stabilize the 3_{10}-helix (45). There is a high probability to observe 3_{10}-helical segments as N- and C-terminal capping of an alpha-helix. The mixture of helical structures in a membrane and their transition from one to another was demonstrated to be important for biological function (*31-34*). Our data does not point to the aggregation of the peptide in membrane; however we cannot exclude that as a possibility. We can confirm the thinning of a bilayer as measured in SAXS experiments and the formation of a stretched 3_{10} helix or most probably mixture of alpha- and 3_{10}-helices with 3_{10} components at the beginning and end of alpha-helix.

Author Contributions

Designed Experiment: Andreev, Reshetnyak, Narayanan; **Performed Experiment**: Weerakkody, Karabadzhak, Anderson, Narayanan; **Analyzed Data**: Laliberte, Reshetnyak; **Wrote Paper**: Andreev, Reshetnyak, Narayanan.

Acknowledgements

This work was supported by NIH grants CA133890 and GM073857 to OAA and YKR. ESRF is acknowledged for synchrotron beam time.

References

1. Killian, J. A. (1998) Hydrophobic mismatch between proteins and lipids in membranes, *Biochim Biophys Acta 1376*, 401-415.

2. de Planque, M. R., and Killian, J. A. (2003) Protein-lipid interactions studied with designed transmembrane peptides: role of hydrophobic matching and interfacial anchoring, *Mol Membr Biol 20*, 271-284.

3. Cybulski, L. E., and de Mendoza, D. (2011) Bilayer hydrophobic thickness and integral membrane protein function, *Curr Protein Pept Sci 12*, 760-766.

4. Holt, A., and Killian, J. A. (2010) Orientation and dynamics of transmembrane peptides: the power of simple models, *Eur Biophys J 39*, 609-621.

5. Mondal, S., Johnston, J. M., Wang, H., Khelashvili, G., Filizola, M., and Weinstein, H. (2013) Membrane driven spatial organization of GPCRs, *Sci Rep 3*, 2909.

6. Nomura, T., Cranfield, C. G., Deplazes, E., Owen, D. M., Macmillan, A., Battle, A. R., Constantine, M., Sokabe, M., and Martinac, B. (2012) Differential effects of lipids and lyso-lipids on the mechanosensitivity of the mechanosensitive channels MscL and MscS, *Proc Natl Acad Sci U S A 109*, 8770-8775.

7. Gambin, Y., Reffay, M., Sierecki, E., Homble, F., Hodges, R. S., Gov, N. S., Taulier, N., and Urbach, W. (2010) Variation of the lateral mobility of transmembrane peptides with hydrophobic mismatch, *J Phys Chem B 114*, 3559-3566.

8. Weerakkody, D., Moshnikova, A., Thakur, M. S., Moshnikova, V., Daniels, J., Engelman, D. M., Andreev, O. A., and Reshetnyak, Y. K. (2013) Family of pH (low) insertion peptides for tumor targeting, *Proc Natl Acad Sci U S A 110*, 5834-5839.

9. Reshetnyak, Y. K., Segala, M., Andreev, O. A., and Engelman, D. M. (2007) A monomeric membrane peptide that lives in three worlds: in solution, attached to, and inserted across lipid bilayers, *Biophys J 93*, 2363-2372.

10. Reshetnyak, Y. K., Andreev, O. A., Segala, M., Markin, V. S., and Engelman, D. M. (2008) Energetics of peptide (pHLIP) binding to and folding across a lipid bilayer membrane, *Proc Natl Acad Sci U S A 105*, 15340-15345.

11. Karabadzhak, A. G., Weerakkody, D., Wijesinghe, D., Thakur, M. S., Engelman, D. M., Andreev, O. A., Markin, V. S., and Reshetnyak, Y. K. (2012) Modulation

of the pHLIP transmembrane helix insertion pathway, *Biophys J 102*, 1846-1855.

12. Karabadzhak, A. G., An, M., Yao, L., Langenbacher, R., Moshnikova, A., Adochite, R. C., Andreev, O. A., Reshetnyak, Y. K., and Engelman, D. M. (2014) pHLIP-FIRE, a cell insertion-triggered fluorescent probe for imaging tumors demonstrates targeted cargo delivery in vivo, *ACS Chem Biol 9*, 2545-2553.

13. Andreev, O. A., Engelman, D. M., and Reshetnyak, Y. K. (2014) Targeting diseased tissues by pHLIP insertion at low cell surface pH, *Front Physiol 5*, 97.

14. Cheng, C. J., Bahal, R., Babar, I. A., Pincus, Z., Barrera, F., Liu, C., Svoronos, A., Braddock, D. T., Glazer, P. M., Engelman, D. M., Saltzman, W. M., and Slack, F. J. (2015) MicroRNA silencing for cancer therapy targeted to the tumour microenvironment, *Nature 518*, 107-110.

15. Deacon, J. C., Engelman, D. M., and Barrera, F. N. (2015) Targeting acidity in diseased tissues: mechanism and applications of the membrane-inserting peptide, pHLIP, *Arch Biochem Biophys 565*, 40-48.

16. Sztucki, M., Di Cola, E., and Narayanan, T. (2010) Instrumental developments for anomalous small-angle X-ray scattering from soft matter systems, *J Appl. Cryst. 43*, 1479–1487.

17. Manning, M. C., and Woody, R. W. (1991) Theoretical CD studies of polypeptide helices: examination of important electronic and geometric factors, *Biopolymers 31*, 569-586.

18. Caputo, G. A., and London, E. (2003) Using a novel dual fluorescence quenching assay for measurement of tryptophan depth within lipid bilayers to determine hydrophobic alpha-helix locations within membranes, *Biochemistry 42*, 3265-3274.

19. Zoonens, M., Reshetnyak, Y. K., and Engelman, D. M. (2008) Bilayer interactions of pHLIP, a peptide that can deliver drugs and target tumors, *Biophys J 95*, 225-235.

20. McIntyre, J. C., and Sleight, R. G. (1991) Fluorescence assay for phospholipid membrane asymmetry, *Biochemistry 30*, 11819-11827.

21. Clausell, A., Rabanal, F., Garcia-Subirats, M., Asuncion Alsina, M., and Cajal, Y. (2006) Membrane association and contact formation by a synthetic analogue of polymyxin B and its fluorescent derivatives, *J Phys Chem B 110*, 4465-4471.

22. Galassi, V., Nolan, V., Villarreal, M. A., Perduca, M., Monaco, H. L., and Montich, G. G. (2009) Kinetics of lipid-membrane binding and conformational change of L-BABP, *Biochem Biophys Res Commun 382*, 771-775.

23. Brzustowicz, M. R., and Brunger, A. T. (2005) X-ray scattering from unilamellar lipid vesicles, *J. Appl. Cryst. 38*, 126-131.

24. Varga, Z., Berenyi, S., Szokol, B., Orfi, L., Keri, G., Petak, I., Hoell, A., and Bota, A. (2010) A closer look at the structure of sterically stabilized liposomes: a small-angle X-ray scattering study, *J Phys Chem B 114*, 6850-6854.

25. Varga, Z., Wacha, A., Vainio, U., Gummel, J., and Bota, A. (2012) Characterization of the PEG layer of sterically stabilized liposomes: a SAXS study, *Chem Phys Lipids 165*, 387-392.

26. Pabst, G., Rappolt, M., Amenitsch, H., and Laggner, P. (2000) Structural information from multilamellar liposomes at full hydration: Full q-range fitting with high quality x-ray data, *Phys Rev E Stat Nonlin Soft Matter Phys 62*, 4000-4009.

27. Pencer, J., Krueger, S., Adams, C. P., and Katsaras, J. (2006) Method of separated form factors for polydisperse vesicles, *J Appl. Cryst. 39*, 293.

28. Andreev, O. A., Dupuy, A. D., Segala, M., Sandugu, S., Serra, D. A., Chichester, C. O., Engelman, D. M., and Reshetnyak, Y. K. (2007) Mechanism and uses of a membrane peptide that targets tumors and other acidic tissues in vivo, *Proc Natl Acad Sci U S A 104*, 7893-7898.

29. Ludtke, S., He, K., and Huang, H. (1995) Membrane thinning caused by magainin 2, *Biochemistry 34*, 16764-16769.

30. Wu, Y., He, K., Ludtke, S. J., and Huang, H. W. (1995) X-ray diffraction study of lipid bilayer membranes interacting with amphiphilic helical peptides: diphytanoyl phosphatidylcholine with alamethicin at low concentrations, *Biophys J 68*, 2361-2369.

31. Handa, N., Kukimoto-Niino, M., Akasaka, R., Murayama, K., Terada, T., Inoue, M., Yabuki, T., Aoki, M., Seki, E., Matsuda, T., Nunokawa, E., Tanaka, A., Hayashizaki, Y., Kigawa, T., Shirouzu, M., and Yokoyama, S. (2006) Structure of the UNC5H2 death domain, *Acta Crystallogr D Biol Crystallogr 62*, 1502-1509.

32. Hiroaki, Y., Tani, K., Kamegawa, A., Gyobu, N., Nishikawa, K., Suzuki, H., Walz, T., Sasaki, S., Mitsuoka, K., Kimura, K., Mizoguchi, A., and Fujiyoshi, Y. (2006)

Implications of the aquaporin-4 structure on array formation and cell adhesion, *J Mol Biol 355*, 628-639.

33. Scapin, S. M., Carneiro, F. R., Alves, A. C., Medrano, F. J., Guimaraes, B. G., and Zanchin, N. I. (2006) The crystal structure of the small GTPase Rab11b reveals critical differences relative to the Rab11a isoform, *J Struct Biol 154*, 260-268.

34. Shafrir, Y., Durell, S. R., and Guy, H. R. (2008) Models of voltage-dependent conformational changes in NaChBac channels, *Biophys J 95*, 3663-3676.

Tables

Table 1. The percentage of quenching of Trp fluorescence of long-pHLIP and short-pHLIP in the presence of POPC liposomes at pH 8.0 and pH 4.0, by acrylamide and 10DN incorporated into liposomes. The data are calculated from the spectra shown on Figure 2.

	pH 8.0		**pH 4.0**	
	Acrylamide	**10-DN**	**Acrylamide**	**10-DN**
Short-pHLIP	79.1%	12.3%	48.1%	34.7%
Long-pHLIP*	44.1%	32.7%	31.1%	44.6%

Table 2. The mean and St.D. of the parameters calculated from the Gaussian fitting of several SAXS data obtained in different experiments. The mean and st.d. are shown in the Table. ρ_k, z_k and σ_k are the relative weight, position and width of the *k*-th Gauss function, respectively. For the bilayer $k = 1$ represents inner headgroups, $k = 2$ represents hydrocarbon tails, and $k = 3$ represents outer headgroups. We assume that the center of the bilayer coincides with the center of the hydrocarbon tail, which means $z_2 \sim 0 \pm 0.5$ nm. The R^2 varied in the range of 0.980 to 0.999 for all fits. The last row contains values of lipid bilayer thickness, d, calculated from the difference between z_1 and z_3.

	POPC	**Long + POPC, pH 8.0**	**Long + POPC, pH 4.0**	**Short + POPC, pH 8.0**	**Short + POPC, pH 4.0**
z_1	2.14±0.14	1.80±0.02	2.09±0.01	1.75±0.21	1.69±0.01
z_2	0.24±0.26	-0.17±0.33	0.15±0.50	-0.44±0.51	-0.31±0.27
z_3	-2.23±0.16	-2.03±0.04	-2.14±0.06	-2.30±0.28	-1.89±0.02
ρ_1	2.68±0.29	3.00±0.00	3.10±0.13	3.75±0.21	2.90±0.14
ρ_2	-2.00±0.00	-2.00±0.00	-2.00±0.00	-2.23±0.39	-2.00±0.00
ρ_3	2.63±0.46	2.80±0.01	2.92±0.45	2.84±0.27	2.70±0.14
σ_1	0.232±0.104	0.315±0.092	0.196±0.085	0.202±0.047	0.577±0.043

σ_2	0.326±0.007	0.501±0.156	0.377±0.122	0.434±0.136	0.900±0.141
σ_3	0.114±0.028	0.107±0.004	0.191±0.129	0.112±0.053	0.316±0.042
d	4.37±0.03	3.83±0.04	4.23±0.04	4.05±0.07	3.58±0.01

Figures

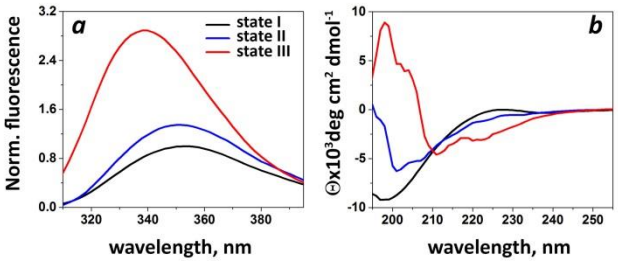

Figure 1. Three states of short-pHLIP. The states were monitored by changes of tryptophan fluorescence (***a***) and CD (***b***). The state I (black lines) represents peptide in solution at pH 8.0. The state II (blue lines) is a peptide in a solution in the presence of POPC liposomes at pH 8.0. The state III (red line) is a peptide in a solution in the presence of POPC liposomes at pH 4.0.

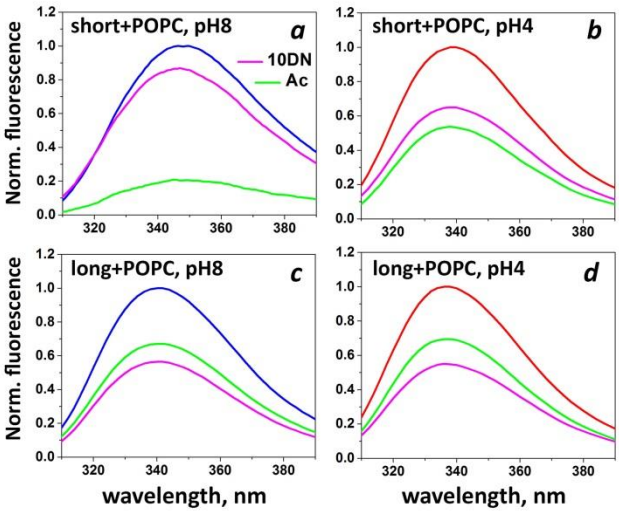

Figure 2. Dual-quenching assay. The tryptophan fluorescence of short-pHLIP (***a***, ***b***) and long-pHLIP (***c***, ***d***) in the presence of POPC liposomes at pH 8.0 (blue lines) and pH 4.0 (red lines) are shown. The emission of tryptophan residues of the peptides in the presence of POPC liposomes at both pHs is quenching by 10DN (magenta lines) or acrylamide (green lines). The amount of quenching is given in Table 1.

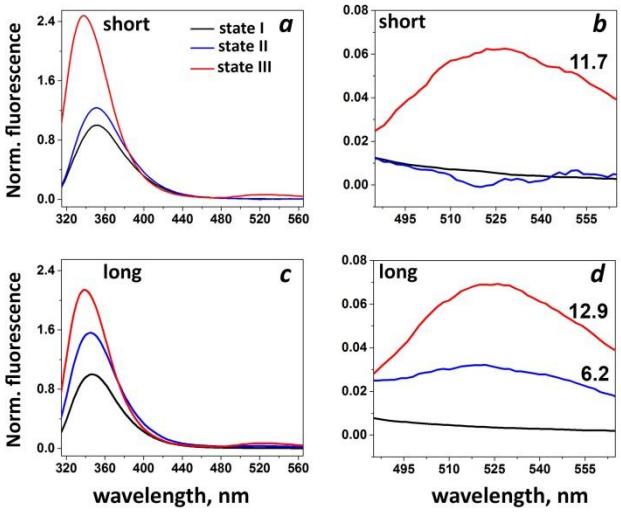

Figure 3. NBD-FRET assay. The tryptophan fluorescence of short-pHLIP (***a***, ***b***) and long-pHLIP (***c***, ***d***) in three states are shown. We used asymmetrically-labeled (by NBD) POPC liposomes to record spectra of peptides in the states II and III. Energy transfer from tryptophan residues to NBD dye at the inner leaflet of bilayer was monitored (***b***, ***d***). The numbers on panels ***b*** and ***d*** indicate the increase of NBD fluorescence in states III and II compared to the baseline (black lines).

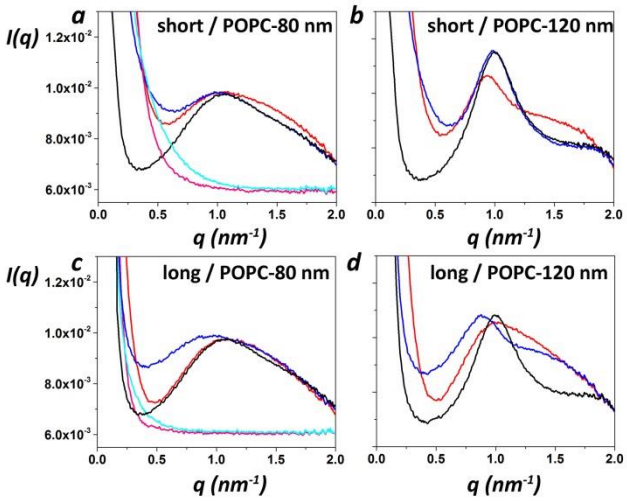

Figure 4. SAXS intensities obtained from the POPC liposomes (~80 nm (***a***, ***d***) and ~120 nm (***b***, ***d***) in diameter) alone (black lines), the peptides at pH 8.0 (cyan lines) and pH 4.0 (magenta lines), the peptide in the presence of POPC liposomes at pH 8.0 (blue lines) and pH 4.0 (red lines) are shown. These are the representative data showing only the bilayer form factor.

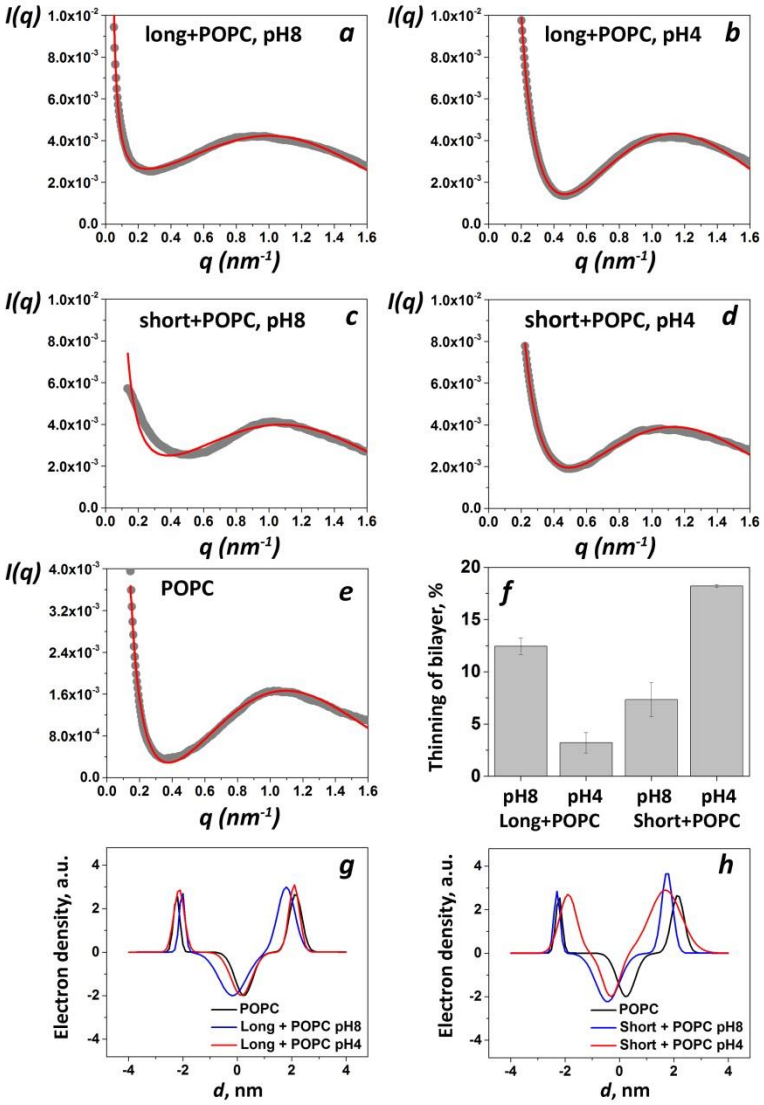

Figure 5. Fittings of SAXS data. The averaged buffer background was subtracted from each intensity profiles of liposomes in the absence and presence of long and short peptides. The fitting was performed using Gaussian electron density model of lipid bilayer for POPC liposomes (80 nm in diameter) in the absence and presence of peptides at different pHs (***a***-***e***). The averaged fit parameters are given in the Table 2. The representative data are shown. The mean and st.d. for the percentages of bilayer thinning for long- and short-pHLIPs in the presence of POPC at pHs 8.0 and 4.0 are shown on panel ***f***. The electron density profiles of bilayer of POPC liposomes in the

absence and presence of long-pHLIP (***g***) and short-pHLIP (***h***) at pHs 8.0 and 4.0 are presented.

CHAPTER 4

In Preparation forPublication

pH at the surface of cancer cells measured *in vitro, in vivo* and *ex vivo*

Michael Anderson[1], Linden Wyatt[1], Gregory Andreev[1], James Segala[1], Anna Moshnikova[1], Donald M. Engelman[2], Yana K. Reshetnyak[1], Oleg A. Andreev[1]

[1]Physics Department, University of Rhode Island, 2 Lippitt Road, Kingston, RI 02881 USA

[2]Department of Molecular Biophysics and Biochemistry, Yale University, PO Box 208114, New Haven, CT 06520, USA

KEYWORDS: Imaging acidity, SNARF, fluorescence, pHLIP, insertion into plasma membrane, extracellular pH, metastatic tumor

Abstract

It is important to measure pH at the surface of cells in diseased tissue with accuracy and precision, since acidity is associated with the development of various pathological states including tumors, ischemic stroke and acidity has the lowest pH at cell surface. We have introduced a novel approach of extracellular pH measurements at the surface of cells, which is based on the use of a pH-sensitive fluorescent dye SNARF conjugated to a pH Low Insertion Peptide (WT-pHLIP), which targets plasma membranes of cells in acidic diseased tissue. Our experimental set up includes two different approaches, one is based on acquisition of fluorescent spectra, and other one is based on recording of images via two emission filters. By using appropriate calibration curves obtained on liposomes and tumor spheroids in the presence of 2-deoxyglucose, both approaches give the same values of surface pH. The developed tool was validated on cancer cells grown in tumor spheroids, in mice and excised tumors *ex vivo*. We establish that highly metastatic cancer cells have lower pH at their surface compared to non-metastatic cells. Our approach was sensitive enough to detect pH changes *in vitro* and *in vivo* induced by glucose, which leads to the enhancement of cancer cells metabolism and acidification of the extracellular space. The introduced tool could be developed for clinical application of surface pH measurements in biopsy samples. It might provide important clinical information about tumor stage and invasiveness, and can guide in the choice of treatment approach.

Introduction

Acidity is associated with development of various pathological states such as tumors, ischemic stroke, neurotrauma, epileptic seizure, inflammation, infection, wounds and others(1-3). Thus, it becomes increasingly important to be able to measure pH with accuracy, precision, and high spatiotemporal resolution in experimental systems of cell culture, animal models and in human beings.

The pH electrodes are used for accurate pH measurements in solution. As such microelectrodes were the first method used to probe pH in living tissue. However they are highly destructive to the tissue and are weighted to the extracellular pH(4, 5). Later on noninvasive pH measurement methods were developed that could measure either the pHi, intracellular pH, pHe, extracellular pH, or both. PET has been used for measuring tissue pH using radiolabeled dimethadione, which distributes in intracellular and extracellular space according to the pH gradient across membranes (6). Unfortunately, dimethadione's distribution depends on the transmembrane pH gradient and the fractional volumes of intra- and extracellular space, both of which are unknown. *In vivo* MRS and MRI have been used to monitor metabolic and physiologic processes employing endogenous and exogenous nuclear MR–active compounds (7). MRS methods are generally based on a difference in chemical shifts between pH-dependent and -independent resonances. Several isotopes have been evaluated to determine tissue pH with MRS. ^{31}P-MRS provides a robust technique for simultaneously measuring pHi from the chemical shift of endogenous inorganic phosphate and pHe from the chemical shift of exogenous indicators, such as 3-

aminopropyl phosphonate (8). Tumor pH was also measured using hyperpolarized ^{13}C bicarbonate (9, 10). One of the limitations of dynamic nuclear hyperpolarization is that the hyperpolarized nuclear spin signal decreases rapidly according to spin-lattice relaxation, T1. Therefore, measurements must be completed within 1–2 min after injection. Another approach using MRI relies on perturbing the relaxivity of water via pH-dependent relaxation agents such as tetraphosphonate, gadolinium-DOTA-4AmP52 (7, 11).

The described above studies showed that tumor pHe is heterogeneous and acidic. However, these methods are still limited in spatial resolution and cannot measure pH on a cellular level. Only optical methods can provide cellular resolution. Fluorescence imaging was employed to study pH at the surface of cultured cancer cells and monitor behavior of individual fluorescent cancer cells in the heterogeneous microenvironments of tumors (12-16). For pH-imaging mostly pH-sensitive dyes, fluorescence intensity of which is changed in a response of pH, are used. However, accurate calibration for the probe concentration is needed. pH-sensitive and pH-insensitive fluorophores were used to functionalize the bacteriophage particles with many copies of these dyes and perform *in vivo* imaging (15). However, the bacteriophages particles are taken by endocytosis, thus reporting pH primarily in endosomes. Fluorescence lifetime imaging is based on measurements of a fluorophore's excited state lifetime, which changes in accordance with pH alterations. However, lifetime measurements are more complicated, especially for the measurements in the nano sec range, which is a typical lifetime of most of organic

dyes (including pH-sensitive ones). One of the approaches is to use long-lived (micro seconds) metal-chelate complexes (they mostly exhibit phosphorescence signal). However, most of them have short wavelength of excitation (<450 nm), which has low tissue penetration (17, 18). Despite the fact that optical imaging can provide single-cell resolution *in vivo*, in order to measure pH on the surface of individual cell the pH-sensitive probe needs to be located close to the plasma membrane. In most cases, the pH-sensitive agents were small molecules distributed in entire organ/tissue and blood (where pH is normal) and washed out from the body very quickly. In case of use of nanocarries (nanoparticles or bacteriophage particles), cells internalize them readily via endocytotic pathway, thus pH could be reported predominately in endosomes. The use of antibody or receptor targeting peptides/molecules could also lead to their internalization. The lipids or fatty acids conjugated with pH-sensitive probes (13, 19) could be used for pH measurements on cellular level, but they are not selective to cells in disease site, they will incorporate into any cellular membrane, and can readily undergo flipping and participate in lipid exchange, thus making problematic identification of their exact location, especially in *in vivo* experiments.

We propose a novel approach of pH measurements at the surface of cells, which is based on use of a pH-sensitive fluorescent dye SNARF conjugated to a pH Low Insertion Peptide (pHLIP). Peptides of pHLIP family insert into the lipid bilayer of a membrane in a pH-dependent manner exposing N-terminus to the extracellular space and translocating C-terminus across membrane into cytoplasm (20-23). The molecular mechanism of pHLIP action is based on protonation of Asp/Glu residues, which

enhance peptide hydrophobicity and promotes membrane-associate folding and formation of transmembrane helix (24, 25). pHLIP labeled with optical, PET or SPECT probes target acidic diseased tissue and are considered to be novel acidity markers (26-33). A novel tool for mapping pH at the extracellular surface of cell, we introduced here, might open an opportunity to contribute in understanding of diseases progression and development of approaches of pH-based image-guided interventions.

Materials and Methods

Peptide Synthesis and Conjugation with Fluorescent Dyes

A pHLIP peptide with a single Lys residue at the N-terminus (the N-terminus is acytilated): Ac-AKEQNPIYWARYADWLFTTPLLLLDLALLVDADEGT was synthesized and purified by reverse phase chromatography by CS Bio. SNARF-1 carboxylic acid, acetate, succinimidyl ester (Life Technologies) was conjugated to pHLIP at a ratio of 2:1 in 60% DMF (dimethylformamide), 30% 0.1 M PBS pH 9.0 and 10% pH 9.5 0.1 M sodium bicarbonate buffer for a final pH of 9.0. SNARF-1 was converted to its fluorescent form after conjugation by raising the conjugation solution's volume by 50% with methanol and raising the solution pH to 14 with 2 M potassium hydroxide for 1 hour. The reaction progress was monitored by reverse phase (Zorbax SB-C18 columns, 9.4 × 250 mm 5 μm, Agilent Technology) high-performance liquid chromatography (HPLC) using a gradient of 25−75% acetonitrile and water containing 0.05% of trifluoroacetic acid. The concentration of each labeled peptide in buffer was determined by SNARF-1 absorption at 548 nm, ε_{548}=27,000 M^{-1}

cm^{-1}. The purity and characterization of the constructs was performed by analytical HPLC and SELDI-TOF mass spectrometry.

Phosphate Buffered Solutions

Phosphate buffered solutions were created by mixing 0.5 M dibasic and mon-basic solutions (J.T. Baker) to obtain desired pH in the range of 5.5 to 8.0. The final PBS solutions (experimental PBS) used in experiments contained 10 mM of phosphate, 150 mM NaCl (J.T. Baker), 0.2 mM $MgCl_2$ (Sigma) and 0.2 mM $CaCl_2$ (Sigma) were added. The pH of the final solution was measured with a microelectrode pH meter (Thermo Scientific). Buffer solutions

were sterilized by passing them through a 200 μm filter.

Liposome preparation

Large unilamellar vesicles were prepared by extrusion. 2.5 mg POPC (1-palmitoyl-2-oleoyl-snglycero-3-phosphocholine, Avanti Polar Lipids, Inc.) lipids were dissolved in 0.5 mL chloroform and desolvated on a rotary evaporator and dried under high vacuum for 3 hours. The phospholipid film was then rehydrated in pH 7.4 experimental PBS, vortexed for 5 minutes, and repeatedly extruded through a membrane with a 50 nm pore sizes.

Cell lines

Human cervical adenocarcinoma HeLa, human melanoma M4A4, human melanoma NM2C5 and mouse breast cancer 4T1 cell lines were purchased from the American

Tissue and Culture Collection (ATCC). All lines were propagated in DMEM (Dulbecco's Modified Eagle Medium) containing 4.5 g/L D-glucose and 40 mg/L sodium pyruvate supplemented with 10% FBS (fetal bovine serum) (Gibco), ciprofloxacin-HCl (10 µg/mL) (from Cellgro, Voigt Global Distribution) in a humidified atmosphere of 5% CO_2 at 37°C.

Tumor Spheroids

150 µL of 1% agarose (Sigma) in x1 strength PBS pH 7.4 (Gibco) was pipetted into each well of a 48 well flat bottom tissue culture plate (Celltreat). After the agarose gel had sufficiently settled (~1 hour), 200 µL of DMEM supplemented with 10% FBS, ciprofloxacin-HCl was then added to each well. The covered tray was then left in a humidified atmosphere at 37˚C, 5% CO_2 for 24 hours. Next a suctioned glass Pasteur pipette was used to remove excess media from the agarose layer. Then 200 µL of the same DMEM with 10,000 HeLa, NM2C5 or M4A4 cells were seeded into each well and kept in a humidified atmosphere of 5% CO2 at 37°C for 3-4 days. In case of matrigel (Corning) use, it was dissolved on ice in DMEM at a concentration of 2.5% (would be diluted till 2% once added to well) and then heated to 37˚C before combining with cells to be seeded.

Tumor Mouse Models

All animal studies were conducted according to the animal protocol AN04-12-011 approved by the Institutional Animal Care and Use Committee at the University of Rhode Island, in compliance with the principles and procedures outlined by NIH for

the Care and Use of Animals. Subcutaneous tumors were established by injection of HeLa, M4A4, NM2C5 and 4T1 cells (8 × 105 cells/0.1 mL/flank) in the right flank of adult female athymic nude mice (for implanting of human cancer cell lines: HeLa, M4A4 and NM2C5) and adult female BALB/c mice (for implanting of murine cancer cell line, 4T1). Mice were about 20−22 g and were obtained from Harlan Laboratories.

Imaging Tumor Spheroids

The spheroids of a given cell line were incubated with 5 μM of SNARF-pHLIP into 50 μL of pH 6.3 experimental PBS buffer either with 25 mM D-glucose (glucose) or 50 mM 2-deoxyglucose (2DG) in an open Eppendorf in a humidified atmosphere of 5% CO2 at 37°C for 30 minutes. The spheroids were then washed 3 times with 1 mL of experimental PBS of a pH that was desired for the observation. The spheroids were then placed into an open Eppendorf with 1 mL of same PBS followed by washing with PBS containing either 25 mM glucose or 50 mM 2DG for 15 minutes. The spheroids were transferred to a single well of a glass bottom 96 well cell tray and fluorescence signal was obtained onto an inverted epi-fluorescent microscope (Olympus IX71) using 20x objective. Both spectra and images of the SNARF-pHLIP from tumor spheroids were obtained using the same excitation filter of FF01-531/40-25 (Semrock) with transmittance at 531 ± 20 nm. The fluorescence spectra from tumor spheroids were recorded by an Solis software (Andor) after emission from the sample was passing through a long pass emission filter of BCP01-568R-25 (Semrock)with transmittance at 580 nm and higher and an shamrock SR-303i-B spectrograph (Andor) with a diffraction grating of 300 l/mm blaze 500 nm, 400 μm entrance slit and a

Newton^{EM} EMCCD (Andor) camera thermoelectrically cooled to -60˚C. Spectra were taken every several minutes until 3 in a row were identical. After spectra recording, the fluorescent images were acquired using Qcapture software by a Retiga-SRV CCD (Qimaging) with two emission filters FF01-580/14-25 (Semrock) and FF01-640/14-25 (Semrock) with transmittance at 580 ± 10 nm and 640 ± 10 nm, respectively.

Trypan Blue Assay

Trypan blue solution (Sigma) at concentration of 0.67 M in experimental PBS of pH 7.0 was added to a HeLa spheroid, which was incubated with SNARF-pHLIP as described above, in a glass bottom collagen coated cell dish (MatTek). The fluorescence spectra and images before and immediately after addition of Trypan Blue were taken as described above with 20x objective.

In vivo Imaging of Tumors

When tumor reached 5-8 mm in diameter, mouse was subjected to a starvation (no food) for 24 hours before a single tail vein injection of 4 nmol (100 μL of 40 μM) of SNARF-pHLIP in PBS was performed. At 4 hours after construct administration, the skin was removed from tumor site under ketamine/xylazine anesthesia and mouse tumor was placed onto a 24 x 60 mm NO 1 thickness glass slide and imaged on fluorescent microscope using objective with 20x magnification as described above. The SNARF-pHLIP fluorescent spectra and images were taken from various areas of tumor before and after an intra-peritoneal injection of 125 mg of glucose (125 mg in 220 μL of PBS pH 7.4). After *in vivo* imaging animal was euthanized by cervical

dislocation and tumor was excised, cut in half and fluorescence spectra and images were acquired immediately as described above.

Ex vivo Imaging of Tumors

When tumor reached 5-8 mm in diameter mouse was euthanized and tumor was excised. The tumor was cut into slices and placed into 150 µL, 1 µM solution of SNARF-pHLIP experimental PBS of pH 6.3 with either no glucose or 25 mM glucose. The slices were left to incubate with SNARF-pHLIP for 1 hour and washed 3 times with 150 µL of experimental PBS of pH7.4 with 15 minutes between washings. Then slices were placed into glass bottom dish and imaged on an inverted epi-fluorescent microscope with 20x objective. Spectra and images were acquired in the same manner as described above.

SNARF-pHLIP Liposome Calibration

300 µL of 1 µM SNARF-pHLIP and 200 µM of POPC liposomes were mixed into pH 7.4 experimental PBS and left to incubate over night at 4˚C. The pH was adjusted by adding 0.5 M hydrochloric acid or 2 M of potassium hydroxide and final pH of the solution was measured with a microelectrode pH meter (Thermo Scientific). The solution was placed into a glass bottom collagen coated cell dish (MatTek) and imaged on a fluorescent microscope with an objective of 20x magnification. Images and spectra were taken in a similar manner as described above.

Spectra and Image Analysis

The fluorescent spectra and images of SNARF were analyzed by our programs. The spectra were analyzed with a Mathematica program (Version 10, Wolfram), and images were analyzed using Matlab program (Mathworks) both introduced by us. The description of the program is provided in the Result section. All graphs were constructed using Origin Lab (Version 9.1, Origin Lab Corporation). The p-level values were computed based on the two-tailed test.

Results

Various pathological states are associated with extracellular acidity. There is a proton gradient, which decays with the distance from a cell in acidic areas. Thus, the lowest values of pH are expected to be at the surface of cells. We have developed a novel tool for pH measurement at the surface of cells and validated it *in vitro* on liposomes, different cancer cell lines grown in tumor spheroids, *in vivo* in mice and *ex vivo* on tumor and muscle tissue samples. Among cancer cell lines we selected highly metastatic human cervical adenocarcinoma HeLa, and two human melanoma cell lines, M4A4 and NM2C5, derived from the same origin, MDA-MB-435, where M4A4 is a highly metastatic, while NM2C5 is non-metastatic(34, 35).

Our approach to measure pH at the surface of cells is based on use of WT-pHLIP, which inserts into a cellular membrane and forms a transmembrane helix translocating the C-terminal end into the cytoplasm and exposing the N-terminal end to the extracellular space. Additionally the pHLIP has multiple protonatable residuesat the membrane-inserting C-terminal end, which are deprotonated in the cytoplasm and

serve as additional anchoring point for the peptide in membrane. Thus, once WT-pHLIP is inserted into a plasma membrane, the rate of its exit from membrane is very low even when extracellular pH is raised. This opens up an opportunity to treat cells with WT-pHLIP at low pH and then raise pH of media for measurments. The acetylated N-terminus of the peptide contains a single Lys residue, which was conjugated with a SNARF-1 dye and this dye was subsequently converted to its fluorescent form by chemical activation. The product was purified and characterized and used in all experiments.

Our choice of ratiometric pH-indicator, SNARF, was dictated by the fact that pH values could be established independent of the dye's concentration, which was used previously to measure pH in vivo (16). SNARF also has other desirable characteristics such as high excitation and emission wavelengths, two fairly fluorescent peaks and it runs in a single excitation dual emission configuration. The SNARF-pHLIP was excited by the xenon lamp attached to the inverted epi-fluorescent microscope in the range of 531 ± 20 nm as selected by an excitation filter. The emission was detected by two different set ups: i) fluorescence was passed via emission cut off filter for the detection of light at wavelengths from 580 nm and higher. The spectrograph connected to the microscope allowed to record entire fluorescence spectra from 500 to 800 nm simultaneously (Figure 1A). Our program in Mathematica performs a smoothing of spectra and establishes the emission maximums of the SNARF-pHLIP and their ratio $\frac{F_{595\pm1}-background}{F_{645\pm1}-background}$. While recording of spectra is very useful, it does require special instrumentation. For that reason it is more practical to acquire images. Thus, another

approach we developed is based on acquisition of two fluorescent images via two emission filters 580 ± 7 nm and 640 ± 10 nm (Figure 1B, C). We designed program in Matlab, called Cell Fluorescence Analysis (CFA), for image analysis. First, it aligns 580 nm and 640 nm emission images on a pixel by pixel basis. The CFA program is based on the identification of the position of individual cells by looking for high contrast around cell edges. It uses a threshold value for the size of a cell to exclude any signal coming from objects smaller in size than a cell. Next, pixel-by-pixel background subtraction is processed, followed by thecalculation of an average intensity within a cell and 580/640 nm ratio values.

The main idea of our approach is to measure pH at the surface of cells. To prove that SNARF is indeed located in the extracellular space we imaged cells in HeLa tumor spheroids before (Figure 2A) and immediately after (Figure 2B) treatment with membrane-impermeable Trypan Blue, which is capable of quenching of emission of fluorophores in the range of 500-600 nm (36). The fluorescence of the SNARF-pHLIP in this region was completely quenched indicating that SNARF is located in the extracellular space. The spectra of the SNARF-pHLIP before and after addition of Trypan Blue are shown on Figure 2C (the emission at 680 nm is associated with Trypan Blue). The bright field images of cells indicated that the vast majority of cells were viable.

A critical step is the identification of calibration curves to transfer 595/645 ratio values into pH values. The ratio of emission at 595 nm to 645 nm was calculated from the

fluorescence spectra of the SNARF-pHLIP treated with POPC liposomes at various pHs, which were recorded under microscope. The ratios were used to establish a calibration curve, since pH in bulk of the solution, at the surface of liposomes, where most of the SNARF-pHLIP is located, and even inside a liposome are equilibrated quickly (25, 37). We could not exclude the possibility that the SNARF signal and thus, calibration curve, might be different when the SNARF-pHLIP is located at the surface of real cells, which would not be unexpected given that nigericin calibrated intracellular SNARF curves differ from that of SNARF in solution(38)Therefore, we used 3 cell lines, HeLa, M4A4 or NM2C5, treated with the SNARF-pHLIP to record the spectra at various pHs. However, to establish the calibration, pH at the surface of cancer cells needs to be equilibrated with bulk extracellular pH, which could be achieved by preventing pumping of protons into extracellular space. This situation can be achieved by incubating tumor spheroids before imaging with 50 mM of non-metabolizable analog of glucose, 2-deoxyglucose (2DG). Treatment of cancer cells with 2DG inhibits fermentative metabolism and hence the proton production and proton flux, as confirmed previously using the Seahorse extracellular flux analyzer (39). Indeed, all 3 cell lines demonstrated the same ratio of the fluorescence at 595/645 nm, which coincides with the ratios obtained on liposomes (Figure 3A). We used the obtained liposome data to introduce a calibration curve, since pH at the surface of liposomes and cells treated with 2DG is the same as pH of the bulk solution, which could be controlled. The linear fitting was performed to establish the calibration curve:

$$pH_s{}^{spectra} = (8.459 \pm 0.031) - (1.223 \pm 0.024) \cdot Ratio_{595/645}{}^{spectra}$$

(1)

Since fluorescent images are obtained at different experimental settings and processed by different mathematical algorithm, we established separate calibrations curve (Figure 3B):

$$pH_s{}^{images} = (8.221 \pm 0.035) - (1.191 \pm 0.030) \cdot Ratio_{580/640}{}^{images}$$

(2)

Thus, equations (1) and (2) will be used for the processing of fluorescence ratios obtained from spectra and images, respectively. The developed tool was applied to establish pH at the surface of metastatic (HeLa and M4A4) and non-metastatic (NM2C5) cancer cells grown in tumor spheroids in presence of 50 mM glucose, which enhances and promotes cellular metabolism (Figure 3C). It is important to outline that the pH at the surface of metastatic cancer cells does not increase more than value of 7.0 even when the pH of bulk solution is around 7.9. Non-metastatic cancer cells are less acidic compared to metastatic, especially in the range of normal pH values. With a decrease of pH we observed equilibration of cell-surface pHs and bulk pH of media. When the pH of media is less than 6.4, the pH at the surface of cancer cells in average did not decrease accordingly and did not dip below 6.35. The images were analyzed by the CFA program, which establishes the pH of the most bright cells. This data was correlated well with the results obtained by spectra analysis.

The advantage of our approach is in its applicability for pH measurements *in vivo*, since pHLIP can target acidic diseased tissue and tether imaging agents, including fluorescent, to the surface of cells (27). To validate this approach *in vivo*, we grew metastatic, HeLa and M4A4, and less metastatic, NM2C5 tumors in mice. When the tumors reached about 5-8 mm in diameter, the mouse was placed in condition of starvation for 24 hours in order to reduce flux of glucose to cancer cells from blood and increase pH in the tumor as much as possible, followed by single IV injection of the SNARF-pHLIP construct. At 4 hours post-injection, the mouse was anesthetized and the skin was removed from the tumor site. Fluorescent spectra and images were recorded from the tumor surface (the image is shown in Figure 4A). Then, the mouse obtained a single IP injection of solution of glucose. It was shown previously that the average extracellular pH decreases after glucose administration and reaches a minimum level 0.3 pH units below the initial value (40). We observed spectra changes after 40 minutes post-injection of glucose (Figure 4B), no further spectral changes occurred after 40 minutes, which indicated acidification of tumor as monitored by our approach. Finally, the animal was euthanized, tumor was excised, cut in half and fluorescence was recorded from the center of the tumor. Figure 4C represents the mean of the surface pHs in tumor surface before and after glucose injection and in the center of the tumor. HeLa tumors are the most acidic even after 24h starvation period. The mean values of surface pH in the center of HeLa, M4A4 and NM2C5 tumors are 6.51±0.22, 6.68±0.41 and 6.94±0.29, respectively with some HeLa tumors having pH as low as pH 6.1. M4A4 and NM2C5 tumors had similar pH before glucose injection, while pH was reduced more significantly in metastatic M4A4 tumor compared to non-

metastatic NM2C5 tumors after glucose injection. Finally, we performed analysis of tumor tissues excised from mice and immediately treated with the SNARF-pHLIP *ex vivo* for 1 hour followed extensive washing and imaging SNARF fluorescence at 580 nm and 640 nm. Treatment was performed in PBS of pH7.4 in absence and presence of glucose. Glucose in solution promotes cellular metabolism selectively in glycolytic, highly metastatic cancer cells and enhances acidity near their surfaces. Thus, pHLIP preferentially inserts into plasma membrane of cells with low pH at the surface, such as cancer cells. At the same time, glucose does not affect significantly non-glycolytic cells in healthy tissue, which has normal surface pH(41). In Figure 4D we demonstrate the mean values of the surface pHs in highly metastatic human HeLa and murine 4T1 mammary tumor samples before and after treatment with glucose. The surface pHs dropped on 0.2 and 0.6 pH units from pH 6.7±0.3 to pH 6.5±0.4 and from pH 6.8±0.2 to pH 6.2±0.2 in HeLa and 4T1 tumor samples, respectively.

Discussion

Hypoxic conditions induce in a cell switch from the oxidative-phosphorylative mechanism of energy production to the glycolytic mechanism. In addition, malignant cancers have an elevated glucose uptake even under normal oxygen conditions, known as "aerobic glycolysis" or the Warburg effect (42-44). Glycolysis results in much higher level of the production of H^+ and lactic acid, the byproducts, which are readily pumped across a plasma membrane into the extracellular space and accumulate there, in poor-perfused regions such as solid tumor and ischemic stroke (45-47). Another contributor to extracellular acidity is associated with the expression of the carbonic

anhydrase enzymes on the tumor cell surface, which catalyze the extracellular trapping of acid by hydrating cell-generated CO_2 into HCO_3^- and H^+ (48, 49). All these mechanisms contribute towards an acidic extracellular milieu favoring diseases development and progressions. The extracellular pH of solid tumors plays one of the essential roles in almost all steps of metastasis: more acidic tumors became highly aggressive and metastatic (50). It was shown that the pH near the cell surface is the lowest and acidity decays with distance from a cell (13). Thus, the pH at the surface of a cell should reflect the best the stage of pathology development. The tool we introduced allow the measurement of pH at the surface of cells in acidic diseased tissue. The method was validated on metastatic and non-metastatic cancer cells grown in tumor spheroids and *in vivo* in mice. The approached is sensitive enough to detect differences in a pH at the surface of non-metastatic (less acidic) and metastatic tumors, and monitor enhancement of acidity and alteration of pH *in vivo* by injection of glucose. The mean values of pH at the surface of cancer cells in the center of highly metastatic (HeLa and M4A4) tumors were found to be 6.5-6.7. While pH at the surface of cancer cells in non-metastatic tumors (NM2C5) was pH 6.9. The obtained values are about 0.2-0.4 pH units lower than pH values of the bulk extracellular space measured by ^{31}P MRS in various mice and rat tumor models, which were varied from pH 6.7 to pH 7.0 (the normal tissue pH was established to be 7.3-7.4) (51).

We demonstrated that pH at the surface of cancer cells, especially metastatic cells, could be 0.6-0.8 pH units lower even when bulk pH is normal. It might open up an opportunity for clinical applications of the developed tool for the measurements of

pHs in biopsy samples. We validated our approach on mice tumor tissue samples. We established that treatment of tumors with the SNARF-pHLIP in normal pH buffer of 7.4 in presence of glucose can reduce surface pHs on 0.6 pH unit till about pH 6.2 values. Next, we propose to validate our approach on human samples of breast and bladder tumors obtained after surgery and correlate surface pHs with stage of tumor development and appearance of specific markers predictive of cancer invasiveness. If successful, it will introduce a new simple and fast clinical test, which can take about 30-40 min of biopsy sample treatment with the SNARF-pHLIP, quick washing step, imaging and data processing. After the procedure, the sample will undergo standard HE staining and histopathalogical analysis. The proposed method potentially might provide important clinical information about tumor stage and invasiveness, and can guide in the choice of treatment approach.

References

1. Pezzulo AA, *et al.* (2012) Reduced airway surface pH impairs bacterial killing in the porcine cystic fibrosis lung. *Nature* 487(7405):109-113.

2. Paschen W, Djuricic B, Mies G, Schmidt-Kastner R, & Linn F (1987) Lactate and pH in the brain: association and dissociation in different pathophysiological states. *J Neurochem* 48(1):154-159.

3. Kedika RR, Souza RF, & Spechler SJ (2009) Potential anti-inflammatory effects of proton pump inhibitors: a review and discussion of the clinical implications. *Dig Dis Sci* 54(11):2312-2317.

4. Griffiths JR (1991) Are cancer cells acidic? *Br J Cancer* 64(3):425-427.

5. Wike-Hooley JL, Haveman J, & Reinhold HS (1984) The relevance of tumour pH to the treatment of malignant disease. *Radiother Oncol* 2(4):343-366.

6. Rottenberg DA, *et al.* (1985) In vivo measurement of brain tumor pH using [11C]DMO and positron emission tomography. *Ann Neurol* 17(1):70-79.

7. Zhang X, Lin Y, & Gillies RJ (2010) Tumor pH and its measurement. *J Nucl Med* 51(8):1167-1170.

8. Lora-Michiels M, *et al.* (2006) Extracellular pH and P-31 magnetic resonance spectroscopic variables are related to outcome in canine soft tissue sarcomas treated with thermoradiotherapy. *Clin Cancer Res* 12(19):5733-5740.

9. Gallagher FA, *et al.* (2008) Magnetic resonance imaging of pH in vivo using hyperpolarized 13C-labelled bicarbonate. *Nature* 453(7197):940-943.

10. Gallagher FA, Kettunen MI, & Brindle KM (2011) Imaging pH with hyperpolarized 13C. *NMR Biomed* 24(8):1006-1015.

11. Zhang S, Wu K, & Sherry AD (1999) A Novel pH-Sensitive MRI Contrast Agent. *Angew Chem Int Ed Engl* 38(21):3192-3194.

12. Helmlinger G, Yuan F, Dellian M, & Jain RK (1997) Interstitial pH and pO2 gradients in solid tumors in vivo: high-resolution measurements reveal a lack of correlation. *Nat Med* 3(2):177-182.

13. Stock C, *et al.* (2007) pH nanoenvironment at the surface of single melanoma cells. *Cell Physiol Biochem* 20(5):679-686.

14. Schreml S, *et al.* (2011) 2D luminescence imaging of pH in vivo. *Proc Natl Acad Sci U S A* 108(6):2432-2437.

15. Hilderbrand SA, Kelly KA, Niedre M, & Weissleder R (2008) Near infrared fluorescence-based bacteriophage particles for ratiometric pH imaging. *Bioconjug Chem* 19(8):1635-1639.

16. Gatenby RA, Gawlinski ET, Gmitro AF, Kaylor B, & Gillies RJ (2006) Acid-mediated tumor invasion: a multidisciplinary study. *Cancer Res* 66(10):5216-5223.

17. Hynes J, *et al.* (2009) In vitro analysis of cell metabolism using a long-decay pH-sensitive lanthanide probe and extracellular acidification assay. *Anal Biochem* 390(1):21-28.

18. Murtaza Z, Chang Q, Rao G, Lin H, & Lakowicz JR (1997) Long-lifetime metal-ligand pH probe. *Anal Biochem* 247(2):216-222.

19. Ke G, *et al.* (2014) A cell-surface-anchored ratiometric fluorescent probe for extracellular pH sensing. *ACS Appl Mater Interfaces* 6(17):15329-15334.

20. Weerakkody D, *et al.* (2013) Family of pH (low) insertion peptides for tumor targeting. *Proc Natl Acad Sci U S A* 110(15):5834-5839.

21. Andreev OA, Engelman DM, & Reshetnyak YK (2014) Targeting diseased tissues by pHLIP insertion at low cell surface pH. *Front Physiol* 5:97.

22. Reshetnyak YK, Andreev OA, Lehnert U, & Engelman DM (2006) Translocation of molecules into cells by pH-dependent insertion of a transmembrane helix. *Proc Natl Acad Sci U S A* 103(17):6460-6465.

23. Reshetnyak YK, Segala M, Andreev OA, & Engelman DM (2007) A monomeric membrane peptide that lives in three worlds: in solution, attached to, and inserted across lipid bilayers. *Biophys J* 93(7):2363-2372.

24. Andreev OA, *et al.* (2007) Mechanism and uses of a membrane peptide that targets tumors and other acidic tissues in vivo. *Proc Natl Acad Sci U S A* 104(19):7893-7898.

25. Karabadzhak AG, *et al.* (2012) Modulation of the pHLIP transmembrane helix insertion pathway. *Biophys J* 102(8):1846-1855.

26. Vavere AL, *et al.* (2009) A novel technology for the imaging of acidic prostate tumors by positron emission tomography. *Cancer Res* 69(10):4510-4516.

27. Reshetnyak YK, *et al.* (2011) Measuring tumor aggressiveness and targeting metastatic lesions with fluorescent pHLIP. *Mol Imaging Biol* 13(6):1146-1156.

28. Daumar P, *et al.* (2012) Efficient (18)F-Labeling of Large 37-Amino-Acid pHLIP Peptide Analogues and Their Biological Evaluation. *Bioconjug Chem* 23(8):1557-1566.

29. Macholl S, *et al.* (2012) In vivo pH imaging with (99m)Tc-pHLIP. *Mol Imaging Biol* 14(6):725-734.

30. Sosunov EA, *et al.* (2013) pH (low) insertion peptide (pHLIP) targets ischemic myocardium. *Proc Natl Acad Sci U S A* 110(1):82-86.

31. Adochite RC, *et al.* (2014) Targeting Breast Tumors with pH (Low) Insertion Peptides. *Mol Pharm* 11(8):2896-2905.

32. Cruz-Monserrate Z, *et al.* (2014) Targeting pancreatic ductal adenocarcinoma acidic microenvironment. *Sci Rep* 4:4410.

33. Karabadzhak AG, *et al.* (2014) pHLIP-FIRE, a cell insertion-triggered fluorescent probe for imaging tumors demonstrates targeted cargo delivery in vivo. *ACS Chem Biol*.

34. Suzuki M, Mose ES, Montel V, & Tarin D (2006) Dormant cancer cells retrieved from metastasis-free organs regain tumorigenic and metastatic potency. *Am J Pathol* 169(2):673-681.

35. Rae JM, *et al.* (2004) Common origins of MDA-MB-435 cells from various sources with those shown to have melanoma properties. *Clin Exp Metastasis* 21(6):543-552.

36. Loike JD & Silverstein SC (1983) A fluorescence quenching technique using trypan blue to differentiate between attached and ingested glutaraldehyde-fixed red blood cells in phagocytosing murine macrophages. *J Immunol Methods* 57(1-3):373-379.

37. Elamrani K & Blume A (1983) Effect of the lipid phase transition on the kinetics of H+/OH- diffusion across phosphatidic acid bilayers. *Biochim Biophys Acta* 727(1):22-30.

38. Hunter RC & Beveridge TJ (2005) Application of a pH-sensitive fluoroprobe (C-SNARF-4) for pH microenvironment analysis in Pseudomonas aeruginosa biofilms. *Appl Environ Microbiol* 71(5):2501-2510.

39. Ibrahim-Hashim A, *et al.* (2011) Free Base Lysine Increases Survival and Reduces Metastasis in Prostate Cancer Model. *J Cancer Sci Ther* Suppl 1(4).

40. Kozin SV, Shkarin P, & Gerweck LE (2001) The cell transmembrane pH gradient in tumors enhances cytotoxicity of specific weak acid chemotherapeutics. *Cancer Res* 61(12):4740-4743.

41. Jahde E & Rajewsky MF (1982) Tumor-selective modification of cellular microenvironment in vivo: effect of glucose infusion on the pH in normal and malignant rat tissues. *Cancer Res* 42(4):1505-1512.

42. Warburg O, Wind F, & Negelein E (1927) The metabolism of tumors in the body. *J Gen Physiol* 8(6):519-530.

43. Gillies RJ, Robey I, & Gatenby RA (2008) Causes and consequences of increased glucose metabolism of cancers. *J Nucl Med* 49 Suppl 2:24S-42S.

44. Newell K, Franchi A, Pouyssegur J, & Tannock I (1993) Studies with glycolysis-deficient cells suggest that production of lactic acid is not the only cause of tumor acidity. *Proc Natl Acad Sci U S A* 90(3):1127-1131.

45. Grillon E, *et al.* (2011) The spatial organization of proton and lactate transport in a rat brain tumor. *PLoS One* 6(2):e17416.

46. Rehncrona S (1985) Brain acidosis. *Ann Emerg Med* 14(8):770-776.

47. Xiong ZG, Pignataro G, Li M, Chang SY, & Simon RP (2008) Acid-sensing ion channels (ASICs) as pharmacological targets for neurodegenerative diseases. *Curr Opin Pharmacol* 8(1):25-32.

48. Swietach P, Vaughan-Jones RD, & Harris AL (2007) Regulation of tumor pH and the role of carbonic anhydrase 9. *Cancer Metastasis Rev* 26(2):299-310.

49. Ihnatko R, *et al.* (2006) Extracellular acidosis elevates carbonic anhydrase IX in human glioblastoma cells via transcriptional modulation that does not depend on hypoxia. *Int J Oncol* 29(4):1025-1033.

50. Hashim AI, Zhang X, Wojtkowiak JW, Martinez GV, & Gillies RJ (2011) Imaging pH and metastasis. *NMR Biomed* 24(6):582-591.

51. Gillies RJ, Raghunand N, Karczmar GS, & Bhujwalla ZM (2002) MRI of the tumor microenvironment. *J Magn Reson Imaging* 16(4):430-450.

Figures

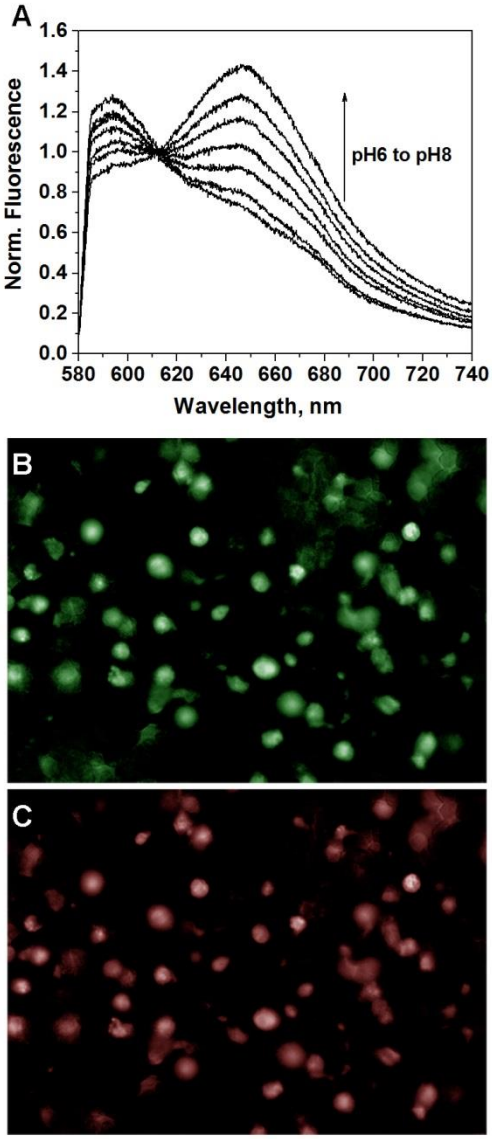

Figure 1. **SNARF-pHLIP spectra and images.** Emission spectra of the SNARF-pHLIP treated with liposomes at different pHs were recorded under inverted epi-fluorescent microscope connected to spectrograph (A). Fluorescent images of HeLa tumor spheroids treated with the SNARF-pHLIP at pH6.6 were acquired using 580 ± 10 nm (B) and 640 ± 10 nm (C) emission filters. Colors are artificial.

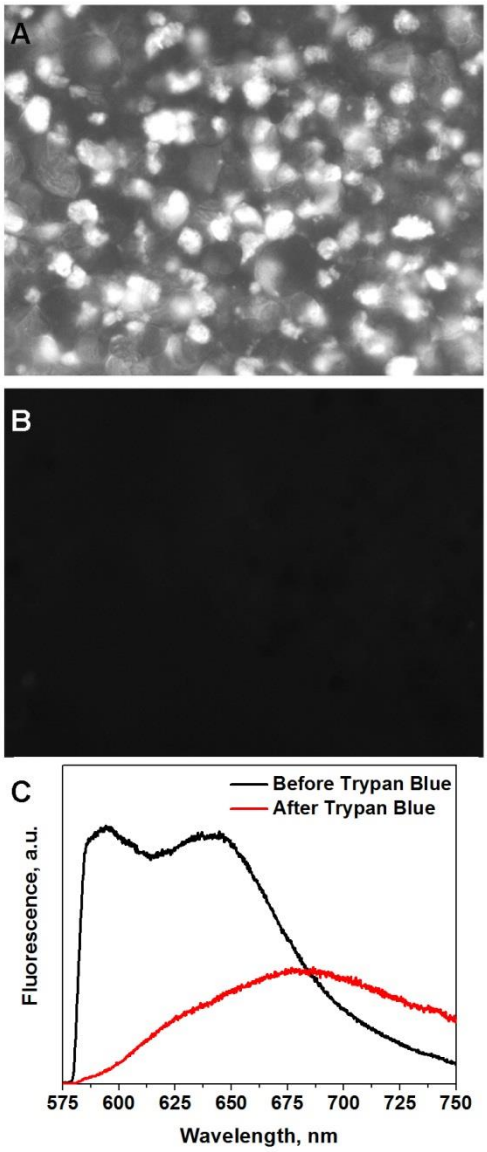

Figure 2. Trypan Blue assay. The SNARF-pHLIP image of HeLa tumor spheroids before (A) and immediately after (B) addition of 0.67 M of Trypan Blue acquired via 580 ± 10 nm emission filter. The spectra of the SNARF-pHLIP treated with HeLa tumor spheroids before and after treatment with Trypan Blue are shown in panel C.

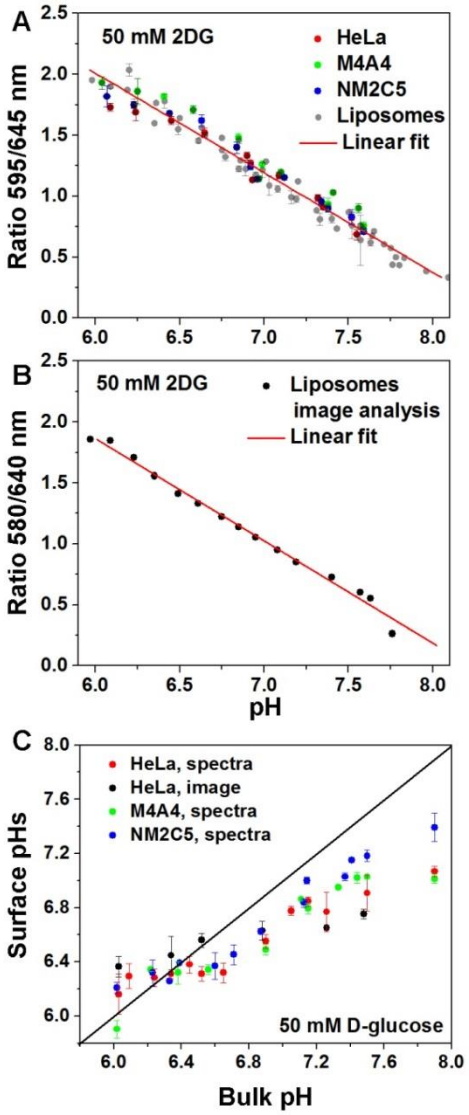

Figure 3. Calibration curves and pH at the surface of cancer cells in tumor spheroids. Calibration curve obtained by linear fitting of 595/645 fluorescence ratios of the SNARF-pHLIP treated with liposomes and HeLa, M4A4 and NM2C5 tumor spheroids in presence of 50 mM of 2DG at different pH of media (A). Calibration curve obtained by linear fitting of fluorescent images ratios at 580 and 640 nm of the SNARF-pHLIP treated with liposomes in presence of 50 mM of 2DG at different pH of media (B). The values of surface pHs obtained from HeLa, M4A4 and NM2C5 cells grown in tumor spheroids and treated with the SNARF-pHLIP in PBS of different pH containing 50 mM of glucose calculated from spectra and images (C).

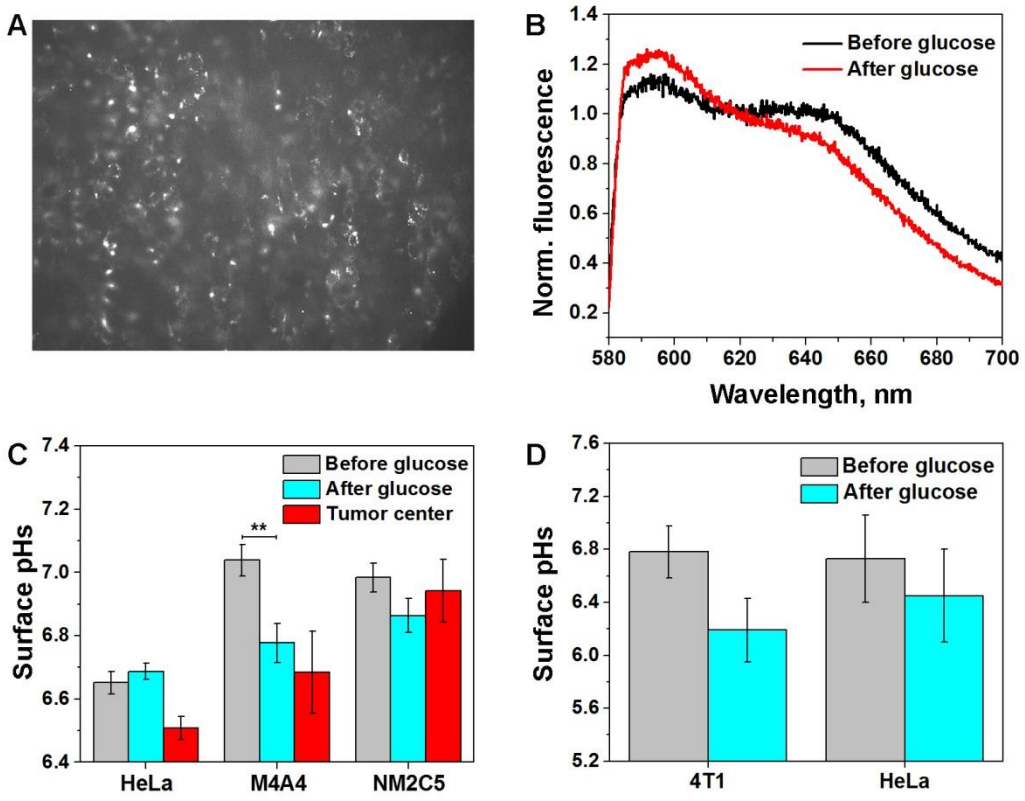

Figure 4. pH at the surface of cancer cells measured *in vivo* and *ex vivo* on tumors. The fluorescent image of HeLa tumor in live mice (skin is removed from tumor site). The SNARF-pHLIP was given as a single tail vein injection (A). Changes of the SNARF-pHLIP fluorescence spectra in HeLa tumor recorded on live animal before and after IP injection of 125 mg glucose (B). The mean values of the surface pHs in tumor of live animal before and after injection of glucose and in the middle of the excised tumor after glucose injection (*in vivo* measurements) (C). The mean values of the surface pHs in HeLa and 4T1 tumors excised from animal and treated with the SNARF-pHLIP before and after incubation with glucose (*ex vivo* measurements) (D).